Engineering Novel optical sensors for magnetic field sensing applications

A Thesis Submitted to the
College of Graduate and Postdoctoral Studies
in Partial Fulfillment of the Requirements
for the degree of Doctor of Philosophy
in the Division of Biomedical Engineering
University of Saskatchewan
Saskatoon

By
Hammed Adewale Ejalonibu

Permission to Use

In presenting this thesis in partial fulfilment of the requirements for a Postgraduate degree from the University of Saskatchewan, I agree that the Libraries of this University may make it freely available for inspection. I further agree that permission for copying of this thesis in any manner, in whole or in part, for scholarly purposes may be granted by the professor or professors who supervised my thesis work or, in their absence, by the Head of the Department or the Dean of the College in which my thesis work was done. It is understood that any copying or publication or use of this thesis or parts thereof for financial gain shall not be allowed without my written permission. It is also understood that due recognition shall be given to me and to the University of Saskatchewan in any scholarly use which may be made of any material in my thesis.

Disclaimer

Reference in this dissertation to any specific commercial products, process, or service by trade name, trademark, manufacturer, or otherwise, does not constitute or imply its endorsement, recommendation, or favoring by the University of Saskatchewan. The views and opinions of the author expressed herein do not state or reflect those of the University of Saskatchewan, and shall not be used for advertising or product endorsement purposes.

Requests for permission to copy or to make other use of material in this thesis in whole or part should be addressed to:

Head of the Division of Biomedical Engineering,
Room 2B60 57 Campus Drive,
University of Saskatchewan,
Saskatoon, Saskatchewan, S7N 5A9,
Canada.

OR

Dean College of Graduate and Postdoctoral Studies,
University of Saskatchewan,
116 Thorvaldson Building, 110 Science Place,
Saskatoon, Saskatchewan, S7N 5C9,
Canada.

Abstract

Research aimed at engineering magnetic detectors will continue to gain wide interest due to the numerous applications of field sensors. Over the years, several methods have been developed to sense and image magnetic fields with a majority of these methods further integrated with medical imaging modalities operated at low fields e.g., magnetic resonance imagers (MRIs). Classical methods of detection making use of inductive coils, based on Faraday's law of induction, or superconducting quantum interference devices (SQUIDs), based on the Josephson effect in superconducting materials are well researched. In addition, optical means of magnetic detection, for example, atomic vapour magnetometers (AVMs) based on alkali spins in massive vapour cells, have shown improved sensitivity over other methods. Nonetheless, the significant drawbacks these methods including the need for cryogenic temperature operations, and size, limits practical applications for sensing in compact medical devices. Magnetic field detectors based on nitrogen vacancies (NV) centres in diamond render an alternative to replace other detection protocols with a potential sensitivity well above the classical limit. The NV centres in diamond have numerous properties making it a sought after candidate for magnetic field sensing applications. Its long spin coherence time at room temperature and an efficient method of initializing with optical readout of electronic spins make it an ideal candidate for magnetometry. Above all, NV-based sensors can be operated over a wide range of temperatures with high spatial resolutions; therefore, it is the aim of this dissertation to provide an all-around exploratory study to address specific problems in the material science, microwave engineering, and magnetometry aspect of the NV centre discipline.

First, the potential of holding large ensembles of NV^- centres in polycrystalline diamonds (PCDs) grown over non-diamond substrates was explored. A high concentration of NV^- centres are a prerequisite to improving the sensitivity of NV sensing protocol, thus making PCDs a favourable candidate for wide-field magnetic field sensing. In addition, PCDs

with the desired concentration of NV^- centres can be obtained in large quantities and at a lower cost, hence this is a cost-effective option in applications where NV sensor arrays are needed. Results obtained from this part of the thesis showed the formation of both neutral and negatively charged NV centres at an optimum nitrogen flow rate of 10 sccm. This study is essential in benchmarking an optimal parameter space for the growth of nitrogen-doped polycrystalline diamonds suitable for sensing applications. Further, the magnetometry applications of diamonds rely on the incorporation of NV^- optical centres in proximity to the diamond surface; there is however a limited understanding of the effect of nitrogen flow rate on the surface charge of NV centres at the surface of PCDs. An exhaustive study on the contributions of nitrogen flow rate on the surface morphology, grain orientations, and the formation of bonded carbon found at the grain/grain boundaries was carried out to understand the correlation between ingrained surface properties of nitrogen-doped PCDs and the formation of NV centres in PCDs. Based on these experimental observations, a mechanism for the changes in the surface morphology of films grown under step-wise nitrogen doping was proposed. Consequently, this model was used to explain the possible dominance of NV^0 centres in PCDs in the low-pressure growth regime. The results obtained from this study contribute to a better understanding of the process for the formation of NV^-centres in PCDs deposited at low pressure.

For sensing applications, a novel NV sensor utilizing a different illumination scheme when compared with the confocal system of sensing was designed and constructed. The performance of the designed system was tested by comparing experimental fluorescence (FL) maps obtained with the confocal system set-up under varying optical powers. The designed system status and proposed performance for sensitivity to fluorescence emission were accessed in terms of signal-to-noise ratio (SNR) and signal-to-background ratio (SBR). Although the conventional confocal set-up outperforms our new design in terms of their SNR in different optical excitation regimes, the new design meets the performance requirement in the undersaturation optical excitation regime. Subsequently, the newly designed system was tested for its magnetic field detection potentials and sensitivity in a Halbach magnet configuration

using the optically detected magnetic resonance (ODMR) protocol. According to the absorbtion profiles observed in the measured ODMR spectrum, each NV centre experiences a static magnetic field in the range 2.14 - 6.07 mT of the Halbach magnet. The sensitivity was estimated and found to be approximately 0.2 $\mu\mathrm{T}/\sqrt{Hz}$. These results pave way for the development of scalable NV sensors using the novel excitation and collection methods developed in this thesis.

Statement of Co-authorship

The research in this thesis are a result of collaborations between the author, Hammed Ejalonibu, Prof. Gordon Sarty, and Prof. Michael Bradley of the Division of Biomedical Engineering and the Department of Physics and Engineering Physics at the University of Saskatchewan. While this thesis is not a full manuscript based thesis, the authors' contributions are described for all published and submitted articles below.

A substantial part of Chapter 2 was submitted for publication in *Materialia*. The manuscript under review was drafted by all authors. The work in chapter 3, was published in *Materials Science: Materials in Electronics*. Conceptualization, experimentation, characterization, data analysis, and drafting was carried out by Hammed Ejalonibu. Gordon Sarty and Michael Bradley coordinated the manuscript preparation and provided overall supervision of the research.

The content in chapter 4 was published in *Material Science and Engineering: B*. For this manuscript, the conceptualization, experimentation, characterization, data analysis, and drafting was carried out by Hammed Ejalonibu. Gordon Sarty and Michael Bradley coordinated the manuscript preparation and provided overall supervision of the research.

A substantial part of Chapter 5 and 6 was submitted to the journal of *Measurement Science and Technology*. For this manuscript, Gordon Sarty conceptualized the experiment. Actual experimentation, characterization, data analysis, and drafting was carried out by Hammed Ejalonibu. Gordon Sarty and Michael Bradley coordinated the manuscript preparation and provided overall supervision of the research.

Chapter 7 is a general conclusion of the thesis and is solely written by Hammed Ejalonibu.

Acknowledgements

It turned out that doing a Ph.D. is a pretty daunting task. I was however fortunate to have amazing advisors, friends, and colleagues that helped me through this phase. First, I would like to thank my thesis advisors, Dr. Gordon Sarty and Dr. Michael Bardley for their consistent support and encouragement. Dr. Sarty was always available to talk and give suggestions during tough times. Most of the skills I gathered from both advisors were invaluable and have definitely prepared me for a post-PhD life elsewhere.

My sincere appreciation goes to the members of my advisory committee; Dr. Artur Sowa, Dr. Gap Soo Chang, and Dr. Paul Babyn for their valuable inputs and advice on this research. Everyone came from their different area of expertise to make this work a total complete. Many thanks to Dr. Logi Vidarson of LT Imaging Inc., and Dr. George Belev of the Saskatchewan Structural Science Centre (SSSC), for their technical support during the last phase of my experimentation. Logi was my "go-to person" when it comes to RF electronics and SDRs, while George gave useful advice on the optical part of the project. Constant support from my labmates, Pallavi Bohidar, Farnaz Zohourparvaz, and Faezeh Ebadollahi are well appreciated - you guys were amazing.

Special thanks to my parents Mr. and Mrs. (Late) Ejalonibu for their prayers. My mother left this world for a heavenly abode at a time I was rounding up this thesis. Indeed your constant prayers and support pushed me this far - we will meet again, of that I am sure, rest in peace Ayinke Kudirat! Life wouldn't have been easy without the love, care, and support from friends like Farida Oyewale, Stephen Owuamanam, Dr. Jude Okolie, Peter Bankole, Adeniyi Adebayo, Ukoji Nnanna, Jude Dugbere, and Olamide Oriola - you guys made Saskatoon enjoyable.

Lastly, I am grateful for the funding provided by the Division of Biomedical Engineering of the University of Saskatchewan, NSERC Discovery and CSA Fast grant awarded to Dr. Sarty and Dr. Bradley in support of this work.

Dedication

In loving memory of my late mother, Mrs Kudirat Ayinke Ejalonibu.

Contents

List of Tables

List of Figures

List of Abbreviations

MRI	Magnetic Resonance Imaging
SNR	Signal-to-Noise Ratio
SBR	Signal-to-Background Ratio
SQUID	Superconducting Quantum Interference Device
AVM	Atomic Vapour Magnetometer
DC	Direct Current
AC	Alternating Current
RF	Radiofrequency
NV	Nitrogen-Vacancy
SCD	Single crystalline diamond
PCD	Polycrystalline diamond
NCD	Nanocrystalline diamond
PL/FL	Photoluminescence/Fluorescence
CVD	Chemical Vapour Deposition
ODMR	Optically Detected Magnetic Resonance
EPR	Electron Paramagnetic Resonance
LCAO	Linear Combination of Atomic Orbitals
HPHT	High-Pressure-High-Temperature
HFCVD	Hot Filament Chemical Vapour Deposition
MPECVD	Microwave Plasma Enhanced Chemical Vapour Deposition
LPHT	Low Pressure Low Temperature
CCD	Charged Coupled Device
FWHM	Full Width Half Maximum
SEM	Scanning Electron Microscope
XPS	X-ray Photoelectron Spectroscopy
AFM	Atomic Force Microscopy
GIXRD	Grazing Incident X-ray Diffraction
FOV	Field of View
LLD	Limit of Detection
BE	Beam Expander
DPSS	Diode Pumped Solid State
SDR	Software Defined Radio
FPGA	Field Programmable Gate Array
ROI	Region of Interest
LED	Light Emitting Diode

Chapter 1

Introduction

"Your cellphone has 10 sensors, and your car has 400, but your body has none - that's going to change."

– Vinod Khosla

Magnetic field detectors are used for a wide range of applications. Examples are in current and position sensing, medical and motor diagnostics systems, as well as in geophysics and astronomy [1, 2, 3]. In addition, magnetic field sensors are also enabling instruments for the fundamental studies of magnetism and symmetries [4, 5], spin dynamics [6], and mechanical motions [7, 8]. In contrast to other forms of detectors used for temperature, pressure, and strain sensing, magnetic detectors do not directly measure the physical properties of interest [9], they instead detect changes in the magnetic fields while deriving information such as direction, presence, or electrical currents from them. The resulting output of these sensors requires adequate signal processing for translation into the desired parameter. In recent times, the detection of low-magnetic fields with high magnetic field sensitivity (defined as noise equivalent magnetic flux density) has been central to several areas of modern science and technology. For instance, the effective detection of low-magnetic fields is now crucial in geophysics, solid-state physics, and medical imaging. For the latter, accessible diagnostic devices requiring low-frequency magnetic field sensors with high sensitivity and spatial resolution (for example, low-field magnetic resonance imagers (MRIs)) are now being developed, therefore improving detection sensitivity in low-field magnetic imagers of such is of importance since clinical imaging modalities requires a high signal-to-noise ratio (SNR)

[10]. Different types of magnetic field sensors have been introduced in the past to detect weak magnetic fields with high sensitivity, examples include Hall effect sensors, superconducting quantum interference devices (SQUIDs), giant magneto-impedance sensors, and the atomic vapour magnetometers (AVMs) to mention a few. In this chapter, some magnetic field sensors pertinent for comparison to this study will be described while explaining their advantages and disadvantages for use at low fields. The chapter also introduces the aim and objectives of this dissertation.

1.1 Existing Magnetic Field Sensors

1.1.1 Induction coils

The induction coils, commonly referred to as the pickup coil sensors are one of the oldest and most popular types of magnetic sensors [11, 12]. They can be deployed for several applications, for example, they have been used for years in the study of magnetic field variations in space plasma [13], and also in the measurement of micropulsations of the earth's magnetic field [14]. The main advantage of using the inductive sensor is that they are passive sensors and do not require any internal energy to convert magnetic fields into electrical signals; the only power consumption linked to using an induction coil is that needed for signal processing [15]. The working principle of this sensor is based on Faraday's law of induction. If an induction coil of N turns shown in Figure 1.1 is in a magnetic field $\mathbf{B}$, the magnetic flux ϕ_B for the surface is given by the surface integral:

$$\phi_B = \oiint_{\Sigma} \mathbf{B}(t) \cdot d\mathbf{A}, \tag{1.1}$$

where d$\mathbf{A}$ is the area element, $\mathbf{B}$ is the magnetic field, and $\mathbf{B} \cdot$ d$\mathbf{A}$ is the scalar dot product of the flux element through d$\mathbf{A}$. The magnetic flux through the loop is proportional to the number of magnetic flux lines passing through the surface and according to Faraday's law, the inductive voltage signal through the N turns of the coil is proportional to the time derivative

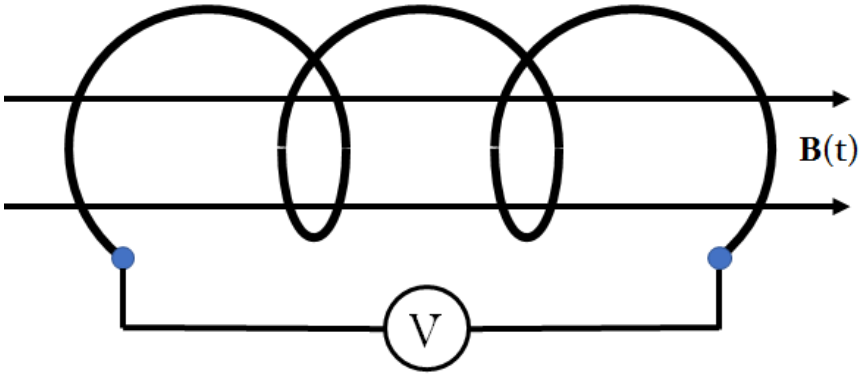

Figure 1.1: A simple coil-based magnetometer of N coil turns, where $\mathbf{B}(t)$ is the applied external magnetic field through the sensor coil and V is the voltage generated by the induction coil.

of the magnetic flux through it:

$$V(t) = -N\frac{d\phi_B}{dt} = -N \iint_{\Sigma} \frac{d\mathbf{B}(t)}{dt} \cdot d\mathbf{A}, \tag{1.2}$$

The quantity $V(t)$ in Equation 1.2 is proportional to the rate of change of the magnetic field, $\mathbf{B}(t)$. Furthermore, it is evident from Equation 1.2 that a large voltage signal; translating into improved coil sensitivity can be achieved by using a large number of N coil turns and large active area A. Nevertheless, the optimization process for the inductive coil sensitivity performance remains arduous. While the inductive sensors have been reported to show a sensitivity of up to 100 $fT/\sqrt{Hz}$ [16, 17], they however have a few shortcomings. First, the output signal is frequency-dependent, thus the signal of the inductive pick-up coil increases with an increase in the magnetic field and corresponding frequency, therefore, the inductive pick-up coils are less sensitive and noisy when used to detect weak magnetic fields. Furthermore, it is difficult to miniaturize the coils since the sensitivity depends on the coil area.

1.1.2 Superconducting Quantum Interference Device (SQUID)

SQUIDs are one of the most sensitive devices for the detection of magnetic flux, ϕ_B [18] and have gained popularity for the detection of low magnetic fields in recent times [19]. The magnetic flux detected in SQUIDs is converted into a voltage across the device to

be measured. SQUIDs are made up of superconducting loops containing either one or two Josephson junctions as shown in Figure 1.2. In terms of sensitivity, SQUIDs are very sensitive magnetometers measuring magnetic fields up to 5×10^{-18} T with noise level as low as 3 fT/$\sqrt{Hz}$ [20]. Detection limits in the fT range are achieved in millimetre-sized sensors, with a reduction in sensitivity value as the device is further miniaturized into micro or nano-size [21, 22, 23].

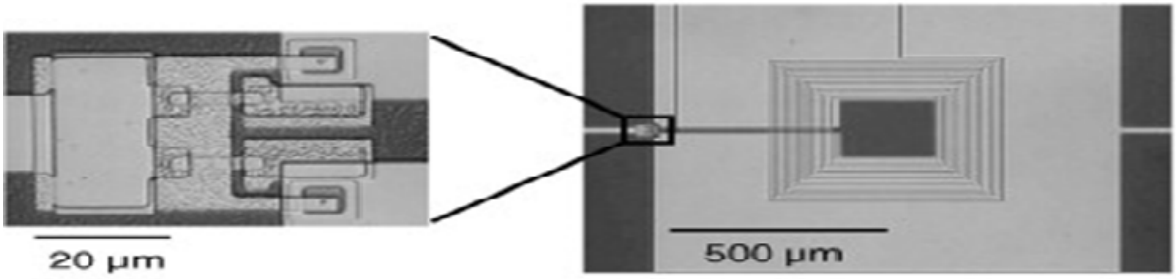

Figure 1.2: An electron micrograph of a SQUID with multi-turn input coil deposited on an insulating layer as adapted from Ref.[10]. The expanded view next to it shows the two Josephson junctions and shunts.

There are two types of SQUIDs namely, the direct current (DC) and radio frequency (RF) SQUIDs. DC SQUIDs have two Josephson junctions in parallel with the superconducting loop. The critical current of each junction is I_c, and the inductance of the loop is L. If it is assumed that both junctions in DC SQUIDs are identical, and the SQUID biased by a current I_b, the spectral density of the voltage noise power (the signal power present as a function of frequency, per unit frequency) across the SQUID in the absence of excess noise may be written as [24]:

$$S_v = \left(\frac{\partial V}{\partial \phi}\right)^2 4\frac{K_B T L^2}{2R} + 4K_B T R_d, \tag{1.3}$$

where $R_d = \partial V/\partial I$ is the dynamic resistance of the SQUID, R is the shunt resistance per junction, ϕ is the applied flux, $\partial V/\partial \phi$ is the flux to the voltage-transfer function, K_B is the Boltzmann constant, and T is the operating temperature of the SQUID. A current running through the ring will then generate a voltage V drop across the junction given as:

$$V = \frac{IR}{2}\left[1 - \left(\frac{2I_c}{I}\cos\frac{\pi\phi}{\phi_0}\right)\right], \tag{1.4}$$

The voltage drop changes in the presence of induced currents. A change in the magnetic field resulting from the spin transition of sample NMR spins can then be detected electrically [25]. Contrarily, RF SQUIDs operate based on the alternating current (AC) Josephson effect and use only one Josephson junction. Although less sensitive compared to DC SQUIDs, RF SQUIDs are cheaper and easier to manufacture. RF SQUIDs are normally inductively coupled to a resonant tank circuit [26]. The effective inductance of the tank circuit changes depending on the external magnetic field, thus changing the resonant frequency of the tank circuit. The frequency measurements can be taken, and the losses which appear as the voltage across the load resistor in the circuit area are a periodic function of the applied magnetic flux [27]. SQUIDs, in general, are required for numerous applications. Importantly, reports on their use as magnetic detectors at low and ultra-low fields can be found in Refs. [28, 29, 30, 31]. Even though SQUIDs offer exceptional sensitivity, the presence of magnetically shielded room and cooling of elements with liquid nitrogen or helium is needed for their operation [32, 33]. Also, issues related to poor resolution which can be solved by the implementation of specific hardware and shielding technologies exist.

1.1.3 Atomic Vapour Magnetometers (AVMs)

Atomic vapour magnetometers are regarded as one of the most sensitive optical detectors for magnetic field sensing [4, 34]. They are spin-based devices making use of an optical interrogation to probe atomic spins in a vapour cell while detecting variations in magnetic fields. The measurement of magnetic fields in atomic vapour cells is based on the Faraday effect in a vapour of alkali atoms like potassium (K), rubidium (Rb), or cesium (Cs) [25]. The alkali atom is confined in an optically transparent cell in proximity to the specimen to be measured as shown in Figure 1.3. The working principle of the atomic vapour magnetometer can be understood as evolving in different steps (see Figure 1.3 (a), (b), and (c)). First, the individual alkali atoms are optically pumped and made to create a macroscopic magnetic moment using a polarized beam. During this process, nearly all of the randomly oriented electron spins are re-aligned along the pump beam optical axis.

In the presence of an external magnetic field, the aligned electron spins interact with the

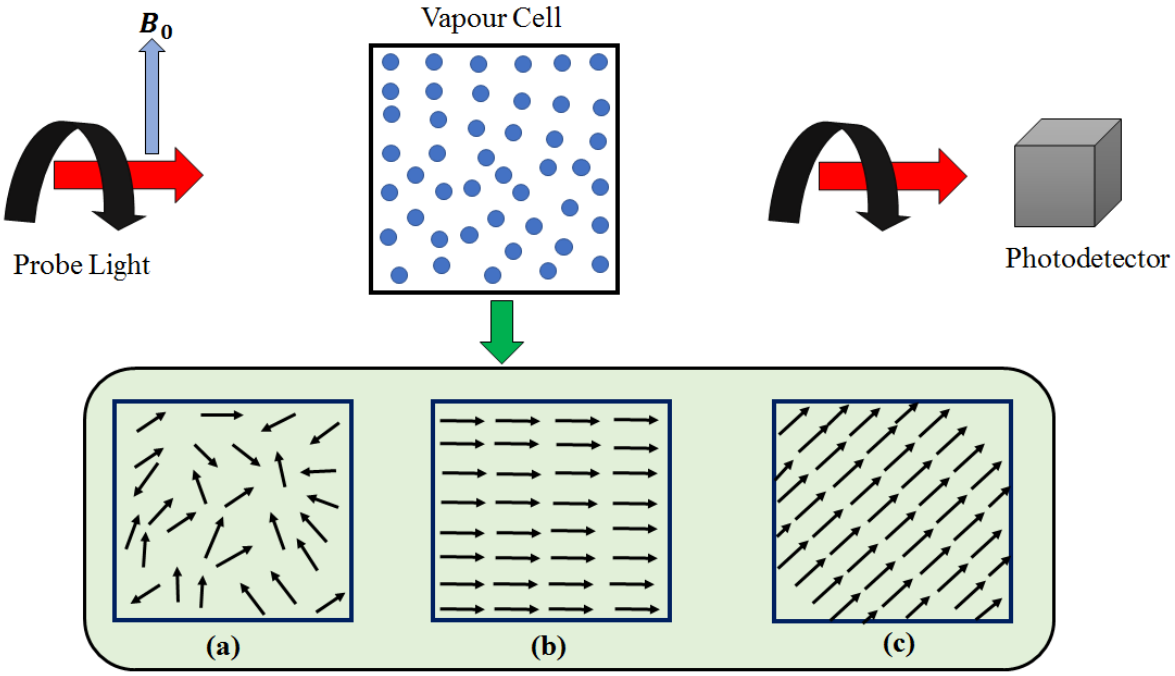

Figure 1.3: A schematic showing the working principle of the atomic vapour magnetometer. Light is used to interrogate alkali atoms such as rubidium (Rb), cesium (Cs), and potassium (K). (a) Spins are randomly oriented in the absence of interrogating light. (b) Spins align in the direction of the interrogating light. (c) Spins undergo precession about an applied magnetic field at a rate proportional to the magnitude of the field and finally, the measured precession angle is detected by a photodetector.

field causing a precession at the Larmour frequency $\omega = \gamma \mathbf{B}$, proportional to the value of the magnetic field $\mathbf{B}$ [35] given by:

$$\left.\frac{d < \mathbf{F} >}{dt}\right|_{\text{Larmour}} = \Omega \times < \mathbf{S} >, \tag{1.5}$$

where $\mathbf{F}$, is the field causing a precession, Ω is the angular frequency, and $< \mathbf{S} >$ is the electron spin polarization of the alkali vapour vapour atoms. If a linearly polarized beam is used for optical pumping, the NMR signal can be detected via a tilt of the beam polarization. This tilt based on Faraday rotation is directly proportional to the strength of the external magnetic field. In the past, sensitive atomic vapour magnetometers have been developed for magnetic field detection as detailed in Refs. [4, 36, 37]. The sensitivity of the vapour cell is

given by [5]:

$$\delta B \simeq \frac{1}{\gamma\sqrt{NVT_2t}}, \tag{1.6}$$

γ here is the gyromagnetic ratio of the alkali spins, N is the number of atoms, t is the measurement time, V is the measurement volume, and T_2 is the spin dephasing time of the spins. Alkali atoms loose spin coherence after collison with the vapour glass cells [38], thus limiting their polarization lifetime. Antirelaxation surface coating or buffer gases are sometimes used to reduce the effect of wall relaxation. Additionally, to obtain high sensitivities and long spin coherence times of the alkali spins, vapour cells in the order of cm^3 are needed, thus making them bulky and not applicable for compact applications. It is also important to mention that several other magnetic sensors such as the fluxgate sensor, magneto-electric sensor, and the cavity optomechanical magnetometers have extended applications in bio-medicine with detection limits ranging from 1 - 100 $pT/\sqrt{Hz}$ exist [39, 40, 41, 42], nonetheless, because of the focus of this thesis, the working principle of the sensors above were reviewed to serve as a background for the optical sensor to be discussed.

1.2 Statement of the Problem

Looking into the combinations of magnetic field detection techniques reviewed above, it is evident that existing magnetometer types cannot satisfy the stringent requirements of a combination of high magnetic field sensitivity, compactness, and ambient temperature operations needed for low magnetic field sensing. Lately, the search for novel optical sensors satisfying these requirements has brought forward a new class of quantum material for magnetic field detection. These classes of materials are based on spin qubits found in host diamonds possessing remarkable magnetic and quantum properties. A typical spin defect in diamonds that has been explored for magnetic field sensing till-date is the nitrogen-vacancy (NV) centre. Table 1.1 compares existing magnetic field sensors and the novel NV sensor found in diamonds. The comparison table indicates that NV centres satisfies the sensitivity, size, noise, and temperature requirements needed for the detection of low magnetic fields if properly optimized.

Table 1.1: Comparison of existing sensors for magnetic field detection purpose.

Properties	Induction Sensor	Vapour Sensor	Hall Sensor	Force Sensor	SQUIDs	NV Sensor
Sensitivity	Varies	pT	μT	nT	fT	pT - μT
Size	Small-Large	Medium	Ultra small	Small	Medium	Nanoscale
Sensor Noise	Low	Ultra-low	High	Low	Ultra-low	Ultra low
Temperature	Ambient	Ambient	Ambient	Ambient	Ultra-low	Ambient
Cost	Low	High	Low	Medium	High	High

The NV centres in diamond have numerous properties making it a sought after candidate for magnetometry applications. Of its properties, its long spin coherence time at room temperature, and an efficient method of initializing/optical readout of electronic-spins make it an ideal candidate for magnetic field sensing. Additionally, NV based sensors can be operated over a wide range of temperature with high spatial resolutions. In 1997, Gruber et al. [43] were one of those that first demonstrated the magnetic resonance of single NV centres at room temperature. Since then, several experiments demonstrating the use of single and ensembles of NV centres in quantum information processing [44, 6], bio-magnetometry [45], electrometry [46], and as sensitive nanoscale thermometer [47] have been published. Further, an ensemble of NV centres located in diamond have been exploited for two-dimensional magnetic field imaging [48, 49, 50], while their counterparts located in proximity to the surface of the host diamond can be used for nuclear spin sensing with high sensitivities [51, 52]. In Table 1.2, the author has presented a range of magnetic field sensitivity and spatial resolutions (a measure of the smallest object a sensor can resolve) of a list of magnetometers (based on the literature reviewed) and presents this comparison scheme to validate the need for a more sensitive nanoscale magnetic field sensor like the NV sensor with high photostability in the temperature ranges 0 - 600 K.

The research to develop magnetic sensors involving NV centres is highly interdisciplinary putting into play material science, microwave engineering, and magnetometry. From the material science standpoint, optimal conditions for fabricating NV sensors with a good coherence time are still not well understood. The question of how best to optimize conditions for the fabrication of NV sensors over a large area for wide-field imaging needs to be addressed. Besides the optimization of fabrication methodologies, what factor(s) affect the formation of NV sensors fabricated in polycrystalline diamonds (PCDs) at low-pressure conditions? On the magnetometry side, we are concerned with the design and applications of a scalable NV sensor. Is it possible to use the sensor to characterize static magnetic fields in different magnet configurations? These are some of the research questions addressed in this dissertation, since to the best of the author's knowledge, not much has been done to answer these

Table 1.2: Comparison of different magnetometer(s) sensitivity and spatial resolution, from the conventional inductive pickup coils through SQUIDs, atomic vapour, hall sensors, and finally the reported sensitivities of NV sensor in diamond.

Magnetometer(s)	Sensitivity ($/\sqrt{Hz}$)	Spatial resolution (mm)
Inductive Pick-up coil	Scales as coil winding volume (V_W), frequency, and diameter of the coil [53].	1.3 - 4.2 [54], 0.75 - 1 [55], 0.125 - 0.5 [56].
SQUIDs	1.2 - 2.8 fT [29], 3.5 fT [57], 1.4 pT [58]	5.0×10^{-3} [59], 0.1 [58], 10^{-4} [57].
Atomic Vapor Magnetometers	200 fT [60], 25 fT [61], 70 fT [62], 10 fT [62]	1 [36], 3 [53].
Hall Sensors	12 μT [63] , 5μT [64]	4 [65], 0.7 $\times$ 10$^-$3 [66].
Force Sensors	Relatively low and not quantitatively defined [67, 68]	—
NV Sensors	3 nT [69], 1.7 nT [70], 8.3 pT [59]	10^{-6} [71], 6×10^{-6} [72], 4×10^{-5} [73].

questions. Although still at the exploratory phase, the data generated from the first few chapters of this thesis can be used to further optimize studies aimed at imploring PCDs for magnetic field sensing. Further, the latter aspect of this thesis showing the design of a novel NV sensor and a proof-of-concept for the detection of magnetic fields in an Halbach magnet configuration can be scaled up in the future to develop sensitive scalable sensors integrated with imaging devices operated at low fields.

1.3 Research Objectives

The overall aim of this dissertation is to address specific problems in the material science, microwave engineering, and magnetometry aspect of the NV centre discipline, and also to establish the feasibility of this approach in the characterization of low-magnetic fields of experimental MRIs. To realize this goal, the following objectives were pursued:

1. Determine the influence of nitrogen flow rate on the formation of NV sensors in PCDs. In this part of the studies, we investigate the effect of nitrogen flow rate on the morphology, optical, and photoluminescence (PL) properties of PCDs deposited at low-pressure conditions. This study is crucial to benchmark an optimal parameter space(s) for the growth of nitrogen doped polycrystalline diamonds suitable for sensing applications.

2. Determine optimal parameter conditions for the formation of NV sensors in PCDs. The study examines the influence of the step-wise surface nitrogen doping process on PCDs and used this to explain the dominance of neutral charged NV (NV^0) centres in PCDs deposited at low pressure using the chemical vapour deposition (CVD) technique. This aspect of our studies helps to give a better understanding of the formation of negatively charged NV centres (NV^-) in PCDs deposited at low pressure.

3. Design, construct and test the performance of a scalable NV based detector for magnetic sensing applications. In this part of the dissertation, an NV centre optical detector was conceptualized and designed for the purpose of magnetic field detection. The instrumentation and automation of the set-up were detailed in this part of the thesis.The

system status and proposed performance for sensitivity was accessed in terms of signal-to-noise ratio (SNR) and signal-to-background ratio (SBR). The study establishes a metric to compare the newly designed detection system to the conventional confocal system of detection.

4. Detect and characterize inhomogeneous radially-varying static magnetic fields - this study is a proof-of-principle. Here, the magnetic field detection potential and sensitivity of the NV sensor built was tested using a homebuilt Halbach magnet configuration. The sensitivity of the set-up was estimated and found to be approximately 0.2 $\mu\mathrm{T}/\sqrt{Hz}$.

1.4 Thesis Organization

This thesis contains seven chapters. The first few chapters are material-focused with the intent to contribute to the ever-expanding area of the NV centre material fabrication. Chapter 1 contains a brief overview of known magnetic field detectors, statement of the problem, and research objectives.

Chapter 2 provides a brief introduction to diamond and colour centres. The physics, electronic structure, and the basis for magnetic field detection of the NV centre were presented here. To provide a background for NV centre fabrication that will appear in later chapters, existing methods for NV centre fabrication were also reviewed. A substantial part of this review is in preparation for publication in *Materialia*.

In chapter 3, the parameter(s) space for the fabrication of negatively charged NV centres in PCDs was explored. The approach not only offers a standard recipe to grow inexpensive diamonds with NV centres over large areas, but also opened interesting findings on the effect of nitrogen flow rates on the morphology, physical properties, and optical properties of PCDs deposited at low-pressure conditions. This work was published in *Materials Science: Materials in Electronics*.

In chapter 4, a series of characterization techniques were used to identify an optimal parameter for the growth of NV optical centres in PCD diamonds. By using a step-wise doping technique, it was possible to explain the formation of NV centres at low pressure. The content of this chapter was published in *Material Science and Engineering: B*. At the end of this chapter, we identified issues relating to NV centre orientations and the poor sensitivities in PCDs and made recommendations for future research.

For magnetometry applications, it is important to design an optical setup for detection. Chapter 5 detailed the instrumentation and design of a simple but scalable bench detection optical apparatus using a different excitation protocol. Here, a comprehensive and detailed description of the construction and operation of a simple and scalable NV centre detector was detailed. The performance of the designed system was tested by comparing experimental fluorescence (FL) maps obtained with that of the confocal system set-up under varying optical power. The designed system status and proposed performance for sensitivity to fluorescence emission was accessed in terms of signal-to-noise ratio (SNR) and signal-to-background ratio (SBR). In wrapping up this chapter, the extendibility, scalability, and limitations of the designed system were discussed. A manuscript containing part of this work is in preparation for submission in *Measurement Science and Technology*.

In chapter 6, the magnetic field detection potential and sensitivity of the Sparrow NV sensor was tested using a homebuilt Halbach magnet configuration. The results obtained pave way for the development of scalable NV sensors using the excitation and collection methods developed in this thesis. Finally, highlights of research findings and some conclusions drawn from this research work were presented in chapter 7. Chapter 7 also includes some recommendations for future work.

Chapter 2

Background

"I never worry about diets. The only carrots that interest me are the number you get in a diamond."

– Mae West

2.1 Introduction

Diamond is regarded as a material of technological interest owing to its extreme mechanical hardness [74, 75, 76], high thermal conductivity, broad optical transparency, resistance to chemical corrosion [77, 78, 79], and its remarkable semiconducting properties (diamond has a band gap of about 5.47 eV for use in high temperature devices) [80, 81, 82, 83]; see Table 2.1 for a list of some of these properties. In a typical diamond lattice, carbon atoms are tetrahedrally coordinated, forming strong bonds to its four neighbours using hybrid sp^3 atomic orbitals, with angles of $109^o28^{'}$ to each other [84]. Diamond has a face centre cubic structure, with strongly covalent bonds between carbon atoms characterized by a small bond length of about 0.154 nm and bond energy of 711 KJ mol^{-1} [84, 65]. In nature, diamonds formed from carbon are found under high temperature and high pressure conditions, and also synthesized in the laboratory under similar high pressure conditions. In both natural and synthetic diamonds, nitrogen exists as a common atomic impurity [85, 86]. It suffices to say that the intrinsic properties of diamonds, for example, its colour and optical properties are greatly influenced by the form and concentration of nitrogen impurities present in the actual diamond lattice [87, 88]. Essentially, diamonds can be classified into types Ia, Ib,

IIa, and IIb depending on the level of nitrogen concentration, the form of nitrogen, and boron impurities present [86]. In type Ia diamonds, nitrogen is found in aggregated forms in contrast to their substitutional and atomically dispersed form in type Ib crystals. Most of the diamonds synthesized in the laboratory using different techniques, for example, chemical vapour deposition (CVD) are of type Ib [85]. The type IIa diamonds are the purest form of diamonds; containing a very small concentration of impurities, while type IIb contains boron impurities [85, 86]. Mainly, nitrogen impurities incorporated into diamonds can exist in several bonding configurations [89]. For example, the incorporation of nitrogen in diamonds might lead to the formation of A-centres (N_S - N_S) made up of two nearest neighbouring nitrogen atoms, B-centres ($4N_S$ - V^0) consisting of four nitrogen atoms surrounding a vacancy, and vacancies with complexes (N-V-N) [90, 91].

Table 2.1: A list of some selected properties of natural and synthetic diamonds [75, 92, 74, 80, 84]

Properties	
Density (g cm^{-3})	2.8 - 3.52
Thermal Capacity at 27^oC (J $mol^{-1}K^{-1}$)	6.12
Thermal Conductivity at 25^oC (W $m^{-1}K^{-1}$)	2100 - 2200
Band Gap (eV)	5.45
Electrical resistivity (Ω cm)	10^{12} - 10^{16}
Young's Modulus (GPa)	820 - 1250
Index of Refraction at 10 μm	2.34 - 2.42

Also, a C-centre corresponding to single substitutional nitrogen (N_S) atoms in the diamond lattice may be formed. In some cases, N_S atom adjacent a vacant centre in the diamond lattice is present, resulting in the formation of NV optical centres. Optical centres of this nature are commonly referred to as colour centers and are responsible for the numerous colours of diamonds. Some other examples of optical centres in diamond that are not considered in this dissertation are silicon-vacancy (SiV) centres, tin-vacancy (SnV), germanium-vacancy (GeV) centres etcetera. The main focus of this chapter is to present the properties of the NV centres. In addition, the principle behind the methods used to fabricate NV centres are

detailed to serve as a background for the fabrication technique adopted in later chapters for NV optical centre engineering.

2.2 The NV Centre

2.2.1 Physical Properties

The prominent nitrogen vacancy (NV) centre is a point defect in the diamond lattice with C_{3v} symmetry. It is one of the many colour defects in diamonds consisting of a substitutional nitrogen atom adjacent a vacancy in the diamond lattice (see Figure 2.1). The vector connecting the nitrogen atom and the vacancy defines the NV centres' symmetry axis. Results obtained from *ab initio* simulations indicate that the carbon atoms and the substitutional nitrogen atom relax outward from the vacancy [93]. There are four different orientations the NV centre can take, giving rise to four possible NV alignments along of one possible crystallographic axes: [111], [$1\overline{1}\overline{1}$], [$\overline{1}\overline{1}1$], and [$\overline{1}1\overline{1}$] as shown in Figure 2.2. The four possible alignments will be of interest when discussing the magnetic field sensing application of the NV centre.

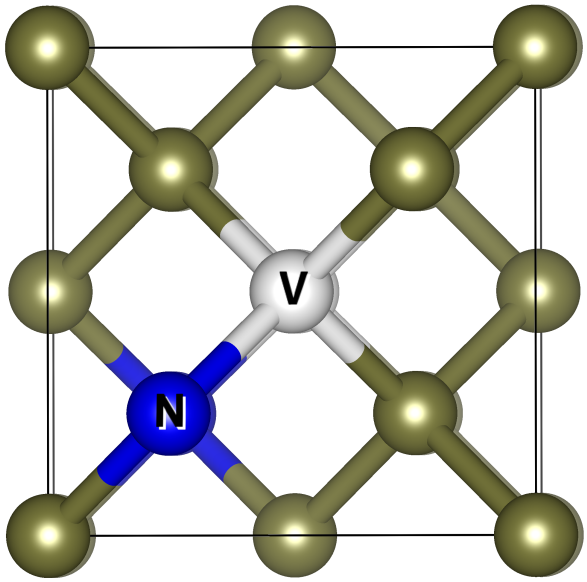

Figure 2.1: A schematics of the nitrogen-vacancy centre in the diamond lattice showing the vacancy (in white), the neighbouring carbon atom to the vacancy (in brown), and the substitutional nitrogen atom in blue.

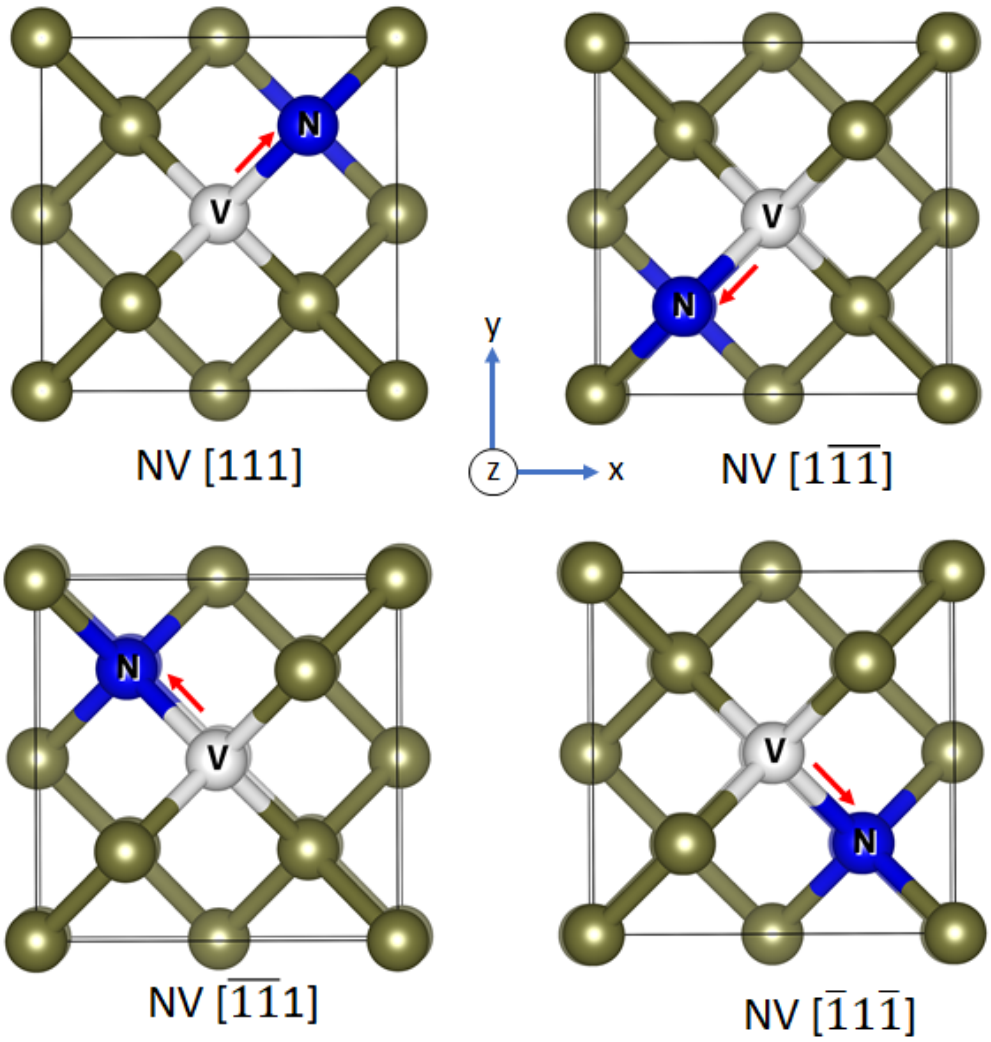

Figure 2.2: The four different orientations of NV centres in diamond; [111], [1$\bar{1}\bar{1}$], [$\bar{1}$1$\bar{1}$], and [$\bar{1}\bar{1}$1]. Nitrogen (N) atom are in blue, vacancies (V) are in white, and the carbon atoms of diamonds coloured lustrous grey. The NV axis are indicated in red arrows.

2.2.2 Charge State

NV centres can be found in two main charged states namely, the negatively charged (NV^-) and the neutral charged (NV^0) states, with each charged states having different optical and spin properties. For most applications, only the NV^- centres have been found useful, this is because there has been no report up to now on the coherent manipulation and readout of the NV^0 centres. The charge state of the defect is dictated by surrounding impurities and the position of the Fermi level [94]. The NV^- has six electrons associated with it, five of the electrons are contributed from neighbouring carbon atom (originating from three dangling carbon bonds) and the nitrogen atom (two valence electron from the nitrogen atom), while the extra electron which gives rise to the negative charge state is captured from an electron donor, for example oxygen. Upon optical excitation, the NV centre undergoes a stochastic charge state transition between the NV^- and the NV^0 state. The symmetry of the NV^- centre reduces the six electron system to a two electron, spin-1 system. At all time in this thesis, a distinction will always be made between the two charged states.

2.2.3 Electronic Structure and Optical Properties

Negatively charged NV centres emit red fluorescence signals in the energy range 1.65 - 2.0 eV (637 - 750 nm) when optically pumped using green light of about 2.33 eV (532 nm) photon energy. The emitted fluorescence can be used to detect spin transitions induced by microwave radiation, thus leading to optically detected magnetic resonance (ODMR) [1] - similar to the commonly known electron paramagnetic resonance (EPR) [43]. Figure 2.3 shows the electronic structure of the NV^- centres that has been constructed using a linear combination of atomic orbitals (LCAO) group theoretical approach [96, 97]. From the electronic structure diagrams, it is known that the NV^- centre consists of a spin-triplet ground ($^3A_2$) and excited (^3E) state with three sublevels having magnetic quantum numbers $m_s = 0, \pm 1$. Here, m_s is the spin projection along the NV centre quantization axis. Additionally, the NV centres are also made up of a spin-singlet ground ($^1A_1$) and excited (^1E) states which are metastable in

[1] The optically detected magnetic resonance (ODMR) is a double resonance technique by which the electron spin state of a crystal defect may be optically pumped for spin initialization and read out [95]. Similar to the electron paramagnetic resonance (EPR), the ODMR make use of the Zeeman effect in unpaired electron.

nature.

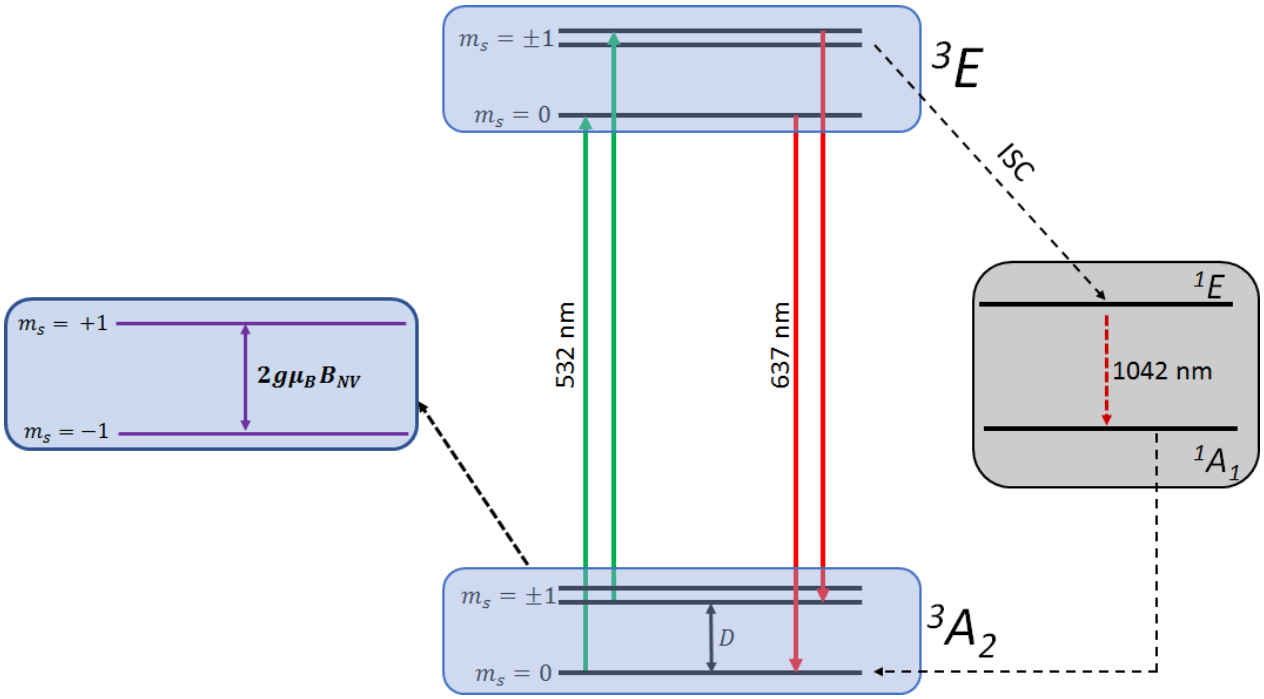

Figure 2.3: Electronic energy levels of the NV centre showing optical optical transitions and Inter-System Crossing (ISC) of the excited triplet states ($^3A_2$ and ^3E) to the excited singlet state ($^1A_1$). Optical pumping and read-out are realized using the spin-triplet ground state. In the absence of an applied magnetic field, the ground state spin state $m_s = \pm 1$ is lifted from the $m_s = 0$ due to spin-spin interaction. The frequency corresponding to this transition, D is about 2.87 GHz. Spin conservating optical transitions can occur between the levels and are represented in green and red, while non-radiative transitions can occur through the intersystem crossing (ISC). In the presence of an external magnetic field **B**, along the NV quantization axis, the degeneracy between state $m_s = \pm 1$ is lifted proportionally to the field. It is possible to detect magnetic resonances of this nature by applying a microwave field that induces transitions between the states $m_s = 0$, and $m_s = \pm 1$ when its frequency D is resonant with the transition frequency; the decrease in the photoluminescence gives rise to ODMR.

The optical transitions between the $^3A_2$ and ^3E have a 637 nm wavelength corresponding to red light, while the transition between ^1E and $^1A_1$ has a 1042 nm wavelength corresponding to infrared light [98]. Both experimental and theoretical studies have shown that the transitions have phonon sidebands due to vibrations in the diamond lattice. This phonon sideband results in the broadening of the fluorescence spectra of the NV centres [96]. To drive the $^3A_2 \longrightarrow {}^3E$, a green laser, commonly 532 nm is required. The emission from the $^3E \longrightarrow {}^3A_2$ decay is in a broad range of wavelength 637 nm to 800 nm.

The transition between states is ideally spin-conserving, however, an intersystem crossing (ISC) can also occur between the spin-triplet and spin-singlet states. Non-radiative decay can occur from ^3E to $^1A_1$ and also from ^1E to $^3A_2$ [99, 100]. Further, one can detect the spin state of NV centres and optically pump it into the $m_s = 0$ ground state sublevel. Consider for example if, the NV centre is illuminated with green light that drives the transition from $^3A_2 \longrightarrow {}^3E$. If the NV centre is initially in the $m_s = 0$ ground state sublevel, will be excited into the $m_s = 0$ excited state due to the spin conserving nature of the transition. Subsequently, the NV centre will decay back into the $m_s = 0$ sublevel emitting red fluorescence. Similarly, if the NV centre is initially in one of the $m_s = \pm 1$ ground state sublevel, it will be excited into the $m_s = \pm 1$ excited state. In the $m_s = \pm 1$ excited states, the NV centre has a probability to undergo intersystem crossing (ISC) to the singlet states. From the singlet states, the NV centre then undergo decay from $^1A_1$ to the ^1E states before going into the ground state $^3A_2$ with some 10 - 30 % chance of transitioning into the $m_s = 0$ after several excitation cycles. Furthermore, it is possible to know if the NV centre is in the $m_s = 0$ or in the $m_s = \pm 1$ by observing the intensity of the fluorescence emitted. NV centres emit less fluorescence when pumped into their $m_s = \pm 1$ than their $m_s = 0$ states, thus making the fluorescence intensity useful to determine the NV spin states. It is worthy of mention that the non-radiative ISCs to the ^1E singlet states are strongly spin-selective because their shelving rate from $m_s = 0$ sublevel is much smaller than those from $m_s = \pm 1$ [99, 100].

2.3 Relaxation Times

We define the different relaxation times associated with the NV centre. The relaxation times discussed here sets a limit on the sensitivity of NV based detection protocol and will be referred to later in this chapter.

2.3.1 Spin-lattice Relaxation Time (T_1)

The spin-lattice relaxation, T_1, also referred to as the longitudinal relaxation time is the decay lifetime for an NV polarized population to transition to the ground-state magnetic sublevel[2]. NV centres in bulk diamonds have T_1 on the order of $\sim$ 1 ms, while in nanodiamonds T_1 value is $\sim$ 100 μs [101]. T_1 relaxation of NV centres is largely dependent on temperature and magnetic field. Experimental studies showing temperature and magnetic-field dependency of the longitudinal spin relaxation time in ensemble of NV centres can be found in Refs. [102, 103]. In the study of T_1 relaxation as a function of temperature and magnetic field, it was realized that the two-photon Raman, a cross-relaxation, and an Orbach-type process are responsible for this relaxation process.

2.3.2 Spin-Spin Relaxation Time (T_2)

The spin-spin relaxation, T_2, also called the tranverse coherence time or the dephasing time describes the decay time in a spin echo experiment in which a resonant π microwave pulse is applied in the middle of a free precession interval. T_2 relaxation times are on the order of several microseconds in a spin echo experiment and can be extended with the application of multiple π pulses [104, 105]. Multiple spin echoes act like lock-in amplifiers to aid in the improvement of magnetic field sensitivity [106].

2.3.3 Spin Dephasing Time (T_2^*)

The spin dephasing time, T_2^* describes how long the phase of an NV qubit stays intact. It is the decay constant time after which an initial state $|m_s = 0\rangle$ will evolve into a superposition with the $|m_s = \pm 1\rangle$ states. To initiate T_2^*, a resonant $\pi/2$ microwave pulse is applied to superpose up and down spin states. T_2^* are typically on the order of a few microseconds, and extends into the millisecond range when isotopically pure diamond is used [107]. The spin dephasing time sets the sensitivity limits in most sensing protocols as it depends on

[2]Note that all relaxation time are not actually "time from state **a** to state **b**" but rather decay constants. For instance, the probability that a NV qubit will stay in state $|m_s = 1\rangle$ after time t, is given by the formula $P(|m_s = 1\rangle = \exp^{-\frac{t}{T_1}})$.

paramagnetic impurities such as ^{15}N, ^{29}Si, ^{13}C, ^{14}P within the diamond lattice [108].

2.4 Sensing Applications

As described earlier, the NV centre can be used to sense several physical quantities, and to understand the mechanism, it is necessary to analyze the center's spin ground state $^3A_2$ Hamiltonian in Equation 2.1:

$$\hat{\mathbf{H}} = \underbrace{D\left(\hat{\mathbf{S}_z}^2 - \frac{2}{3}\right)}_{\text{I}} + \underbrace{\gamma_e \overrightarrow{\mathbf{B}} \cdot \overrightarrow{\mathbf{S}}}_{\text{II}} + \underbrace{\epsilon_z E_z \left(\hat{\mathbf{S}_z}^2 - \frac{2}{3}\right) + \epsilon_{xy}\left[E_x\left(\hat{\mathbf{S}_x}\hat{\mathbf{S}_y} + \hat{\mathbf{S}_y}\hat{\mathbf{S}_x}\right) + E_y\left(\hat{\mathbf{S}_x}^2 + \hat{\mathbf{S}_y}^2\right)\right]}_{\text{III}}$$

$$+ \underbrace{\overrightarrow{\mathbf{S}}\mathbf{A}\overrightarrow{I}}_{\text{IV}} + \underbrace{\gamma_n \overrightarrow{\mathbf{B}} \cdot \overrightarrow{\mathbf{I}}}_{\text{V}} \quad (2.1)$$

here, D is the zero-field splitting parameter, $\overrightarrow{\mathbf{B}}$ is the vector magnetic field, γ_e is the electron gyromagnetic ratio, $\overrightarrow{\mathbf{E}}[\mathbf{E}_x, \mathbf{E}_y, \mathbf{E}_z]$ is the vector electric field, ϵ_{xy} and ϵ_z are the electric field coupling constants, $\mathbf{A}$ is the hyperfine coupling tensor, $\hat{\mathbf{S}_x}$, $\hat{\mathbf{S}_y}$, $\hat{\mathbf{S}_z}$ are the spin-1 operators in Equation 2.2, and γ_n is the nuclear gyro-magnetic ratio:

$$S_x = \frac{1}{\sqrt{2}}\begin{pmatrix} 0 & 1 & 0 \\ 1 & 0 & 1 \\ 0 & 1 & 0 \end{pmatrix}, \qquad S_y = \frac{1}{\sqrt{2}}\begin{pmatrix} 0 & -i & 0 \\ i & 0 & -i \\ 0 & i & 0 \end{pmatrix}, \qquad S_z = \begin{pmatrix} 1 & 0 & 0 \\ 0 & 0 & 0 \\ 0 & 0 & -1 \end{pmatrix} \quad (2.2)$$

In the very low magnetic field regime, typically less than 5 Gauss, term I (zero-field splitting term) in Equation 2.1 is the only dominating interaction and the rest can be approximated as perturbations. The zero-field splitting term arises from spin-spin interaction between two unpaired electron of the NV centre. In general, the term I is a trace zero matrix that describes the energy level splitting at zero magnetic field in spin S > 1/2 systems. The parameter D in I term is highly sensitive to temperature fluctuations and could limit the sensitivity of NV

magnetometers. In the following paragraphs, the remaining terms in the Equation 2.1 are described.

Term II is the Zeeman term, and it describes the magnetic field coupling to NV centre electron spin; experiments later in this thesis are based on this coupling. The value of γ_e in Equation 2.1 is approximately 28.0 GHz/T. Suppose a magnetic field $\mathbf{B} = B_z\mathbf{z}$ is aligned along the NV quantization axis (chosen as the $\mathbf{z}$ direction by convention), a splitting in the $m_s = \pm 1$ sublevel is observed and the energies of the m-sublevels is given by Equation 2.3 and shown diagrammatically in Figure 2.4

$$E(m) = Dm^2 + \gamma B_z m \tag{2.3}$$

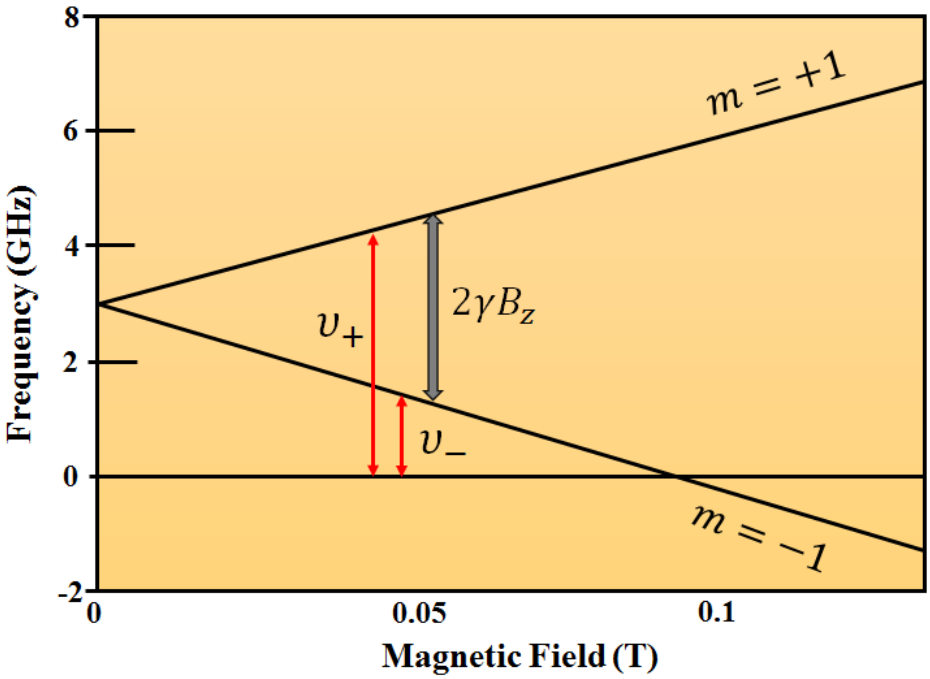

Figure 2.4: A schematic of the energy level diagram of a NV centre as a function of applied external magnetic field aligned along the NV axis. The transition frequencies m = 0 ↔ +1 and m = 0 ↔ -1 are denoted as ν_+ and ν_- respectively.

The applied magnetic field can be determined through the detection of the Zeeman shifts of the NV defect ground state spin sublevels. Note that the energies of the $m_s = \pm 1$ sublevels

depends linearly on the applied magnetic field - the principle of the NV magnetometry is based on the optical detection of this energy shift.

Similar to the interaction of NV centres with magnetic fields, term III in Equation 2.1 known as the Stark term describes the electric field coupling to the NV centre, where ϵ_{xy} and ϵ_z are the longitudunal and transverse components of the coupling respectively. The use of NV centres as an electric field sensor has been investigated extensively [46, 109], although coupling co-efficient reported in Refs. [46, 109, 110] indicate that the NV centres are less sensitive to electric fields. Additionally, the NV centre is also sensitive to stress/strain via the piezoelectric effect. Finally, term V is the nuclear Zeeman interaction describing the relationship of nuclear spins with the external magnetic field and it is small enough that it can be neglected in the Hamiltonian. The nuclear spin Zeeman interaction is usually isotropic and thus expressed in terms of the gyromagnetic ratio of the nuclear species, $\gamma_n = \mu_n g_n$.

2.5 Engineering NV Centres in Diamond

For magnetic field sensing applications, the minimum detectable sensitivity for a single NV centre scales as:

$$\eta \propto \frac{1}{C_o \sqrt{I_o T_2^*}} \tag{2.4}$$

where C_o is the contrast of the optically detected magnetic resonance spectra, I_o is the intensity of detected photons, and T_2^* is the inhomogeneous spin dephasing time of the NV centre. All variables listed in Equation 2.4 can be modified to improve sensitivity except C_o which depends on the photophysical properties of the NV defect. From a materials engineering standpoint, the only parameter that can be tuned to improve sensitivity is the spin dephasing time T_2^* of the NV spin sensor [111]. T_2^* is limited by the interaction of NV spins with other paramagnetic impurities present at the surface and within the diamond matrix [44].

Thus, for optimized magnetic field sensitivity, diamond samples with low impurity content are highly desirable to prolong coherence time. In particular, NV centres located very close to the surface are prone to electronic spin noise generated from the spin bath at the surface contributing to poor spin dephasing time [112]. A series of chemical treatment and surface termination has been reported to improve the spin coherence time of NV centres located close to the diamond surface [113, 114]. An alternative to this method might involve the use of in-plane Schottky-diode geometries [115] to manipulate charge state conversion, or the introduction of advanced pulse sequences to prolong T_2^* [44, 116].

While the single NV centre has drawn attention numerous attention with regard to their applications, one can further improve the sensitivity of detection by introducing an ensemble of NV centres:

$$\eta \propto \frac{1}{C_o\sqrt{N}\sqrt{I_o T_2^*}} \tag{2.5}$$

in Equation 2.5, N represents the NV centre density. A critical challenge for material scientists is how to engineer an ensemble of NV centres while still maintaining good coherence. Furthermore, NV centres can be oriented along four possible < 111 > crystal directions, and this leads to decreased sensitivity. This is because one-fourth of the ensemble of NV centres can only be used for detection, while others contribute towards background photoluminescence. In summary, some challenges of engineering NV centres in both SCDs and PCDs for magnetic field detection are as follows:

- Incorporating dense NV centres in PCDs at low pressure: A wide-field magnetic field detection and imaging is made possible and cheaper with PCDs containing an ensemble of NV centres grown over wide areas. The use of commercially available chemical vapour deposition (CVD) diamond machines with permissible operating pressure below 40 Torr has not been very effective in the incorporation of surface NV centres over large areas. Additionally, successful incorporation of an ensemble of NV centres in both SCDs and

PCDs may further require the optimization of growth parameters to enhance NV spin dephasing times.

- Controlling surface charge state stability: In most cases, NV centres located within a few nanometers from the diamond surface are found in their neutral charged states [90]. Certainly, there is a need to understand the mechanism of charge state conversion in both SCDs and PCDs. Commonly studied is the mechanism of NV centre formation and charge state conversions in SCDs. However, to date, there have been no studies explicitly detailing the same in PCDs.

- Controlling NV orientation: The engineering of preferentially oriented NV centres is targeted at limiting unwanted background noise, increasing sensitivity, and simplifying device operation [111]. While the preferential orientation of NV centres has been achieved in SCDs [117, 118], this result remains a nightmare in PCDs because of the random orientation of grains.

In recent times, a variety of methods have been explored to place NV centres in the diamond matrix while in turn solving some of the challenges listed above. The requirements for post-processing, spatial localization of NV centres, and coherence times strictly depend on the method employed. Here, we review three commonly known methods for the engineering of NV centres in diamonds, namely electron irradiation, ion implantation, and the CVD approach.

2.5.1 Irradiation and Annealing Technique

The creation of NV centres in diamond depends on the presence of substitutional nitrogen (N_s) and vacancies (V) in the diamond lattice [119]. High-pressure-high-temperature (HPHT) fabricated diamonds contain substitutional nitrogen at about 100 ppm. As a result, HPHT diamonds have been used to create high-density ensembles of NV centres using the irradiation technique. This process involves four stages as shown in Figure 2.5.

First, a type-Ib SCD fabricated using HPHT method is obtained. Typically, the concentration of nitrogen impurities in these samples ranges from about 100 - 200 ppm. Subsequently,

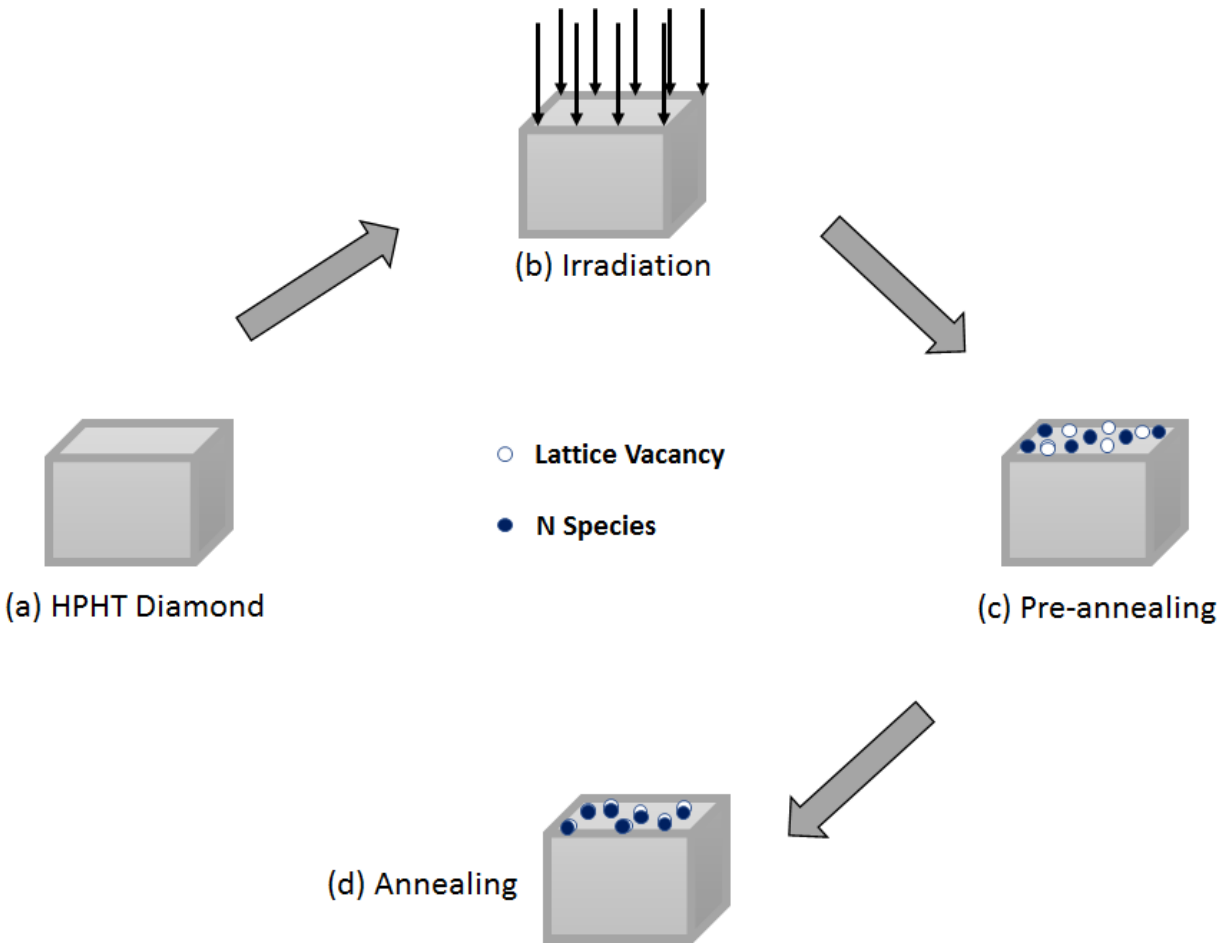

Figure 2.5: Schematics showing the experimental processes involved in the irradiation technique for the synthesis of NV centres in diamond; from irradiation to the annealing process. (a) HPHT SCD containing 100 - 200 ppm N_s is prepared for irradiation (b) SCD is irradiated using particles such as protons, electron, or neutrons (c) Vacancies are created as a result of the irradiation process (d) The irradiated SCD is annealed above 700^oC to allow the diffusion of vacancies through the crystal and to recombine with nitrogen atoms. NV^o (P1) centres may be initially formed, subsequent capture of an electron by P1 centres will result in the formation of NV^- centres.

vacancies are formed in the diamond samples by bombarding them with high energy particle irradiation [120], such as electrons, neutrons, protons or ions. The particle beam interacts with the diamond crystal, displacing carbon atoms in the lattice and leaving behind vacancies [119]. The diamond samples are then subjected to a thermal annealing process above 700^{o}C allowing vacancies to diffuse through the crystal lattice and recombine with the intrinsic nitrogen atoms present in the diamond [121]. The resulting NV centre concentration from this method depends on the initial concentration of N_s as well as the irradiation and annealing parameters [122]. This method has been used for a long time in the fabrication of NV^- centres due to its high efficiency and low-cost. In spite of this, the large concentration of intrinsic nitrogen does not allow for control down to a single optical centre [123]. Furthermore, the presence of other defects in type-Ib diamond in addition to the N_s crucially affects the spin dephasing times of NV centres. Past efforts have been tailored towards understanding the relationship between irradiation doses and the spin relaxation times. Results have shown that high irradiation doses induce electron spin resonance linewidth broadening and longitudinal relaxation rate growth [124, 125]. Additionally, using lower irradiation energies increases the ratio of centres in the negatively charged states compared to the neutral one. Also, annealing at 900^{o}C after irradiation reduces the spin resonance linewidth. Via parameter optimization, efforts have been made to improve the spin dephasing times and lifetimes of NV centres fabricated using this method, nevertheless, it is still impossible to isolate single NV centres using this process.

2.5.2 Ion implantation and Annealing Technique

Contrary to the use of HPHT diamonds in the irradiation technique, unwanted impurities leading to an inhomogeneous broadening of NV centres can be avoided by starting with ultra-high purity diamonds and implanting nitrogen to achieve the desired properties. Type IIa diamonds having less than 1 ppb nitrogen concentration are used for this purpose. Pure diamonds of this kind are not commonly found in nature and must be fabricated synthetically. A host of diamond vendors such as Element Six (`www.e6.com`) and Sumitomo (`sumitomoelectric.com`) have made tremendous progress in improving the quality of CVD diamonds over time. Ion implantation has an advantage over other techniques because it can

be used to control the spatial localization of NV^- centres in diamonds. The process of ion implantation and annealing is explained diagrammatically in four steps in Figure 2.6 . This process begins with the bombardment of nitrogen ions (N^+) in ultra-high purity diamond sample. Although other molecules containing nitrogen such as N_2^+, and CN^+ can be used as demonstrated by Haruyama et al. in Ref. [126]. During the process of implantation, high energy ion bombardment creates Frankel pairs as well as other damage in the diamond lattice [127].

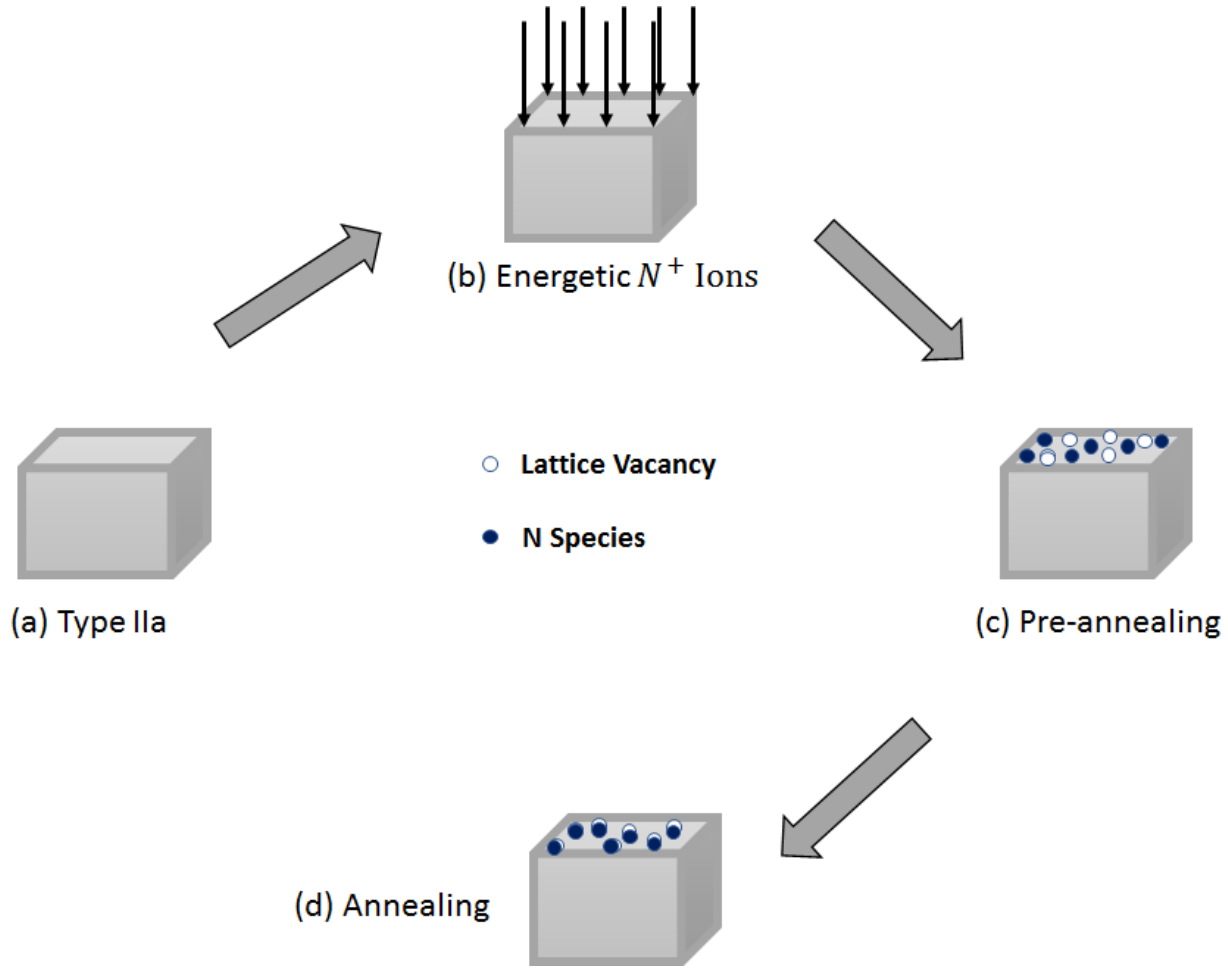

Figure 2.6: Schematics showing the ion implantation process in four stages. (a) Type IIa diamonds containing less than 1 ppb nitrogen in concentration is prepared for ion implantation. (b) Diamond samples are bombarded with nitrogen ions. (c) Vacancies are created resulting from the ion bombardment process (d) The ion implanted sample is annealed above 700°C to allow the diffusion of vacancies through the crystal and to repair damages formed from heavy ion bombardment.

The samples are then annealed at a temperature of about 700 - 1000°C, thus providing energy

for the diffusion of the defects. At the same time, Frenkel pairs[3] may split and produce isolated vacancies or self-interstitial following an arbitrary direction of motion [128]. Due to the mobility of self-interstitials, they may tend to aggregate to the surface, or grain boundaries or form layered defects. During the annealing process, these types of luminescence quenching defects are healed. From previous studies, it is well known that NV centres are formed after the annealing process when vacancies get trapped in N_s sites. The annealing process is a quasi-equilibrium process, and an insight into the creation of NV^- centres can be gained by understanding the formation energies and occupation levels of the defects. An elaborate study of the kinetics involved in the process is the topic of discussion in the work of Haque and Sumaiya [128].

Many quantum applications require bright, single, and photo-stable NV centres located in proximity to the diamond surface, and it is known that the irradiation technique which makes use of intrinsic nitrogen impurities cannot be used as a fabrication technique for this purpose. A useful method for the isolation of a single NV centre via ion implantation typically makes use of a different isotope of nitrogen for bombardment. For example, ^{15}N can be implantation into type IIa diamond, then optically detected magnetic resonance technique (ODMR) can be employed to measure the hyperfine coupling of the NV^- centre. It is possible then to discriminate the NV centre(s) arising from the implanted ^{15}N from that created by the native ^{14}N sites. Analysis done by Rabeau and Reichart, 2006 [129] indicates that 1 in 40 implanted ^{15}N atoms give rise to an optically observable NV^- centre. For NV centres created by ion implantation, the proximity to the surface is determined by the ion energy and by the vertical diffusion of vacancies that occurs during the annealing process [123]. Furthermore, ion implantation has been used to fabricate coupled NV centre pairs with applications in quantum information processing [126].

Regarding the stability of charge states, it is possible to manipulate charge states of vacancies

[3]Frenkel defects discovered by Yakov Frenkel occurs when an atom leaves its position thereby creating a vacancy and subsequently becomes interstitial by taking a nearby location.

by implanting nitrogen into n-type diamonds instead of into a standard crystal. Using n-type diamonds promotes negative charge states of vacancies, favours clustering of NV centres for charge transfers, and reduces the probability of single NV centre formation [111]. The challenges of short spin coherence times of qubits produced by ion implantation are presumably due to residual radiation damage. Results in Refs. [130, 131, 132] have shown that high-temperature annealing at about 1000 - 1200^{o}C allows an improvement in the spin coherence times to about 1.5 ms at room temperature. Also, the annealing process reduces the fraction of NV^- centres converting into NV^0. This result indicates that thermal treatment of ion-implanted diamond samples leads to a substantial decrease in the paramagnetic residual defects. The catch here for improvement in coherence time is the optimization of annealing temperature being above 1200^{o}C can lead to diminishing coherence properties.

2.5.3 In situ CVD Doping Technique

The ion implantation technique is good for obtaining spatially localized NV centres, however, obtaining excellent coherence properties using this method is still debatable. Intentional nitrogen (N_2) doping during CVD growth has recently been used to fabricate NV centres with good coherent properties. The CVD technique simultaneously allows the growth of a high-quality diamond while forming NV centres. Furthermore, a major advantage of using the CVD method is the ability to grow diamond samples heteroepitaxially on different substrates including silicon and quartz. Diamond films containing NV centres can be synthesized in the laboratory using a hot filament chemical vapour deposition (HFCVD) or the microwave plasma-enhanced chemical vapour deposition (MPECVD) technique. Although both techniques involve diluting a small quantity of methane in excess hydrogen gas, the MPECVD is known to be a more effective technique for preparing high-quality films in comparison to the HFCVD. This is because the HFCVD generates an electrode plasma discharge which affects the quality of deposited films [133].

Figure 2.7 shows a schematics of the process involved in the deposition of diamond with NV centre using a plasma-assisted chemical vapour deposition technique (MPCVD). The deposition can either be homo-epitaxial; on a diamond substrate or hetero-epitaxial, where

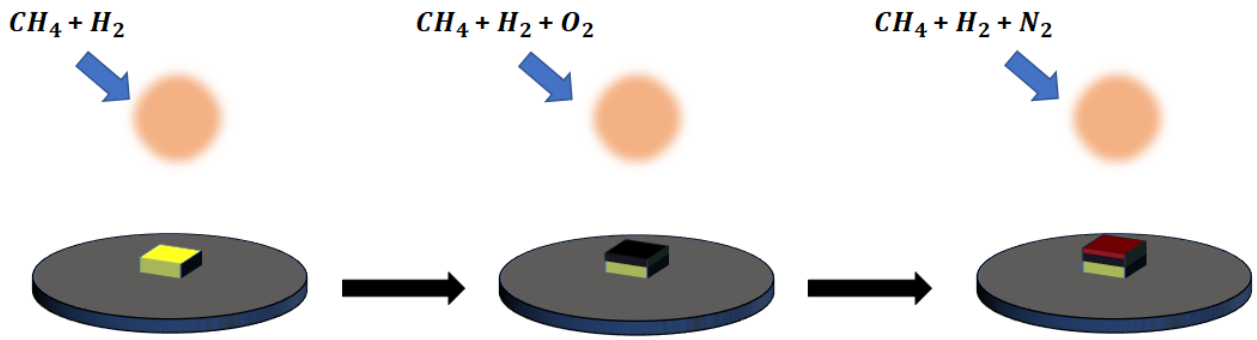

Figure 2.7: Schematics showing the stages involved in the insitu nitrogen doping of diamond. The chemistry of each stage is explained comprehensively in the paragraphs below.

deposition occurs on a foreign substrate other than diamond. The deposition is plasma-assisted and usually carried out in a 2.45 GHz MPCVD reactor. An advantage of using the 2.45 GHz reactors arises from the higher plasma density with higher energy electrons produced at this frequency. Certainly, the higher plasma density is expected to result in higher concentrations of atomic hydrogen and hydrocarbon radicals. Importantly, in the MPCVD method, plasma is densely concentrated at the centre in the form of a sphere preventing carbon deposition on the chamber walls.

Before the growth process schematically shown in Figure 2.7, substrates are always pre-treated. The treated substrates are then introduced into the reactor at a baseline pressure of $\sim 1.0 \times 10^{-6}$ Torr. Operating at this baseline pressure eliminates unwanted residual gases in the reactor. Diamond film deposition commences with an introduction of CH_4 with H_2 being the carrier gas. The gases are dissociated according to the equation below using the microwave plasma discharge:

$$H_2 \longrightarrow 2\,H$$

$$CH_4 + H \longrightarrow CH_3 + H_2$$

The formation of CVD nitrogen doped diamond can be described in steps using a modified form of the Goodwin model [134].

1. First $k1$ active sites Ac^* are generated prior to diamond deposition by an abstraction reaction of adsorbed hydrogen atoms from the gas phase (R_1).

$$Ac - H + H \longrightarrow Ac^* + H_2 \qquad (R_1)$$

2. Then $k2$ of those active sites are re-occupied by atoms from the gas phase (R_2).

$$Ac^* + H \longrightarrow Ac - H \qquad (R_2)$$

   The two reactions described above define the ratio of the open sites, $k1/(k1 + k2)$ which depends solely on the surface temperature.

3. On the addition of nitrogen gas, the active sites can receive nitrogen atoms and methyl radicals joining the diamond crystal lattice by successive abstraction reactions.

$$Ac^* + CH_3 + N_2 \longrightarrow Ac - H_3CN + N \qquad (R_3)$$

$$Ac^* - H_3CN + N + H \longrightarrow Ac - H_2CN^* + N + H_2 \qquad (R_4)$$

Oxygen added in a small amount can help reduce non-carbon phases hence purifying the deposited diamond. This stage is sometimes necessary before the introduction of the dopant gas. By using this method, one can control the dopant concentration which in turn determines the density of NV centres obtained. Using the CVD method has resulted in a long spin dephasing time for the NV centre ensemble. Ultralong spin coherence times close to 2.0 ms [44, 135] with a magnetic field sensitivity of about 4 $nTHz^{-1/2}$ has been obtained. In a similar vein, further improvement in the charge state stability which translates into improved sensitivity is achieved using selective surface termination methods. Such methods involve the use of acid treatment that can serve as an oxidizing agent or passing gas (e.g. ozone, oxygen, or nitrogen) while annealing at a temperature of about 450^oC to functionalize NV centres. Results obtained so far shows improved NV^- centre stability and coherence times using chlorine surface functionalization [114, 136]. Lastly, preferential alignment of NV centres is usually achieved using the MPCVD technique when nitrogen-doped diamond is homoepitaxially deposited on a < 111 > oriented diamond, albeit recent work on NV centre engineering have shown that the same can be achieved on < 113 > oriented diamonds with

a partial orientation of about 73 % [118]. Evidence shows that majority of the aligned NV centres were formed by nitrogen first aligning itself along the < 111 > growth surface and then followed by the formation of vacancies on top [137, 138].

It is not untrue that most of the previous work on NV incorporation in diamond has been performed with nanodiamonds and SCDs. Deposition of NV centres has also been mostly performed under HPHT conditions. It appears that controlled formation of NVs in PCDs at low-pressure-low temperature (LPLT) conditions will save the cost of production which will be beneficial when multi-diamond sensors containing an ensemble of NV centres is desired for any application. For successful control of the NV centres in PCDs grown under LPHT conditions, the following questions need answers. What nitrogen configuration is assumed at low-pressure growth? How do we incorporate dense ensemble of NV centres during low-pressure growth? What will be the effect of surface termination on NV centres in PCDs? Most importantly, what is the mechanism of colour centre formation in PCDs deposited at low pressure? This dissertation provides extensive findings to answer most of these questions in chapter 3 and chapter 4. It should be mentioned that the original manuscripts underlying these chapters have been modified for inclusion in this dissertation.

Chapter 3

Experimental insights into the Engineering of NV centres in PCDs at low pressure

"I like pressure. Diamonds are made under pressure, and I definitely enjoy it."

– Caroline Buchanan

This chapter is based on the manuscript:

Ejalonibu, H. A., Sarty, G. E., & Bradley, M. P. (2019). Optimal parameter (s) for the synthesis of nitrogen-vacancy (NV) centres in polycrystalline diamonds at low pressure. *Journal of Materials Science: Materials in Electronics, 30*(11), 10369-10382.

3.1 Introduction

Nitrogen-vacancy (NV) color centres in diamonds have attracted much attention in the last few decades owing to their long spin coherence time, stability at ambient temperature, and their ability to be manipulated/controlled by laser and microwave pulses [139, 138]. Novel applications of NV centres found in diamonds include quantum information processing, nanoscale thermometry, magnetic field sensing, and single-spin nuclear magnetic resonance [109, 139]. The NV centres are known to exist in two main charge states namely the neutral charged (NV^0), and the negatively charged (NV^-) states as mentioned earlier in 2. The aforementioned charge states have distinct optical and spin properties. However, for several quantum applications, only the NV^- centre is a sought-after candidate due to its unique

spin properties. In the last few decades, research attention has been directed towards the study of the incorporation of impurities in the CVD growth process of SCDs and PCDs. In particular, the incorporation of nitrogen in PCDs grown using the CVD technique has been a major topic of interest for two reasons. First, PCDs grown over non-diamond substrates have the potential of holding large ensembles of NV^- centres (a high concentration of NV^- centres are prerequisite to improving the sensitivity of NV sensing protocol), thus making them a favourable candidate for wide-field magnetic field sensing. In addition, PCDs with a desired concentration of NV^- centres can be obtained in large quantities and at lower cost, hence it is a cost-effective option in applications where NV sensor arrays are needed. Surprisingly, up to now, few works have focused on the incorporation of nitrogen impurities in PCDs for the formation of NV^- centres due to the complexity involved in the process. For example, the incorporation of nitrogen impurities in PCDs might lead to the formation of single substitutional nitrogen, vacancies with complexes, lattice defects or even nitrogen located at grain boundaries. Each of these bonding configurations is formed under different conditions, therefore, precisely controlled growth parameters (most especially, the nitrogen flow rate) are required. In this chapter, we develop experimental insights into the engineering of NV centres in PCDs at low deposition pressure. This objective was achieved by examining the influence of nitrogen flow rates on the formation of NV^- centres in PCDs deposited at low pressure of about $\sim$ 30 Torr. The study is essential because it provides information for the growth of PCDs at low pressure conditions suitable for sensing applications.

3.2 Experimental

3.2.1 Diamond Film Preparation

The PCD films used for this study were deposited hetero-epitaxially on a $< 100 >$, $3 \times 3 \times 0.5$ mm^3 p-type boron doped silicon substrate of resistivity 5 Ωcm (Silicon Material Inc., NV, USA) in a 2.45 GHz Microwave Plasma Chemical Vapour Deposition (MPCVD) reactor (Plasmionique Inc., QB, Canada) with operating power between 0.2 and 1 kW. In order to prevent the cracking of the quartz window, the reactor was not operated at maximum power.

It is also important to mention that the chamber is designed to operate at low pressure, therefore plasma becomes unstable above 50 Torr. Figure 3.1 shows a cross-sectional schematic of the MPCVD reactor used in this part of our work. The reactor chamber is made of quartz window of diameter 30 mm in the centre of the wall of a compressed waveguide. A stainless steel disk of about 11 cm serves as the substrate holder in the deposition chamber and the substrate holder is water cooled. Microwave power is transmitted into the cavity using a rectangular waveguide, converting the TE10 microwave mode into the TM01 mode in the cavity. We observe that the plasma density is highest in the region close to the substrate surface. Also, it is our assumption that the substrate is at the temperature of the substrate holder and by choosing the thickness of the holder and the cooling rate, the substrate holder's temperature can be controlled.

Prior to diamond deposition, the silicon substrates used for growth were nucleated by treating the surface with a mixture of diamond powder and ethyl-alcohol in an ultrasonic bath for 30 minutes. This process, known as seeding is done in order to achieve a uniform growth of coalesced films on the silicon substrate. The seeding process can be achieved by using different techniques - interested readers are referred to the review article of Mandal. 2021 [140] for a detailed summary of the different seeding techniques available. The MPCVD chamber was then evacuated to a baseline pressure of 4.9×10^{-3} Pa using a turbo molecular pump. At this baseline pressure, a little percentage of nitrogen gas is trapped in the chamber hence making it possible to define low nitrogen flow rates without the deliberate addition of nitrogen gas. Gas mixtures consisting of hydrogen, methane, and nitrogen ($H_2/CH_4/N_2$) were varied in the reactor chamber as shown in Table 3.1. Diamond deposition was carried out at 800 W microwave power and ~ 30 Torr pressure. The duration of each deposition run was 14 hours. For samples in the medium and high nitrogen flow regimes, nitrogen gas was introduced for a period of time close to the end of the experiment, see details in Table 3.1.

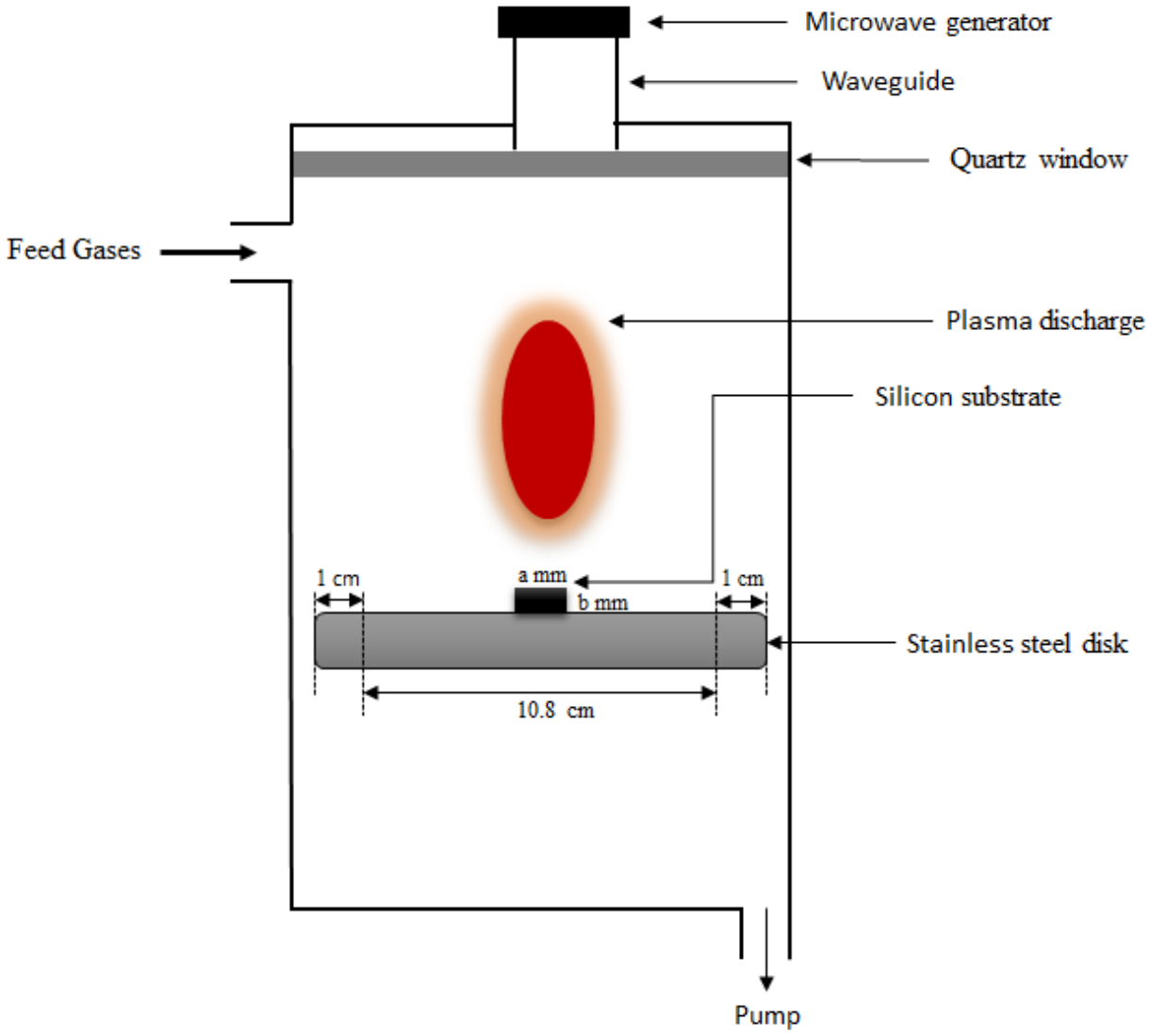

Figure 3.1: Schematic illustration of the MPCVD reactor. The reactor chamber is made of quartz window of diameter 30 mm in the centre of the wall of a compressed waveguide. The manufacturer's details on the construction of the reactor may be found in Ref. [141]

3.2.2 Diamond Film Characterization

The microstructure and photoluminescence (PL) of the samples were studied using micro-Raman (μ-Raman) Spectroscopy (Renishaw InVia, ON, Canada) equipped with a Modulaser StellarPro50 Ar - ion laser. Raman spectroscopy can be used to detect structural defects and stress distribution in materials [142, 143]. The Ar^+ laser line at 514 nm from the spectrometer is passed through a tunable excitation filter. Subsequently, the resulting scattered light is collected in a 180° back-scattered configuration with a charged-coupled device (CCD) detector. All Raman and PL spectra were fitted with a sum of Lorentz functions (using the WiRE Raman Renishaw software) to identify peaks of interest. The Raman signals were collected using a 50× (NA = 0.75) objective focusing the beam on a 20 μm diameter spot. Spectra collected from 10 different spots on the samples were averaged. The PL emissions were collected using a 20× (NA = 0.40) objective focusing the beam on a 50 μm diameter spot. For each spectra acquisition, a grating of 1200/mm, and a laser power of 10 mW with an exposure time of 10 s was used.

The reflectance spectra of the diamond films were collected using a USB-650 Red Tide UV-Vis spectroscopic reflectometer (Ocean Optics Inc., FL, USA). Reflectance measurement using a back-scatter fiber optics probe were taken at normal incidence. Measurements were taken with an exposure time of 100 ms. Field Emission Scanning Electron Microscopy (FE-SEM, Hitachi SU8000, Tokyo, Japan) was used to characterize the surface morphology of the samples. Electron micrographs were taken using an acceleration voltage of 3 KV and 15× magnification. In the results and discussion section that follows, samples were compared in groups. This means samples grown with the same hydrogen and methane concentration were categorized into the same group while the nitrogen flow rate was varied. Here, 0 sccm, 1.5 - 4 sccm, and 10 - 40 sccm represent the low, medium and high nitrogen flow rate doping regimes respectively.

Table 3.1: Growth parameters for the deposition of diamond films on silicon substrate at ~ 30 Torr pressure, 800 W microwave power, and deposition temperature of 700^0C. Parameters include doping time (in hours), hydrogen, methane, and nitrogen flow rates. All volumetric flow rates are in standard cubic centimeters per minute (sccm).

Group	Samples	$H_2/CH_4/N_2$ (sccm)	Growth time (hrs)	Doping time (hrs)
	S1	100 / 1 / 0	14	0
1	S5	100 / 1 / 1.5	13	1
	S9	100 / 1 / 10	13	1
	S2	200 / 1 / 0	14	0
2	S6	200 / 1 / 2	12	2
	S10	200 / 1 / 20	12	2
	S3	300 / 0.75 / 0	14	0
3	S7	300 / 0.75 / 3	13	3
	S11	300 / 0.75 / 30	11	3
	S4	400 / 0.5 / 0	14	0
4	S8	400 / 0.5 / 4	10	4
	S12	400 / 0.5 / 40	10	4

3.3 Results

3.3.1 Physical Appearance and Raman Spectra of Films

Table 3.2 summarizes the data obtained from micro-Raman analysis and visual inspection of samples. The full width half maximum (FWHM), centre of the diamond peak, and colour of films were reported. From the Table 3.2, it is evident that the colour of deposited diamond changes depending on the amount of nitrogen impurities in the sample. Polycrystalline CVD diamonds grown heteroepitaxially without the addition of nitrogen impurities appeared grey in colour. Those grown with nitrogen impurities show a range of colours depending on the concentration of nitrogen in the sample.

Table 3.2: Characteristics of the deposited samples: full width at half maximum (FWHM) of diamond peaks and center of diamond peaks were obtained from the Raman spectra. Colour of deposited diamonds changes depending on the amount of nitrogen impurities in samples. In particular, diamonds doped with a high concentration of nitrogen impurities appear black in colour.

Group	Sample	FWHM (D) (cm^{-1})	Center of Diamond peak (cm^{-1})	Color
	S1	8.232	1331.2	Grey
1	S5	7.695	1331.7	Lustrous grey
	S9	7.792	1332.0	Lustrous grey
	S2	10.989	1331.3	Grey
2	S6	11.268	1331.9	Lustrous grey
	S10	8.875	1331.9	Lustrous grey
	S3	8.201	1332.0	Grey
3	S7	13.320	1331.2	Grey
	S11	14.662	1332.5	Black
	S4	8.586	1331.5	Grey
4	S8	8.752	1331.4	Dark grey
	S12	15.463	1333.8	Black

Figures 3.2a and 3.2b show the Raman spectra of diamond films in group 1 and 2. The spectra of films were presented with no particular preference, for this reason, the Raman spectra of films in group 3 and 4 showing similar behaviour but with different characteristics were not shown here. In these samples, we observe silicon peaks around 519 cm^{-1}, diamond peaks around 1332 cm^{-1}, D-band around 1345 cm^{-1}, and G-band around 1500 - 1600 cm^{-1}. The presence of both D and G-band results from amorphous carbon (sp^2) related content located in the grain boundaries [144] of PCDs. As seen in Figure 3.2c, films grown with medium nitrogen flow rate in group 1 and 2 (i.e. S5 and S6) exhibit almost similar spectra. The presence of this feature indicates that it might be difficult to differentiate spectra of films with quasi-similar nitrogen and methane concentrations during CVD [89].

The FWHM of a peak obtained from Raman spectroscopy gives an indication of the structural distribution of a material. For example, a crystalline material will show narrower peaks when compared to an amorphous materials. It can also indicate the amount of disorder or defect density incorporated into the material [145]. From Table 3.2, reported FWHM for diamond deposited on silicon (100) substrate is in the range 7.8 - 15.5 cm^{-1}. The observed FWHM of the deposited films is in good agreement with reported values in [144]. In reference to Figure 3.2d, it can be seen that films doped with high nitrogen flow rate (30 - 40 sccm) in group 3 and 4 have larger FWHM than their counterparts.

3.3.2 Morphology of Films

Figure 3.3 shows the SEM micrographs of films. Distinct surface morphology is clearly exhibited with a variation in nitrogen concentration. Without the introduction of nitrogen impurities in the gas phase, the films consist of randomly oriented grains with rough surfaces. Samples doped with low and high nitrogen flow rates have particle sizes ranging from 1.3 μm - 2.5 $\pm$ 0.1 μm as calculated from Origin software. The difference in grain sizes for these samples may be attributed to the different flow rates of hydrogen, methane, and nitrogen feed gas used. With the incorporation of medium (1.5 - 2 sccm) nitrogen flow rate in the gas phase mixture, surface morphology reveals dense nano-sized grains in the films. The grain size of the nanocrystalline films were calculated using the model reported by Cançado et al.

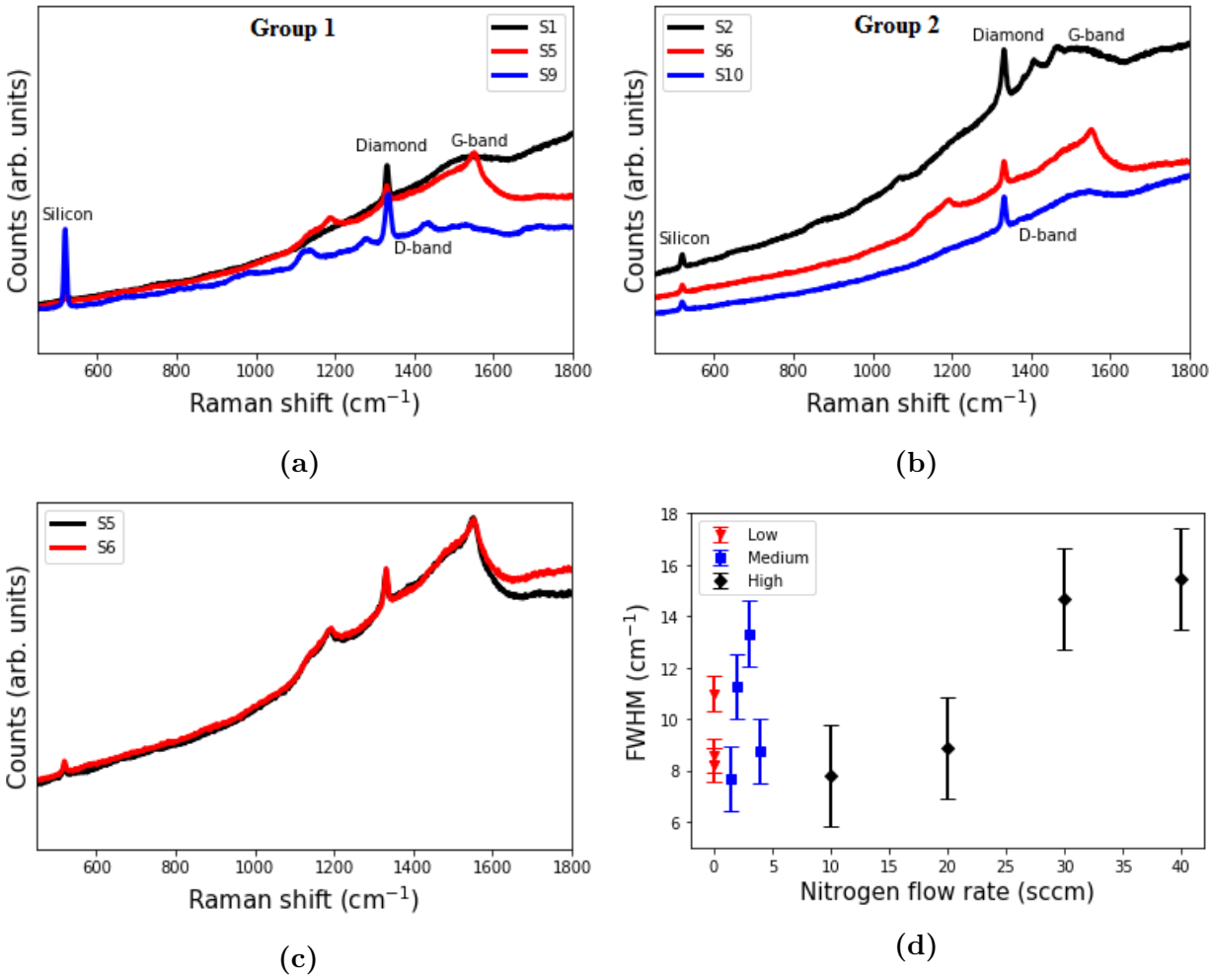

Figure 3.2: Raman spectra of some deposited films (a) Raman spectra of films in group 1 (b) Raman spectra of films in group 2 (c) Raman spectra of films with medium nitrogen flow rate in group 1 and group 2, both films were deposited with similar methane and nitrogen concentration and have shown similar spectra indicating that it might be difficult to differentiate spectra of films with quasi-similar nitrogen and methane concentrations. (d) FWHM of diamond peaks against nitrogen flow rate, films with high flow rate (30 - 40 sccm) show larger FWHM.

[146] as shown in Equation 3.1,

$$L_a(\text{nm}) = (2.4 \times 10^{-10})\lambda_l^4 \left(\frac{I_{Da}}{I_G}\right)^{-1} \tag{3.1}$$

where λ_l is the laser line wavelength (514.5 nm) used in the measurement; I_{Da} and I_G are the integrated intensities of the diamond and graphitic bands. Nano grained samples have grain size of 21 ± 0.46 nm.

To further validate results from Raman spectroscopy, the surface morphology of samples grown with medium nitrogen flow rates in group 1 and 2 (S5 and S6) were observed. These films have similar morphological features. A closer observation from the SEM micrographs revealed the presence of cracks in the sample S6 (see Figure 3.3e) which might be due to stress and as a consequence led to an increase in the FWHM of this sample. With regards to the previous physical observation for highly doped diamonds, surface morphology of sample S12 (as in Figure 3.3l) show heavily defective diamond grains with grains having several surface pores.

3.3.3 Photoluminescence (PL) and Reflectance Spectra of Films

For the films to be used for sensing applications, the presence of optically active NV^- centers located close to the surface is important. To investigate the incorporation of surface optical centers, a room temperature photoluminescence (PL) measurement was performed. Figure 3.4 - 3.5 show the PL spectra of films. The observed sharp distinguishable peaks in the spectra are at 515, 529, and 552 nm. The 515 nm lines are due to the Ar ion laser; the 529 nm lines are due to the silicon substrate, and the 552 nm peaks are that of diamond [147]. Broad peaks due to amorphous related elements are observed between 555 - 560 nm. Neutral optical centers peak (NV^0) occur around 575 nm, while negatively charged optical centres have peaks around 637 nm (NV^-) [148, 109, 149]. Shown in Figure 3.6b is a normalized intensity bar graph of samples having nitrogen related optical features that can be harnessed for sensing. From Figure 3.6, sample S8 in group 4 has the greatest intensity of NV^0 as measured by PL spectroscopy, while S10 in group 2 has the lowest intensity.

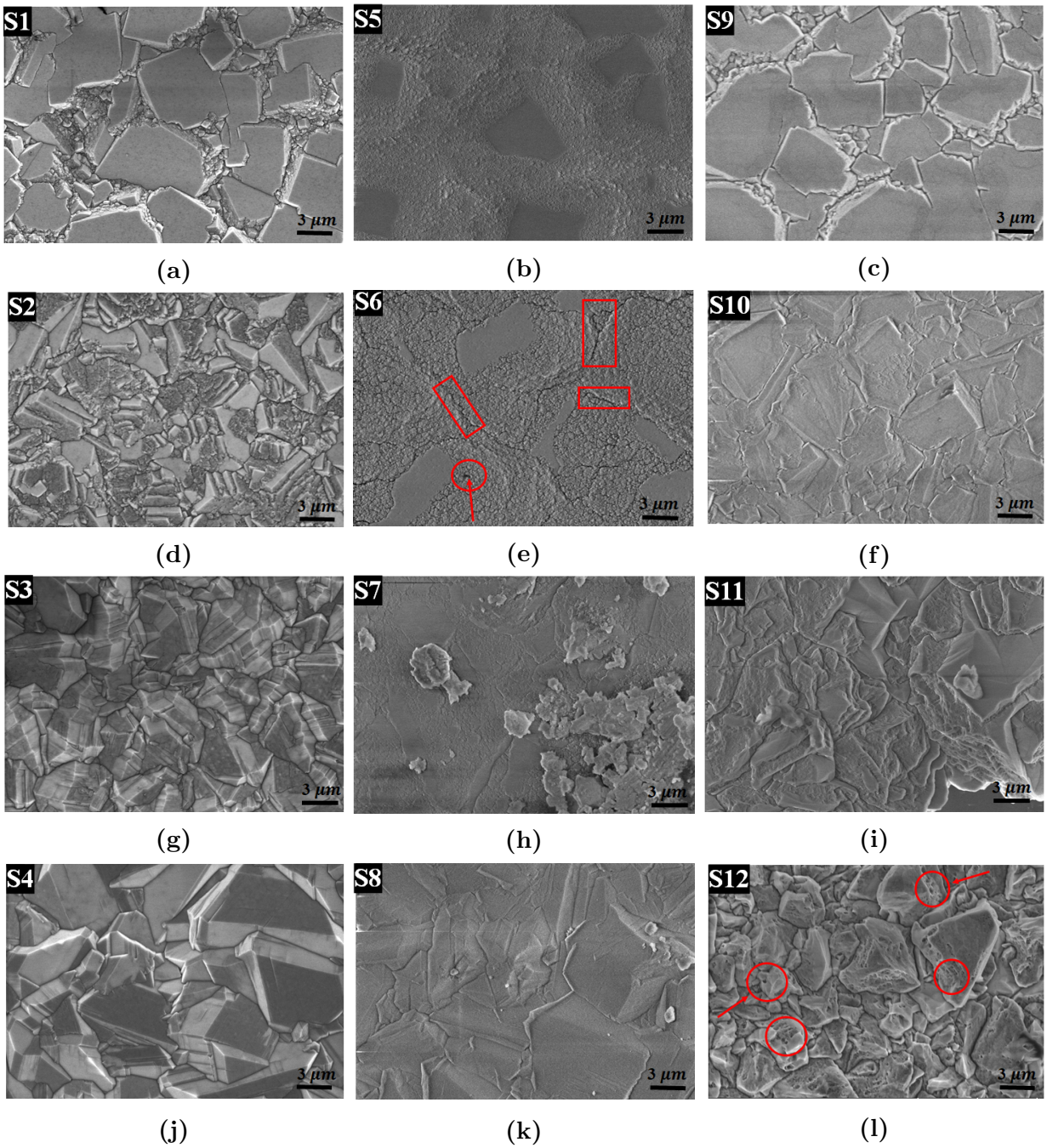

Figure 3.3: Surface morphology of films (a - c) surface morphology of samples in group 1 (d - f) surface morphology of samples in group 2 (g - i) surface morphology of samples in group 3 (j - l) surface morphology of samples in group 4.

In using this material for magnetic sensing applications, a reasonable photon collection efficiency should be achieved. NV centres suffer from a finite collection efficiency and light trapping due to total internal reflection and imperfections [150] in the host diamond. The imperfections reduce the contrast of optically detected magnetic resonance (ODMR) when the material is used as a magnetic field sensor. The relative reflectance of the deposited films was compared to determine the effect of nitrogen flow rates on the expected contrast of the sensors - further calculations on the anticipated contrast is presented in later chapters. Since the thickness of films play a role in the intensity of collected light, the cross section of films was imaged to determine the thickness and shown in Figure 3.7. For the growth parameters used, no considerable increase in film thickness was recorded after 12 hours of growth even with the subsequent introduction of nitrogen gas, thus making it possible to compare samples in groups. The mean thickness of samples in group 1 and group 4 were found to be 11 ± 0.1 μm and 2.5 ± 0.1 μm respectively. Figure 3.8 shows the reflectance spectra of the deposited films. From the spectra obtained in Figure 3.8, we observe that introducing 1 - 10 sccm nitrogen impurities does not have any effect on the reflectance of the material. Outside this regime, the reflectance of the deposited films is seen to decrease with excess nitrogen impurity level in the material (as shown in Figure 3.8c - 3.8d).

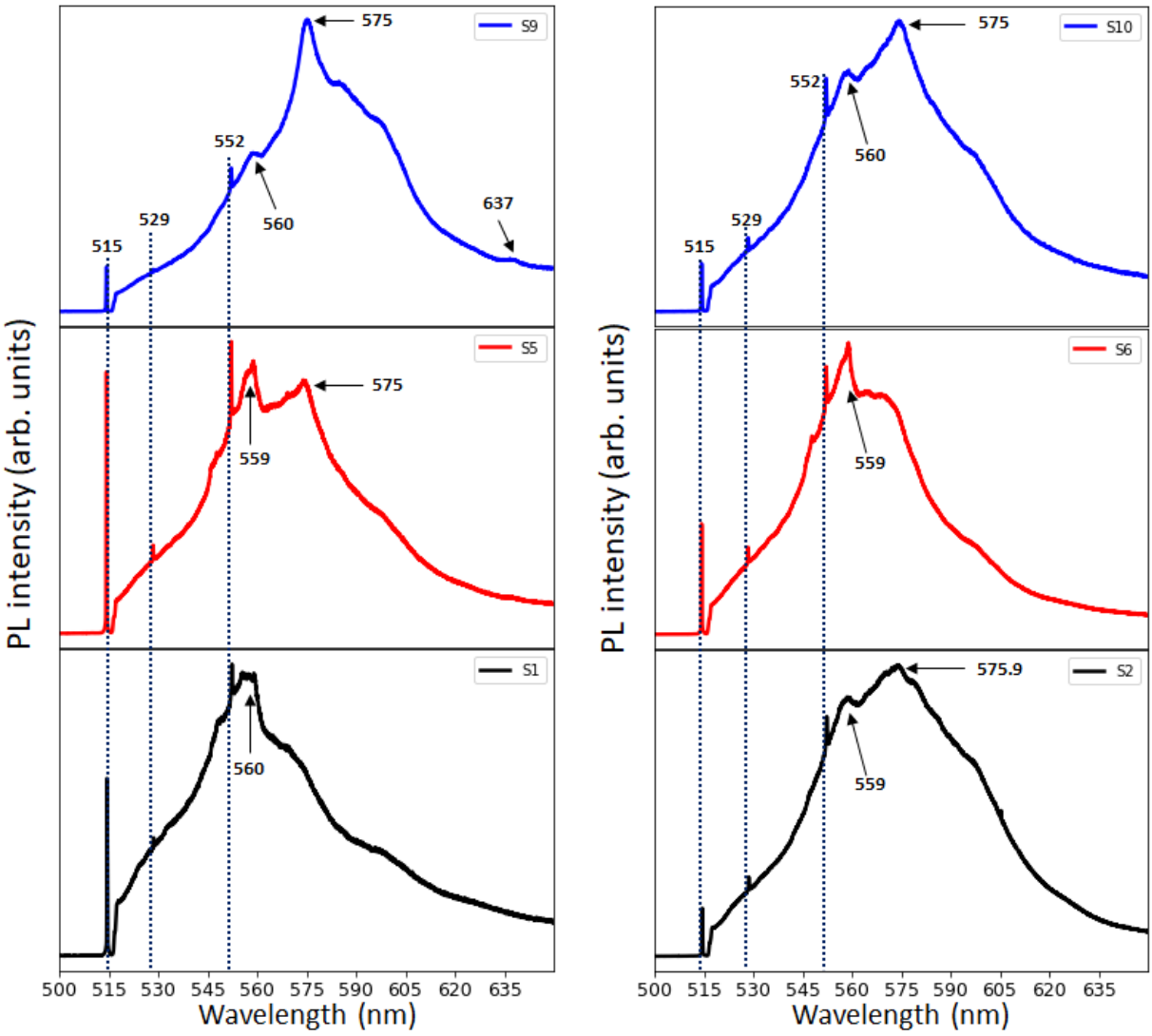

(a) **(b)**

Figure 3.4: Photoluminescence spectra of diamonds films (a) photoluminescence spectra of films in group 1 (b) photoluminescence spectra of films in group 2. The 515 nm lines observed are due to the Ar ion laser; the 529 nm lines are due to the silicon substrate, and the 552 nm peaks are that of diamond. Peaks in the 575 nm to 637 nm line indicates the presence of NV centres. For these groups, most of the deposited films show the presence of neutral charged optical centers (NV^0) but only sample S9 shows the presence of negatively charged optical centers (NV^-) at 637 nm.

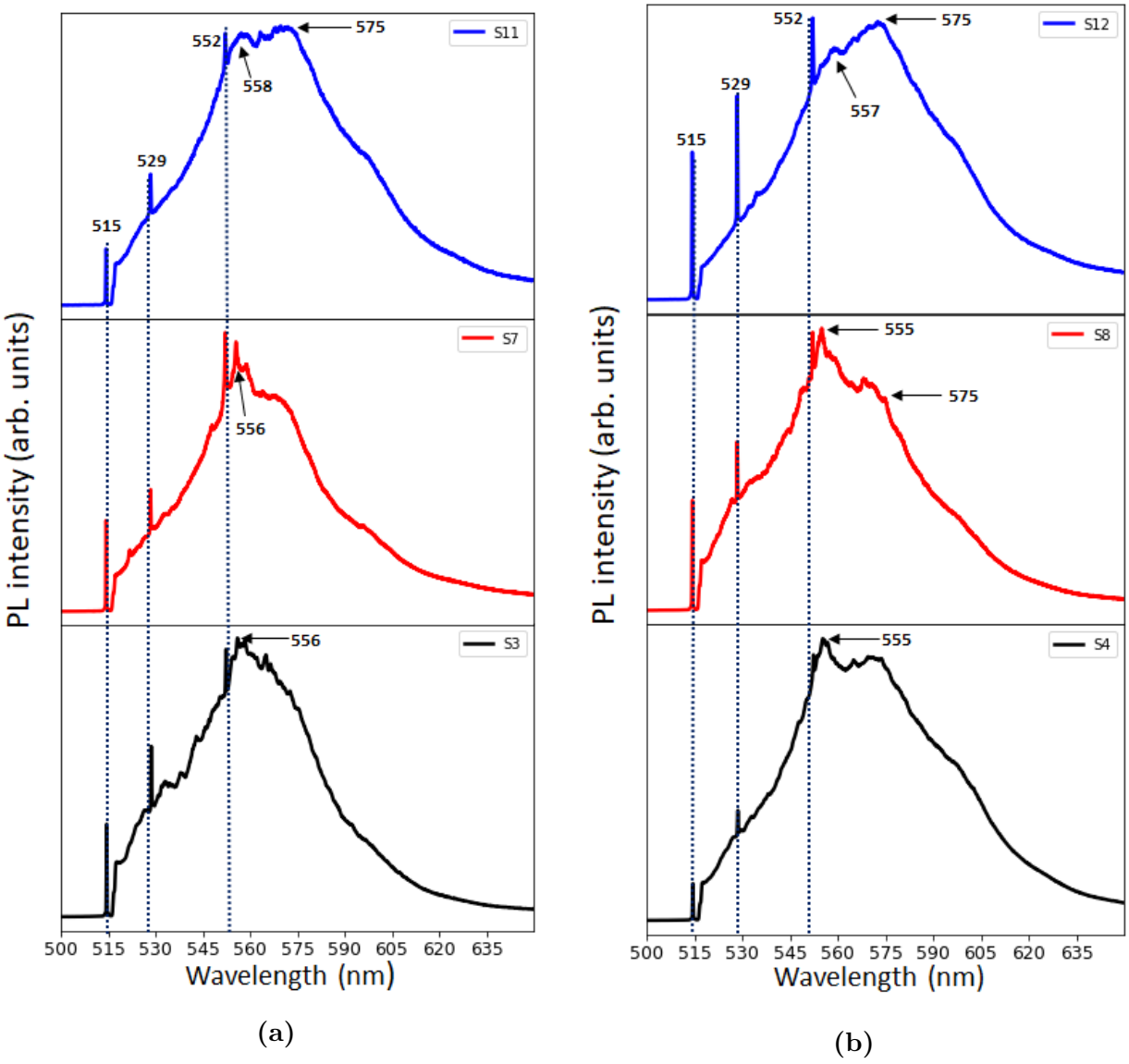

Figure 3.5: Photoluminescence spectra of diamonds films (a) photoluminescence spectra of films in group 3 (b) photoluminescence spectra of films in group 4. It was observed that films doped with medium and a high concentration of nitrogen impurities contained neutral charged optical centers (NV^0). The deposited films in this group do not show the presence of negatively charged (NV^-) centres.

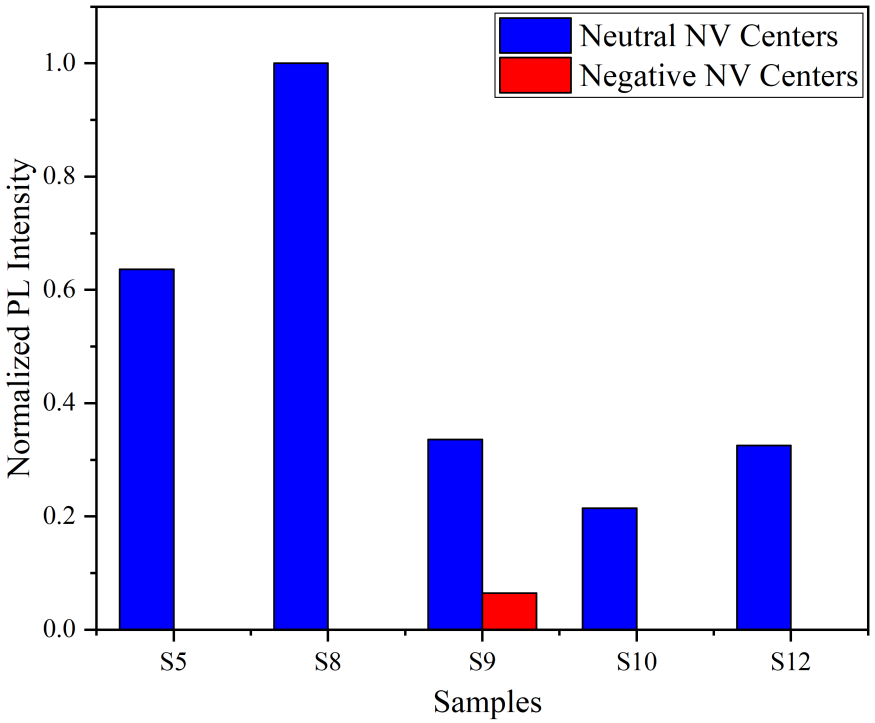

Figure 3.6: Normalized PL intensity of NV^- and NV^0 in diamond samples. Sample S8 in group 4 has the greatest intensity of NV^0 as measured by PL spectroscopy, while S10 in group 2 has the lowest intensity.

3.4 Discussion

3.4.1 Physical Appearance and Raman Spectra of Films

The grey and lustrous grey colour of the deposited diamonds results from the dispersions created by different planes of the grains in the film. Dark grey and black colourations seen in doped diamonds may be due to extended defects from hydrogen atom impurities, dislocation density, and impurities in the lattice [151]. Notably, the incorporation of a high flow rate of nitrogen with a nitrogen-carbon $[N/C]$ ratio greater than 30 in the gas phase mixture leads to black coloured diamonds. Black coloured CVD diamonds are heavily defective with a large quantity of impurity and presence of graphitic grains [152]. The identical spectra of samples with medium nitrogen flow rates (S5 and S6) indicates that a 0.5 sccm difference in flow rate is insignificant to change the microstructure of films grown with similar methane concentration. The observation of the increase in the FWHM of Raman peak of highly doped

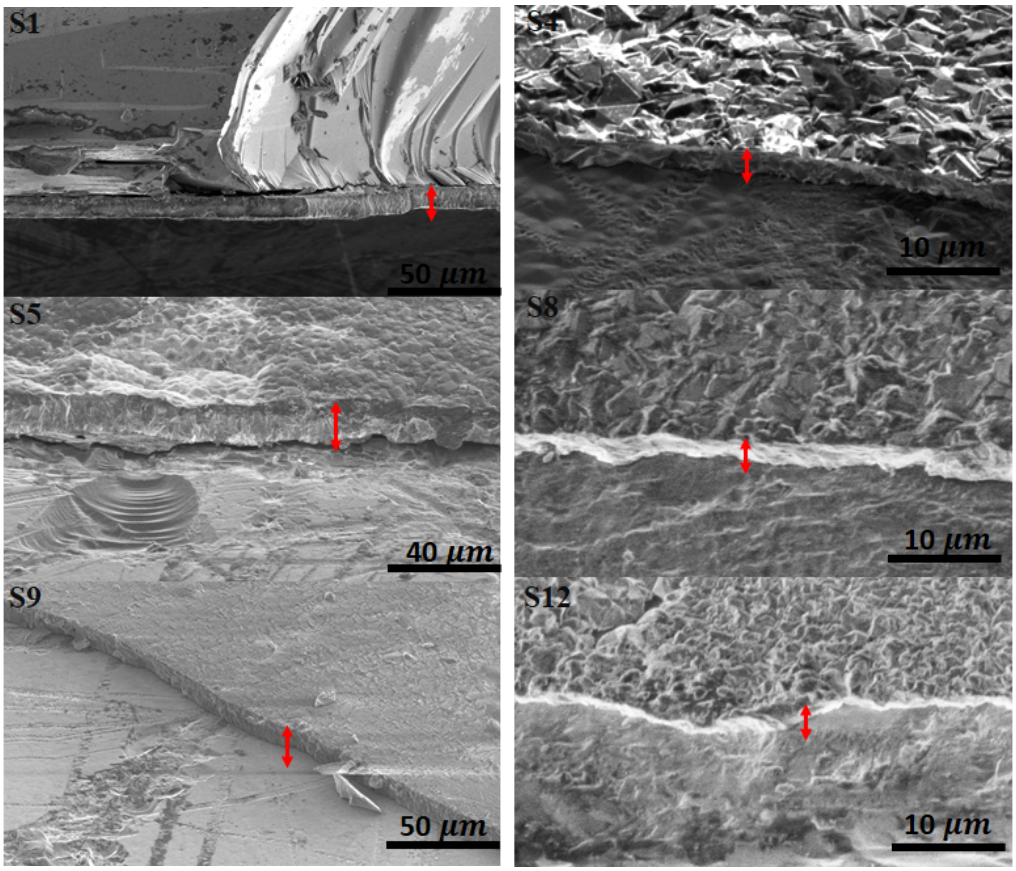

Figure 3.7: Cross-section SEM images of films (a) cross-section SEM images of samples in group 1 (b) cross-section SEM images of samples in group 4.

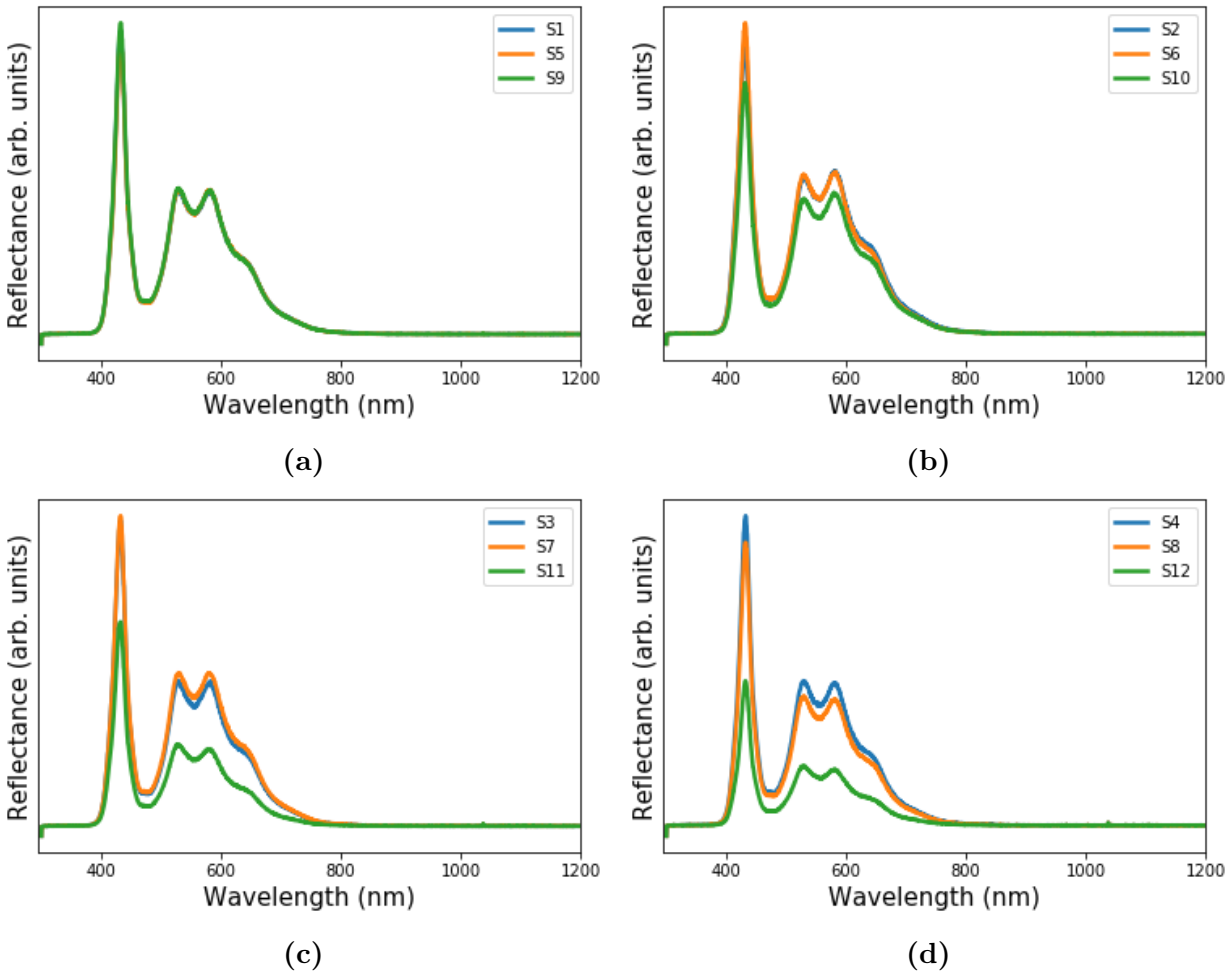

Figure 3.8: Reflectance spectra of samples (a) reflectance spectra of samples in group 1 (b) reflectance spectra of samples in group 2 (c) reflectance spectra of samples in group 3 (d) reflectance spectra of samples in group 4. While there is a remarkable difference in the reflectance spectra of samples in group 3 and 4, deposited films in group 1 and 2 show little to difference in their reflectance spectra.

samples indicates that the addition of a large amount of nitrogen impurity is detrimental to the crystalline quality of CVD diamonds. Using the diamond peak at 1332 cm^{-1} as a standard, the shift in the Raman wavenumber and the ratio of the intensity of diamond and amorphous carbon peak (I_{Da}/I_G) may be obtained and is shown in Figure 3.8. Negative Raman line shifts are due to compressive stresses in the films, while positive Raman line shifts are due to intrinsic stresses which are tensile in nature [145]. A high quantity of nitrogen impurity can introduce stress in the material [152]. This is confirmed by a shift in the diamond peak from $\sim$ 1332 cm^{-1} to 1334 cm^{-1} for highly doped samples (sample S12). For sensing applications, black coloured diamonds are undesirable due to the high concentration of amorphous carbon which quenches photoluminescence from the NV^- centres. Potential candidates for this sensing application are experimental samples showing either grey or lustrous grey colourations with the presence of NV^- center.

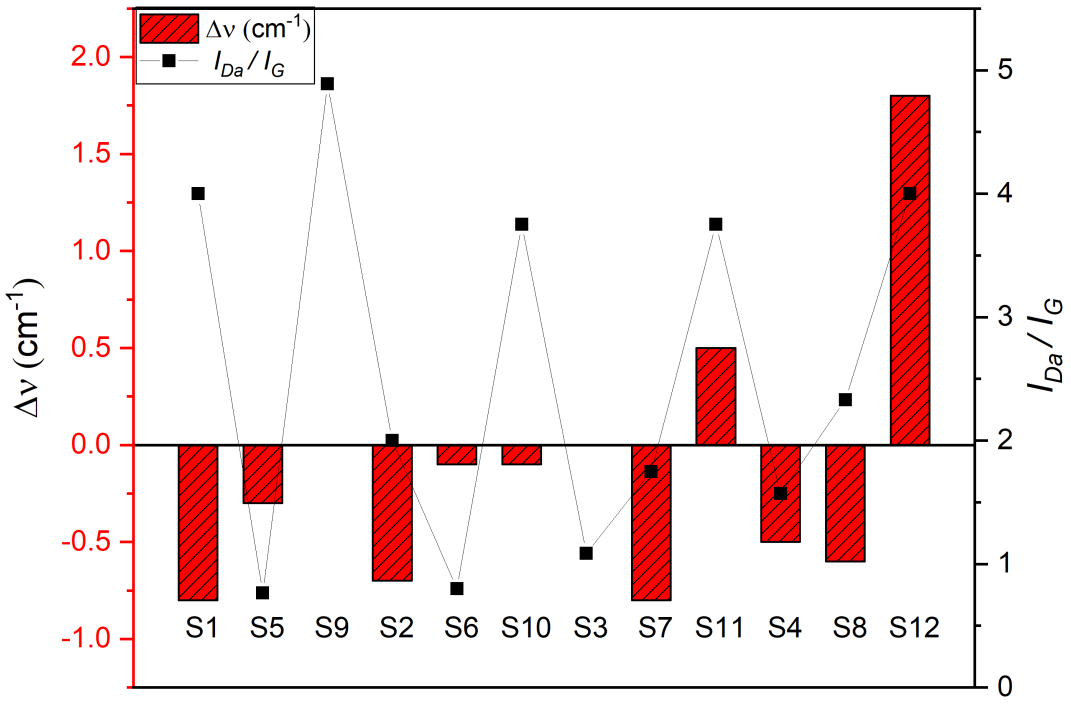

Figure 3.9: Q-graph representing shifts in the Raman lines and the ratio of the intensity of diamond peak to amorphous carbon peaks. Positive Raman line shift in sample S12 and S11 results from intrinsic stresses in the films.

3.4.2 Morphology of Films

From the SEM micrograph results, insights into the formation of nitrogen related optical centres from a surface morphology perspective can be obtained. First, in small-sized nano-grain diamonds typical of diamonds doped with medium flow rates (1.5 - 2 sccm), it is believed nitrogen is incorporated preferentially at grain boundaries [153] rather than in the grains. This is evident by results obtained from tight-binding molecular dynamics simulations in Ref. [154]. It is also possible that vacancies are not easily incorporated in small-sized grain polycrystalline diamond with fine and continuous surface textures, therefore, bringing doped nitrogen to grain boundaries or even forming other complex configurations that do not include nitrogen vacancies. This may explain why there are no nitrogen related optical centres in sample S6 in group 2. Samples with little or no vacancies like sample S6 of group 2 may require further processing.

Vacancies can be created using a high energy electron irradiation beam [155]. Since nitrogen is present in grain boundaries or in other configurations, an additional annealing procedure will help migrate vacancies to form nitrogen-vacancies in the films. Apparently, nitrogen related optical centers can be formed via excessive doping as shown by Ohno et al. [155] but at the expense of losing the crystalline quality of the diamond films. In addition, several authors including Schirhagl et al. [109] have reported a depreciation in the spin coherence properties of excessively doped films. Nevertheless, it is important to emphasize that sample S9 in group 1 maintained its crystalline structure despite the high nitrogen flow rate (10 sccm). This again points to the fact that sample S9 may be a suitable material for sensing applications.

3.4.3 Photoluminescence (PL) and Reflectance Spectra of Films

Several publications [89, 148, 156, 157] have shown that when no extra effort is made to exclude residual nitrogen gas in the chamber before deposition, the PL spectra obtained from CVD diamonds can show the presence of neutral or negative nitrogen-vacancy defects. The

NV defect translates into PL peaks at 575 and 637 nm, where the 575 and 637 nm peaks correspond to a nitrogen atom bonded to the nearest vacancy and to the vacancy trapped at a substitutional nitrogen atom respectively. The observed nitrogen related peaks are broad. The broadness might be indicative of the presence of other defects in the CVD grown diamonds [158]. In group 2, sample S2 shows a peak at 575.9 nm different from the 575 nm line. This peak is also believed to be associated with nitrogen features in the sample [159]. In an earlier work, Gu et al. [159] have shown that the 575.9 nm peak is common in milky type IaB diamonds. The formation of this nitrogen related peak in sample S2 is due to the baseline pressure we operated at before deposition [156].

The relative intensity of NV centres shown in Figure 3.6 reveals the formation of predominantly neutral NV centres on the surface of some of the deposited films. This condition as explained by Santori et al. [160] is due to the formation of electronic acceptor layers at the diamond surface. At the surface region, nitrogen donors are ionized thereby making it impossible to donate an electron to the NV centre. A potential acceptor candidate is an amorphous carbon (sp^2) element deposited alongside diamond during the CVD growth process[161]. In addition, because shallow optical centres are formed at the surface, NV centers at the surface may not be stable [109, 162]. Samples showing the formation of neutral NV centers need further processing to covert the neutral NVs to negatively charged NVs. Surface oxygenation at about 465^oC may be a useful method to induce charge state conversion for the grown diamond films [109, 163, 158].

To understand the influence of microwave power density and pressure on the formation of negatively charged NVs, an additional experiment was carried out at 50 Torr working pressure and 900 W microwave power, while keeping the rest of the parameters for sample S10 in group 2 constant (200 sccm of hydrogen, 1 sccm of methane, 20 sccm of nitrogen). The PL spectra obtained from the experiment is shown in Figure 3.10. Contrary to the formation of neutral NV center in sample S10, the spectra of New S10 clearly shows the formation of both neutral and negatively charged NVs. This implies that higher microwave power density and

pressure may increase the etching of unwanted carbon phases thereby making it possible to observe the photoluminescence of negative NV centers. It is also possible that at low pressure, nucleation is enhanced and as a result causes electron sinks at grain boundaries [164]. This is another possible explanation for the dominance of neutral NVs in samples grown at 30 Torr pressure.

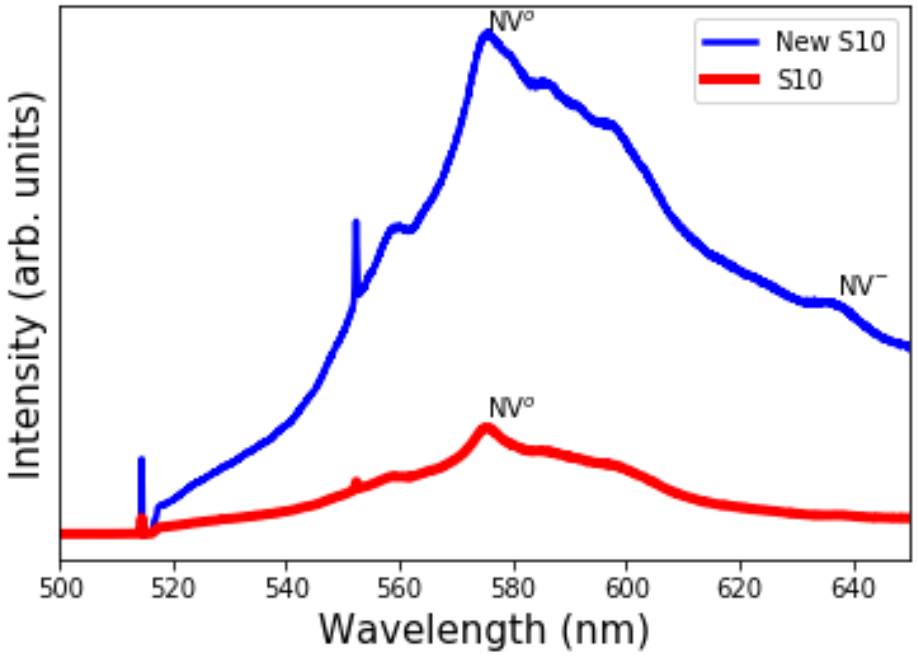

Figure 3.10: Comparison between sample New S10 and sample S10. Sample New S10 was deposited with 50 Torr pressure, 900 W microwave power while keeping other growth parameters for S10 constant (800 W microwave power, 30 Torr pressure, 200 sccm of hydrogen, 1 sccm of methane, and 20 sccm of nitrogen). Formation of neutral and negative NV is observed in sample New S10.

From the PL spectra obtained in Figure 3.5a and 3.5b, it can be concluded that the introduction of high nitrogen (10 - 40 sccm) concentration in the CVD process will always lead to a formation of neutral NV centers in diamond films. Also, increasing nitrogen concentration from 10 - 40 sccm results in broader 575 nm peaks. The introduction of a low concentration of nitrogen impurities might not yield any surface optical centers. This result is not in agreement with the work of Watanabe et al. [149] where they have have reported the formation of negatively charged NV centres while using extremely low nitrogen flow rates.

The possible reasons for this disparity might be the difference in growth parameters or the substrate used. Watanabe et al. [149] have shown the formation of negative NV centers homoepitaxially. Demonstrating the presence of NV centers on foreign substrates like silicon is a way to engineer cheap optical centers needed for arrayed sensing applications.

The total reflectance of the film modelled by Fresnel's equation at normal incidence as described in Ref. [165] depends on several factors. Surface texture, and density variations due to defects in the materials among other factors appear to account for the variation of reflectance. The difference in reflectance observed in the deposited films is closely connected with crystal imperfections [166]. Highly doped films with stacking faults, dislocations, and impurities inclusion will show a significant decrease in surface reflectance compared to undoped or minimally doped films. Zuiker et al. [167] showed that the reflectance of thin film diamonds decreases with an increase in CH_4 content. Here, it was observed that the reflectance of the films grown decreases with an increase in nitrogen content. Poor optically detected magnetic resonance (ODMR) contrast are obtained from films with high nitrogen concentration. Films with high concentration of nitrogen impurity (20 - 40 sccm) are unsuitable for sensing applications due to their poor reflectance properties. Although, sample S9 in group 1 has also been doped with a high nitrogen flow rate (10 sccm), no changes in the intensity of reflectance spectra was observed when compared to its counterparts in group 1, for this reason, sample S9 is suitable for sensing applications.

3.5 Conclusion

The influence of surface-introduced nitrogen impurities on the morphology and optical properties of polycrystalline diamonds deposited at low pressure has been systematically investigated. The studies have been carried out in three flow regimes: no nitrogen addition (0 sccm), medium nitrogen addition (1 - 4 sccm), and high nitrogen addition (10 - 40 sccm). Polycrystalline diamond changes colour depending on the amount of nitrogen impurities added. PCDs deposited without the addition of nitrogen impurities appeared grey in colour, while those deposited in the presence of nitrogen impurities show a range of colours depending

on the concentration of nitrogen in the sample. The grey and lustrous grey colour of the deposited diamonds results from dispersions created by different planes of the grains in the film. Dark grey and black colourations seen in doped diamonds may be due to extended defects and impurities in the lattice.

High nitrogen flow rates in polycrystalline diamonds led to an increase in FWHM of diamond peaks. This feature indicates a depreciation in the crystalline quality of deposited diamonds as revealed by SEM micrographs. The increase in the FWHM of the Raman peak of highly doped samples also indicates that the addition of a large amount of nitrogen impurity is detrimental to the crystalline quality of CVD diamonds. A high quantity of nitrogen impurity can also introduce stress in the material [152]. Signals from nitrogen related optical centres (predominantly neutral NV centres) were mostly detected in the PL spectra of diamond films doped with medium and high nitrogen flow rates. Samples in group 1 (S5 and S6), a sample in group 2 (S10), and samples in group 4 (S8 and S12) show the presence of NV^0. Only sample S9 in group 1 shows peak indicating the presence of NV^-. We observe the formation of predominantly neutral NV centres on the surface of some of the deposited films. This condition is due to the formation of electronic acceptor layers at the diamond surface. A potential acceptor candidate is an amorphous carbon (sp^2) element deposited alongside diamond during the CVD growth process[161]. In addition, because shallow optical centres are formed at the surface, NV centers at the surface may not be stable [109, 162]. Samples showing the formation of neutral NV centers need further processing to covert the neutral NVs to negatively charged NVs. Surface oxygenation at about 465^oC may be a useful method to induce charge state conversion for the grown diamond films.

It was established that a high flow rate of nitrogen doping ($\geqslant$ 20 sccm) will lead to a decrease in the reflectance of polycrystalline diamond. Highly doped films with stacking faults, dislocations, and impurities inclusion will show a significant decrease in surface reflectance compared to undoped or minimally doped films. Also, poor ODMR contrast will be obtained from films with high nitrogen concentration. Thus, due to the poor reflectance properties of

highly doped films (20 - 40 sccm), they might be unsuitable for sensing applications. However, one of the samples (S9 in group 1) doped with high flow rate of nitrogen exhibited a reasonable FWHM, and presence of both neutral and negatively charged optical centers. In addition, the sample S9 in group 1 exhibited a good reflectance property as shown from the reflectance spectra. With these combination of properties, sample S9 in group 1 may be a suitable material for sensing applications. The results obtained are important in identifying optimal parameters for the growth of polycrystalline diamonds suitable for sensing applications. Also, the set of experimental parameters described in this work may be useful as a benchmark for the growth of polycrystalline diamonds with NV centres at low pressure.

Now that an optimal processing parameter set for the formation of useful NV centres in PCDs deposited at low pressure has been identified, it is imperative to understand the theory behind the formation of NV^- centres in PCDs, most especially those fabricated at low pressure - this is the topic of investigation in chapter 4.

Chapter 4

The effect of step-wise surface nitrogen doping on the formation of NV^- centres in PCDs

"No pressure, no diamond"

– Thomas Carlyle

This chapter is based on the manuscript:

Ejalonibu, H., Sarty, G., & Bradley, M. (2020). The effect of step-wise surface nitrogen doping in MPECVD grown polycrystalline diamonds. *Materials Science and Engineering: B*, 258, 114559.

4.1 Introduction

The study of the incorporation of nitrogen impurities into PCDs synthesized using the CVD technique has been an active area of research in recent years. Much literature including the author's in chapter 3 highlights the effect of nitrogen impurities on the intrinsic properties of PCDs. In addition, work by Zaitsev et al. in 2018 [168] investigated the optical properties of nitrogen-doped CVD diamonds treated with electron irradiation, followed by annealing at temperatures between 860 - 1900^{o}C. The optical properties of the CVD diamonds were studied using fluorescence imaging, optical absorption, and photoluminescence spectroscopy. It was reported that nitrogen impurities improve the optical properties of CVD diamonds by producing several optical centres (e.g. nitrogen-vacancy centres) showing absorption lines

throughout the infrared and visible spectral ranges. Also, results obtained from an earlier work by Bhattacharyya et al. [169] show that the electrical conductivity of nitrogen-doped films increases by several orders of magnitude with increasing nitrogen content. Primarily, nitrogen acts as an electron donor that decreases the bandgap of diamond [170] and the increase in the electrical conductivity of nitrogen-doped diamond is attributed to the formation of a lone pair of sp^2-bonded carbon that provides a conductive path for electrons. Thus far, consolidating evidence exists supporting the hypothesis that the introduction of nitrogen impurities into PCDs alters their intrinsic properties.

In chapter 3, it was highlighted that during CVD diamond growth, impurities introduced can be trapped in defects resulting in the formation of optical centres, for example the NV centres. Optical centres engineered via nitrogen incorporation in diamonds are useful for a number of applications. For instance, NV optical centres find applications in room temperature magnetometry, quantum information, and thermometry [139, 50, 171, 172, 173]. The magnetometry applications of diamonds rely on the incorporation of NV^- optical centres at close proximity to the diamond surface; this is achieved by surface nitrogen doping. The effect of surface nitrogen flow rates on the formation of useful NV centres has been widely investigated in SCDs grown at high pressure, high temperature (HPHT) conditions [174, 175]. To date, however, there is a limited understanding of the formation of NV^- centres in polycrystalline diamonds deposited at low pressure. Previous studies did not establish the effect of different nitrogen doping levels on the surface features of PCDs (deposited at low pressure < 40 Torr) and how it contributes to the localization of either NV^- optical centres or its NV^0 counterpart. In particular, previous studies did not provide any conclusive statement on the effect of step-wise nitrogen doping level on the localization of useful NV centres in PCDs.

This chapter is therefore aimed at understanding the effect of a step-wise surface nitrogen doping process on the formation of NV^- centres in PCDs. Here, an exhaustive study of the contributions of nitrogen flow rate on the surface morphology, grain orientations, and the formation of sp^2 bonded carbon found at the grain/grain boundaries is reported. To under-

stand the correlation between ingrained surface properties of nitrogen-doped PCDs and the formation of NV^- centres in PCDs, the changes in the surface properties of the films under a step-wise surface nitrogen-doping have been systematically investigated using different techniques. The surface of the deposited films was characterized using photoluminescence spectroscopy (PL), scanning electron microscopy (SEM), X-ray photoelectron spectroscopy (XPS), and atomic force microscopy (AFM). Grazing incident X-ray diffraction (GIXRD) was used to investigate the crystallographic changes resulting from surface nitrogen doping. Finally, Raman spectroscopy studies were carried out to investigate the microstructural changes in the films and to characterize sp^2 bonds in the diamond grains. Based on these experimental observations, a mechanism for the changes in the surface morphology of films grown under step-wise nitrogen doping is proposed. Consequently, this model was used to explain the possible dominance of NV^0 centres in PCDs in the low pressure growth regime. The results obtained from the study in this chapter contributes to a better understanding of the process for the formation of NV^- centres in PCDs deposited at low pressure.

4.2 Experimental

4.2.1 Materials

Diamond films were deposited on a p-type boron doped silicon (100) substrate of thickness 525 μm and 3×3 mm size obtained from Silicon Materials Inc., NV, USA. Mechanical surface scratching of the substrate was performed using diamond slurry with a grain size of about 1 μm (Markv Laboratories, CT, USA). Finally, ultrahigh purity H_2 (5.0 Grade), CH_4 (3.7 Grade), and N_2 (5.0 Grade) were obtained from Praxair Canada Inc., SK, Canada.

4.2.2 Synthesis of Polycrystalline Diamond Films

The growth process used in this experiment is illustrated in Figure 4.1. Prior to growth, the silicon substrate was seeded using a mixture of diamond slurry and ethanol for 30 min in stage A. Next, the substrates were cleaned in an ultrasonic bath for another 30 min. The seeded substrates were later introduced into a 2.45 GHz MPCVD reactor (Plasmonique Inc.,

QB, Canada) at a baseline pressure of $\sim 2.0 \times 10^{-5}$ Torr in stage B. Diamond films were deposited on silicon substrates with 800 W microwave power and 30 Torr pressure. Table 4.1 shows the process parameters for the growth process.

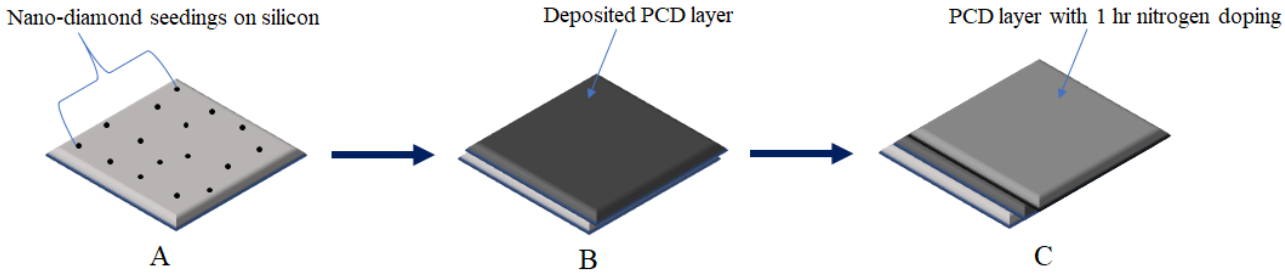

Figure 4.1: Schematics showing the experimental processes involved in the synthesis of polycrystalline diamond films; from substrate preparation to diamond deposition. In stage A, silicon substrates were prepared for growth in a diamond and ethanol slurry. Stage B involved diamond deposition while in stage C surface nitrogen doping was carried out.

All films were deposited for 18 hrs. For samples containing surface nitrogen impurities, the nitrogen gas was introduced 1 hr from the end of the experiment in stage C with varying nitrogen flow rates introduced in a step-wise manner (see Figure 4.2). The substrate temperature was kept at about 750^0C during growth. Surface nitrogen was added in three different regimes: 2 - 4 sccm, 6 sccm, and 8 - 10 sccm which were referred to as the low, medium, and high nitrogen regimes respectively.

Table 4.1: Process parameters for the deposition of PCD films on silicon substrate at 30 Torr pressure, 800 W microwave power, surface nitrogen flow rate in standard cubic centimeter per minute (sccm), and a deposition temperature of about 750 ^{0}C.

Samples	H_2/CH_4 flow (sccm)	N_2 flow (sccm)	Growth time (hrs)	Doping time (hrs)
P1	100 / 1	0	18	0
P2	100 / 1	2	17	1
P3	100 / 1	4	17	1
P4	100 / 1	6	17	1
P5	100 / 1	8	17	1
P6	100 / 1	10	17	1

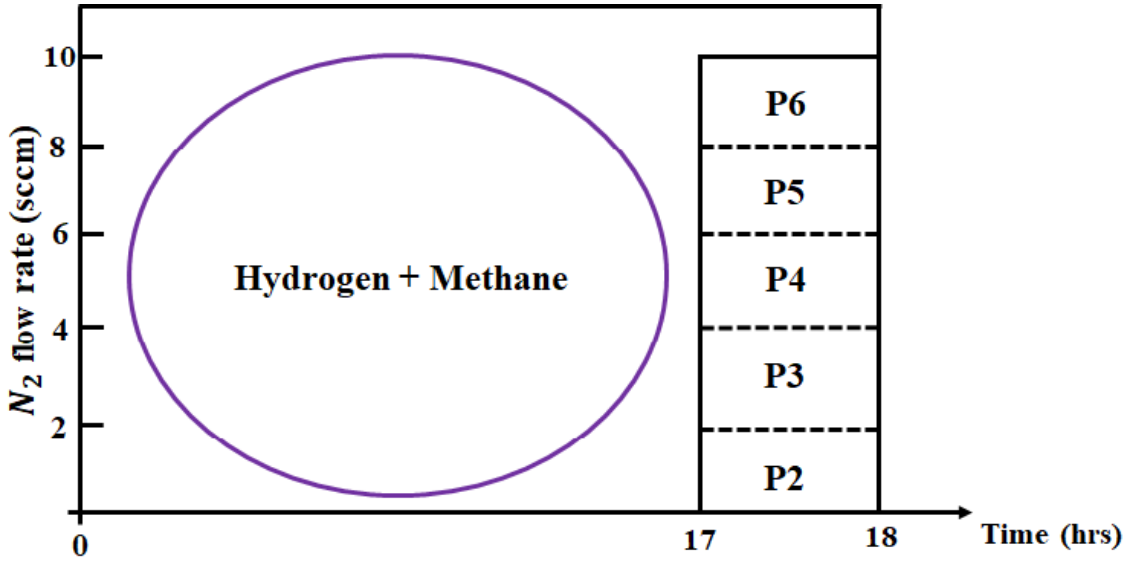

Figure 4.2: Schematics representing the flow rate conditions in a step-wise manner. For the first 17 hrs of growth, only hydrogen and methane were the precursor gas used for deposition. After 17 hrs of diamond deposition, deliberate nitrogen doping was carried out for each sample in a step-wise order.

4.2.3 Diamond Film Characterization

Photoluminescence and Raman Spectrocopy

To probe surface properties within a 1 μm depth from the diamond surface, it was important that the right combination of objective lens and laser wavelength was chosen since the total scattered light intensity (A_S) integrated from the surface of the diamond to depth (d) is given by the following Equation 4.1:

$$A_S = A_0 \frac{1.22 \cdot \lambda}{N_A} \int_0^d e^{-2\alpha x} dx = \frac{0.61 \cdot A_0 \cdot \lambda}{N_A \cdot \alpha} (1 - e^{-2\alpha d}) \tag{4.1}$$

where A_0, λ, N_A , and α are the intensity of the incident light, the laser wavelength, numerical aperture of the microscope objective, and the photoabsorption coefficient of the surface respectively [176, 177]. For this experiment, a 514.5 nm Argon ion laser was used for excitation and a 50× objective microscope with a numerical aperture (N_A) 0.75 was used. Under these conditions, the laser penetrates approximately 1 μm from the diamond surface. To discriminate between neutral and negatively charged NV centres at the surface, photoluminescence (PL) spectroscopy was carried out. The surface microstructure of the deposited films was investigated using a confocal Raman spectroscope (Renishaw InVia, ON, Canada) with embedded PL spectrum collection functionality. The equipment is capable of collecting a PL spectrum from about 100 nm to 650 nm wavelength ranges. The Raman and PL signals were collected by focusing the Argon ion laser beam on a 20 μm diameter spot at 10 different spots and averaging the results. All Raman spectra were fitted with a sum of Lorentz functions using the WiRE Raman Renishaw software to identify peaks of interest. Note that the PL emission intensity of optical centres is laser power and exposure time dependent. For each spectra acquisition, a laser power of 2.74 mW with an exposure time of 10 s was used. Contrary to our previous study in chapter 3, the laser power was reduced to avoid laser heating of the diamond surface which induces sp^2 bonded carbon.

X-ray Diffraction and X-ray Photoelectron Spectroscopy

The orientation and surface crystallographic texture of the PCD films were characterized using X-ray diffraction with CuK_{α} radiation, wavelength 1.54056 (Rigaku Ultima IV, TX, USA) at a grazing incidence angle of 5°. The X-ray diffraction data were collected at 40 kV and 44 mA. Since the characterized PCDs were not free-standing films, the silicon substrate was used as a reference. XPS measurements were taken using a Kratos Axis Supra (Kratos Analytical, MAN, U.K.) equipped with a 500 mm Rowland circle monochromated Al Kα (1486.6 eV) X-ray source to provide better energy resolution.

Scanning Electron Microscopy and Atomic Force Microscopy

The surface morphology of the films was characterized using a Field Emission Scanning Electron Microscope (FE-SEM, Hitachi SU8000, Tokyo, Japan). Electron micrographs were taken using an acceleration voltage of 3 kV and ×10 k magnification. To quantify the surface roughness of the samples and to probe nano-sized grain boundaries, the morphology of the samples were further measured in air by atomic force microscopy (PicoSPM AFM, Keysight Technologies 4500 AFM, ON, Canada) in tapping mode. The AFM instrument was equipped with a single crystal silicon cantilever (Aspire CT170, AZ, USA) with a resonance frequency 170 kHz and a spring constant of 50 N/m. Image J software (NIH and LOCI, University of Wisconsin, USA) was used to process the SEM micrographs while Gwyddion software (Czech Metrology Institute, CZ) was used to process the AFM images.

4.3 Results

4.3.1 Nitrogen Content and PL Study

To probe elemental compositions in the films grown and to understand the chemical state of the main elements present on the surface of the PCDs, XPS were collected for samples P1 - P6 after etching the surface with Ar ions. A wide range spectrum (200 - 1000 eV)

for samples P1 - P6 is presented in Figure 4.3. The elemental composition of the deposited films presented in Table 4.2 reveals that the atomic concentration of nitrogen in PCD films increases with an increase in doping level. XPS survey spectra indicated the presence of carbon, nitrogen, and oxygen with a trace amount of fluorine in sample P4 and P5 only. The peak attributed to this fluorine content is found around 686 eV which corresponds to the peak for silicon hexafluoride $(SiF_6)^{2-}$ ions contaminant [178].

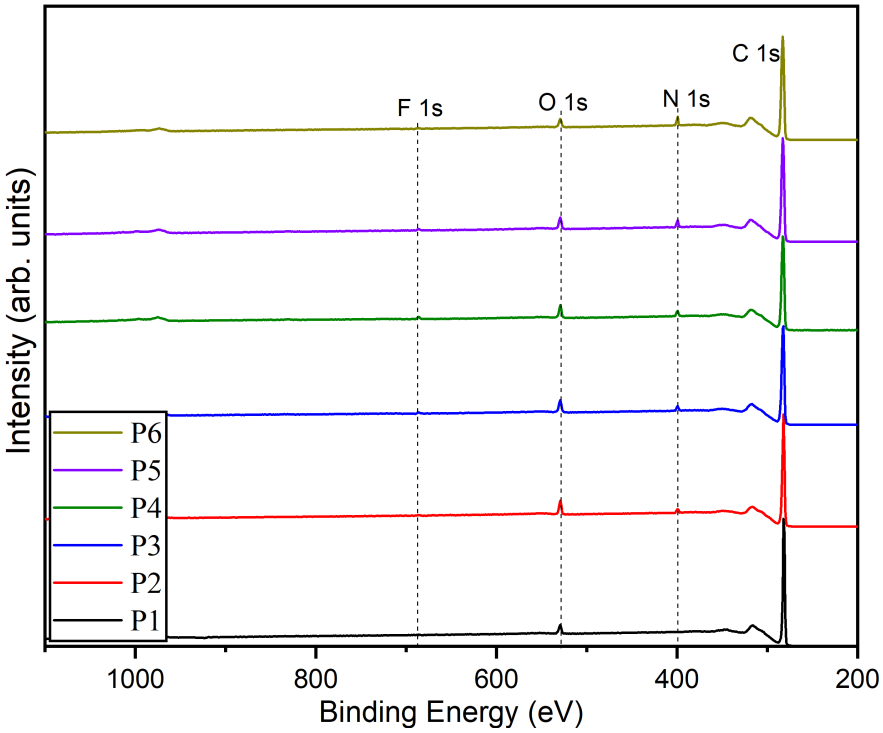

Figure 4.3: Wide survey XPS scan of the deposited films. No traces of atomic nitrogen were found in sample P1 while the presence of atomic nitrogen was found in samples P2 - P6.

C 1s peaks were observed at 283 eV, while N 1s peaks were observed at 399 eV. Since nitrogen doping was carried out for an hour, it was expected that the level of atomic nitrogen present in the actual PCD films did not exceed 0.4%. Processed data revealed the presence of large amount of oxygen O 1s peak, from its spectral peak, on PCD surface (> 2.0 at. %) at around 529 eV, however, the analysis of O 1s, is not of interest in this study. The principal peak of the N 1s signal at ~ 400 eV corresponds to chemical bonds of type N-sp^3-C [179]. This peak corresponds to interior elemental nitrogen present in the diamond matrix, including NN dimers, substitutional nitrogen, and more complex nitrogen clusters

[180]. Deconvolution (fitting the peak with a Voigt function on Origin software, followed by a subtraction of background signals) of the C 1s peak revealed peaks centered at 283 eV corresponding to the C-C bonds in the diamond matrix and another located at 286.9 eV corresponding to the C-N bonds. Since we confirmed the bonding type C-N in these samples it was necessary to obtain PL spectra of samples to ascertain the presence of NV centres.

Figure 4.4 shows the PL spectra of the deposited films where the spectra of only nitrogen doped films have been co-plotted. The broad peaks due to nitrogen luminescence in the diamond material were observed at 575 nm and 637 nm. The NV^0 centres at 575 nm is observed in sample P2 - P6, while the 637 nm peak which may have originated from the NV^- centres was only observed in sample P6. The broad nature of the peaks at 575 nm and 637 nm might have resulted from the presence of other defects in the material [123]. For magnetometry applications, the FWHM of the peaks are irrelevant, because emissions in the red spectra range are only desired (600 - 800 nm). Furthermore, note that the MPCVD samples were deposited on silicon substrates and it is possible that the phonon sides bands of the NV^0 centers, for instance in samples P2 and P4, are suppressed due to the substrate used [181]. From the PL spectra of the films, it is evident that all nitrogen doped samples show the presence of NV^0 centres. On the other hand, only sample P6 doped with 10 sccm of nitrogen indicates the presence of NV^- centres. One of the reasons for the disappearance of NV^- centres at other nitrogen concentrations but 10 sccm may be intimately connected with amorphous carbon (a-C) phases in the grains and grain boundaries. For this reason, a micro-Raman spectroscopy analysis was carried out.

4.3.2 Raman Spectroscopy Analysis

Raman spectroscopy is a useful tool for characterizing structural transformations occurring in carbon materials because it can distinguish between sp^3 and sp^2 bonded orbitals in the deposited films [182, 183]. Figure 4.5a shows the Raman spectra of the deposited films with varying nitrogen concentrations. All films exhibited sharp peaks around 1332 cm^{-1} indicating the formation of a diamond phase and a graphite like carbon (G-band) phase around 1500

Table 4.2: The summary of elemental composition of the MPECVD film. FWHM of deposited peaks widens as the atomic nitrogen concentration increases.

Samples	Elemental Compositions	Atomic Concentration (%)	FWHM	[N/C]
P1	C 1s	97.16	2.41	-
	O 1s	2.84	3.15	
	N 1s	-	-	
P2	C 1s	95.60	2.75	0.0020
	O 1s	4.24	2.90	
	N 1s	0.16	2.93	
P3	C 1s	95.8	3.25	0.0020
	O 1s	4.02	3.17	
	N 1s	0.17	2.48	
P4	C 1s	95.6	3.43	0.0022
	O 1s	3.82	2.95	
	N 1s	0.22	2.82	
	F 1s	0.36	3.08	
P5	C 1s	96.30	3.37	0.0026
	O 1s	3.42	2.29	
	N 1s	0.26	3.18	
	F 1s	0.24	2.74	
P6	C 1s	97.16	3.53	0.0025
	O 1s	2.59	3.29	
	N 1s	0.25	2.12	

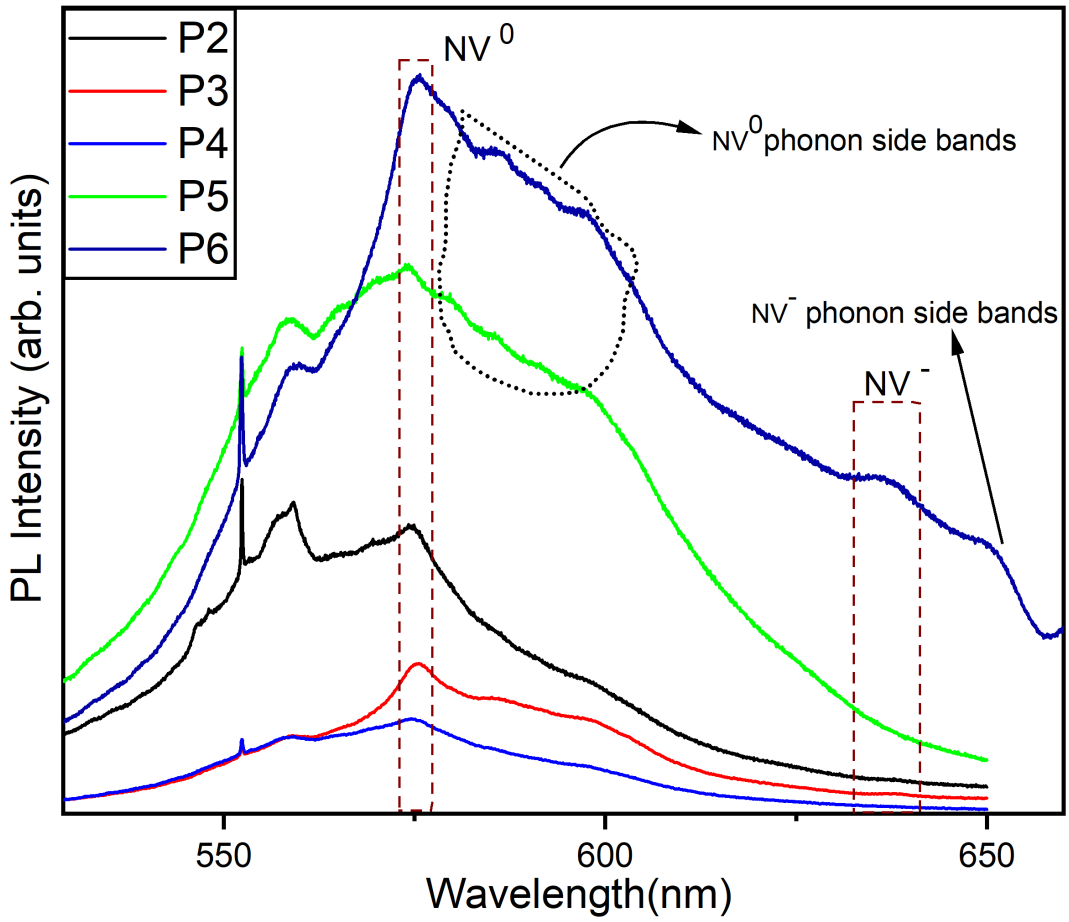

Figure 4.4: Room temperature PL emission spectra of nitrogen doped films showing the presence of NV^0 centres in sample P2 - P6 and their phonon side bands. Only sample P6 indicates the presence of NV^- centres

- 1600 cm^{-1} [178]. Raman peaks occurring around 2000 - 2063 cm^{-1} were attributed to the formation of NV^0 centres. The G-band arises from the presence of sp^2-C chains in the grain boundaries and are more pronounced in nanocrystalline diamond (NCDs) samples [184]. In addition, a 1140 cm^{-1} peak was observed in sample P2. For samples P3, P4, and P5, the presence of a different peak occurring at 1190 cm^{-1} was identified (a magnified spectra is shown in Figure 4.5b). On the contrary, such peaks were not observed in sample P6. To nail down the occurrence of the 1140 cm^{-1} and 1190 cm^{-1} band, further quantitative measurement of the contributions of sp^2/a-C bonded carbon was deduced from the quality factor ($Q_{514.5\ nm}$) of the deposited films at the 514.5 nm excitation wavelength using the formula proposed by Bak et al. [185]:

$$Q_{514.5\ nm} = \frac{I_D}{I_D + \frac{\sum I_{a\text{-}C}}{233}} \times 100\% \tag{4.2}$$

where $Q_{514.5\ nm}$ is the quality factor of the deposited films, I_D is the intensity of the diamond peak, and $\sum I_{a-C}$ is the sum of the intensities of sp^2/a-C related peaks. The low photon energy of Raman lasers results in a large scattering cross-section for the sp^2 orbitals [186], hence the reason for the inclusion of the scattering factor "233" in Equation 4.2 for amorphous carbon.

An analysis of the FWHM of the G-band gives a measure of the structural disorder (distortion of bond length and angle) of the sp^2-bonded carbons in the grains [187, 143]. The Raman spectra of films was fitted with a sum of Lorentz functions; results of curve fittings is shown in Figure 4.6 with FWHM of the G-peak and NV^0 centres being the parameter of interest. Table 4.3 presents the computed quality factor of the diamond films, the corresponding FWHM of their G-bands, and the normalized NV^0 centre intensity of the deposited films obtained from the curve fittings. From Table 4.3, it can be inferred that the degree of structural disorder of the sp^2-bonded carbon in the grains and grain boundaries decreases with an increase in surface nitrogen concentration.

It is also clear that the quality factor $Q_{514.5\ nm}$ of the diamond films increases with an increase in surface nitrogen concentration at least for the growth parameters we have reported here. Further, the normalized NV^0 centre intensity obtained from the Raman spectra shows the highest peak intensity at 8 sccm surface nitrogen concentration (sample P5) and the lowest

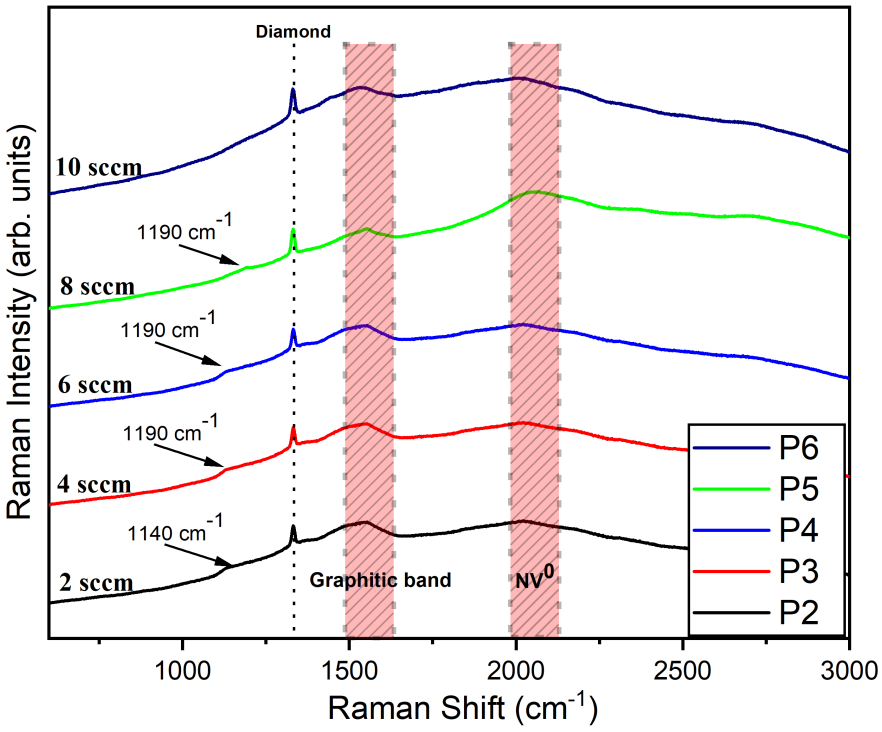

(a)

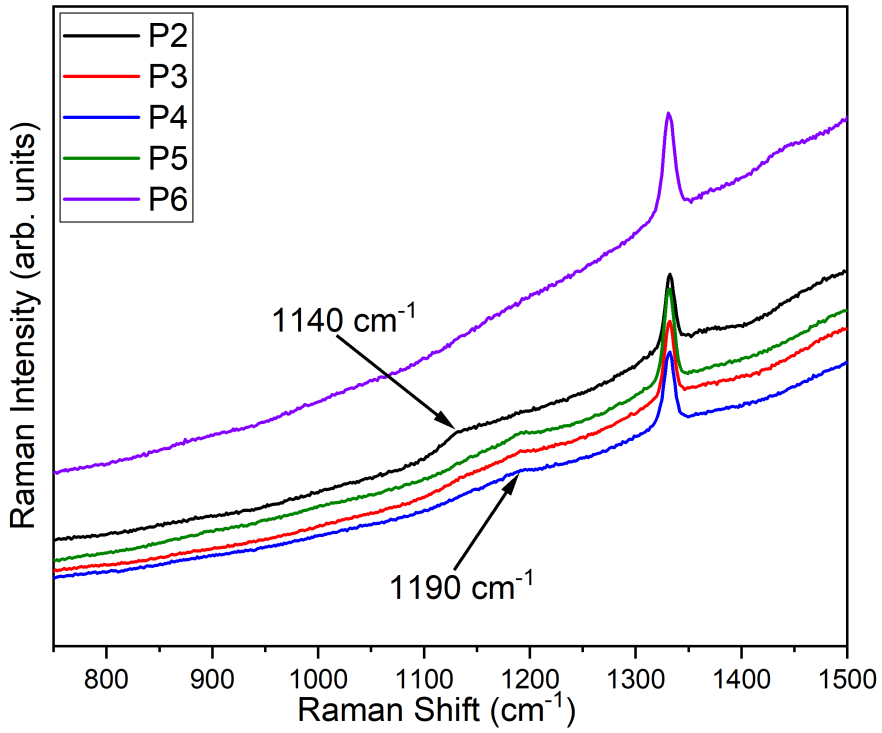

(b)

Figure 4.5: (a) Raman spectra of nitrogen doped samples. Diamond peaks are visible around 1332 cm^{-1}, the G-bands are observed around 1500 - 1600 cm^{-1}. An additional broad peak observed around 2000 - 2063 cm^{-1} indicating the Raman shift of NV^0 centres. (b) Magnified view of the Raman spectra of deposited samples in the 1140 cm^{-1} and 1190 cm^{-1} band region.

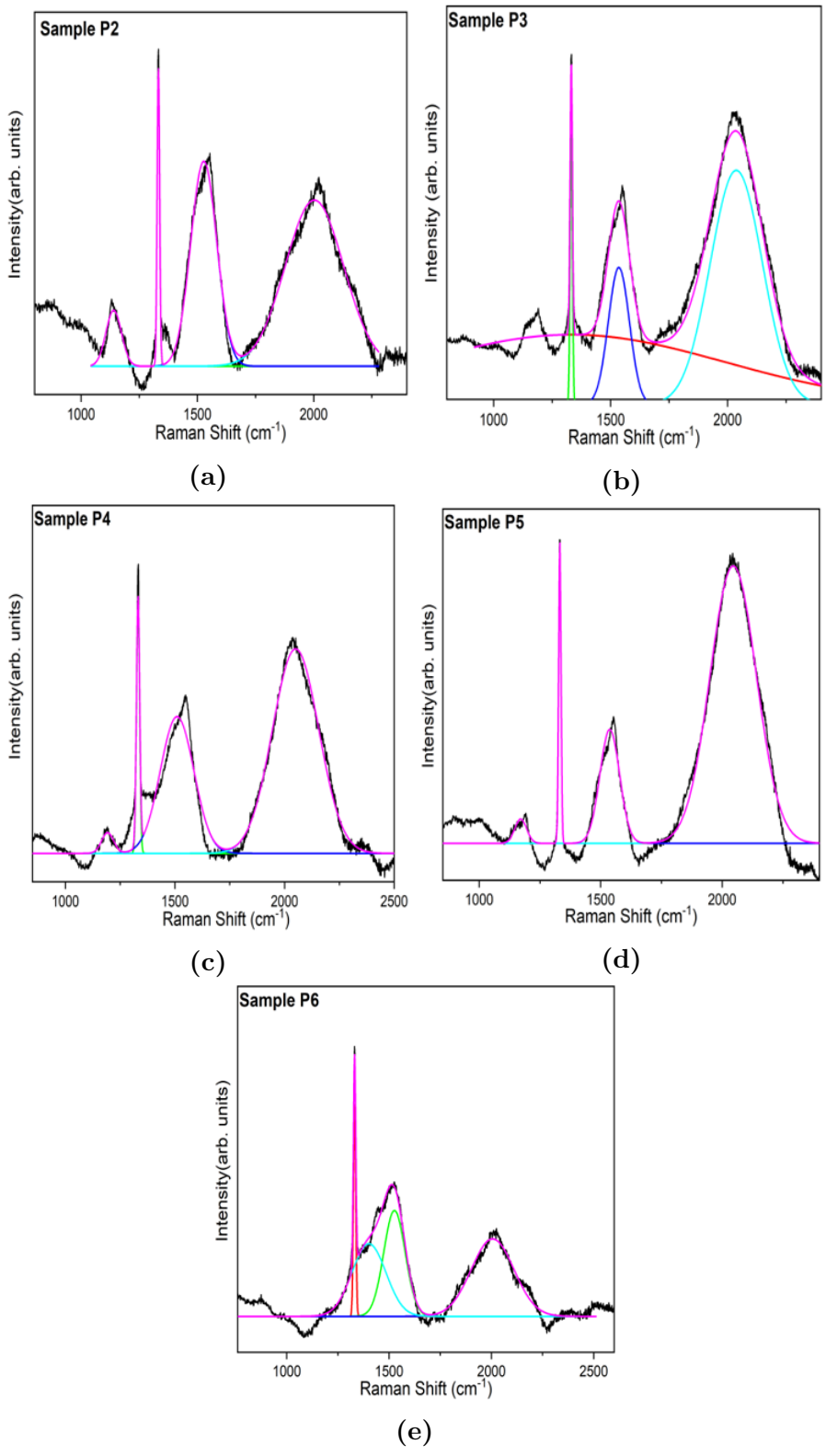

Figure 4.6: Baseline corrected and curve fitted Raman spectra of doped samples P2 - P6. Regions of interest are the FWHM of the G-peak and the 2063 cm^{-1} of the NV^0 centres appearing in the Raman spectra of samples. Peaks at 1332 cm^{-1}, 1500 - 1600 cm^{-1}, and NV^0 centres at 2063 cm^{-1} was fitted with a combination of Lorentzian and Gaussian functions.

at around 10 sccm (sample P6). This result illustrates a huge population of NV^0 at the 8 sccm nitrogen concentration. It can also be seen from Table 4.3 that the intensity of the NV^0 centres in sample P2 is about the same value as in sample P6, nevertheless NV^- centres were not observed in sample P2.

Table 4.3: Quality Factor, full width half maximum (FWHM) of G-band, and the normalized intensity of NV^0 centres of the deposited films.

Samples	Q-factor (514.5 nm)	FWHM (G-band)	NV^0 Intensity (Normalized)
P2	0.982	131.9 ± 1.6	0.49
P3	0.987	123.5 ± 4.5	0.78
P4	0.988	113.4 ± 4.7	0.78
P5	0.990	106.0 ± 1.7	1
P6	0.991	95.6 ± 4.5	0.44

4.3.3 Surface Morphology and Roughness Analysis

To better understand the results obtained from the micro-Raman spectroscopic studies, the surface morphology of the deposited films was observed using SEM and AFM. Figure 4.7 shows the surface morphology evolution of the deposited films and their corresponding topography maps. Sample P1, deposited in the absence of nitrogen gas is added to the series for comparison. The films exhibit distinct surface morphology under different nitrogen doping levels as revealed by the surface micrographs. Without the introduction of surface nitrogen (as seen in P1), the grains were micro-sized with random orientations. However, the introduction of surface nitrogen (as shown for P2 - P5) led to a preferential growth of grains on the surface of the PCDs. The preferentially grown grains satisfy a number of criteria consistent with being NCDs. First, the films showed evidence of facets at high magnification as observed by AFM (see Figure 4.8 (a)). Second, is the presence of Raman lines at around 1140 cm^{-1} and 1190 cm^{-1} as revealed by the Raman spectroscopy shown in Figure 4.5b. The peaks 1140 cm^{-1} and 1190 cm^{-1} are reflective of the presence of sp^2/a-C phases in the grain boundaries [188, 189] of the NCDs. It is also interesting to note that the growth of NCDs

across the surface of the films decreases with an increase in nitrogen flow rate, which was the reason for the disappearance of the 1140 $^{-1}$ and 1190 cm^{-1} peak as high nitrogen flow rates is approached.

A quantitative analysis of the area occupied by the micro-sized grains and grain boundary line density (i.e the number of grain boundaries per unit area under the assumption that the grains are square in shape and the grain boundaries are the sides of the square shaped grains) for every 17.5 μm^2 area measured on the surface of sample P2 to P6 respectively is given in Table 4.4. The Table shows that an increase in the micro-grained area with an increase in nitrogen flow rate was observed while the grain boundary line density decreased. Inspection of the SEM images revealed the presence of abnormal outgrowth on the surface of sample P3 as shown in Figure 4.8(b). This abnormal grain growth on the surface of sample P3 demonstrates well structured and layered diamond grains that could be useful as an NV scanning probe if optical centres are well located at the tip of the structure.

Table 4.4: A qualitative analysis of the grain boundary line density and the area occupied by micro-grains on the surface of the deposited films.

Samples	Area occupied by micro-sized grains (μm^2)	Grain boundary line density (μm^{-2})
P1	-	-
P2	4.58 ± 0.67	1.5×10^3
P3	5.49 ± 0.12	1.1×10^3
P4	7.03 ± 0.11	9.8×10^2
P5	9.96 ± 0.17	7.4×10^2
P6	11.53 ± 0.52	6.1×10^2

The surface roughness of diamond can be of immense importance for several optical applications. For instance, when using NV centres in diamonds for magnetic field sensing applications, the light dissipation from scattering will be intolerable when the surface roughness

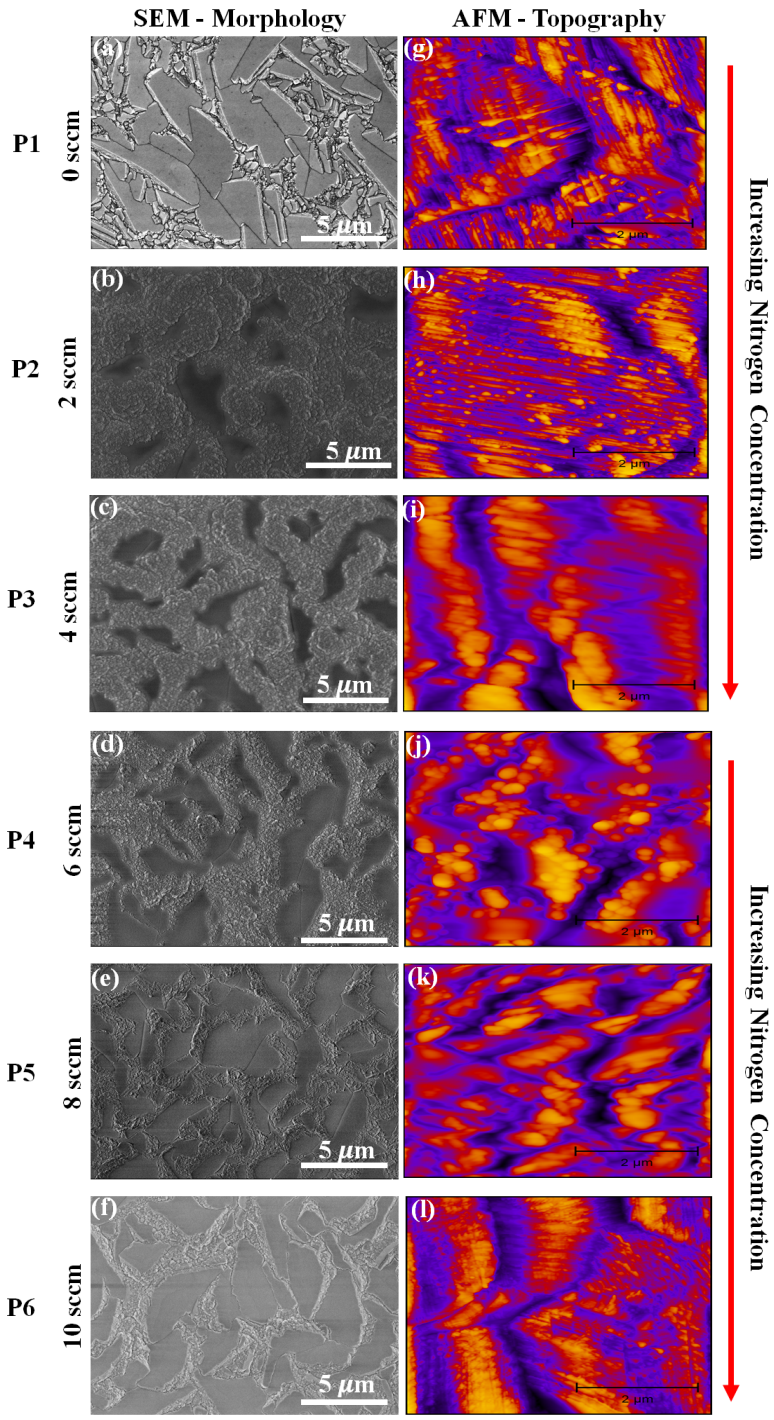

Figure 4.7: Surface micrographs and topography of films (a-f) surface morphology samples P1 - P6 (g-l) surface topography of samples P1 - P6. Surface topography maps were collected at 5 μm $\times$ 5 μm scan range. The population of NCDs decreases with an increase in the surface nitrogen concentration.

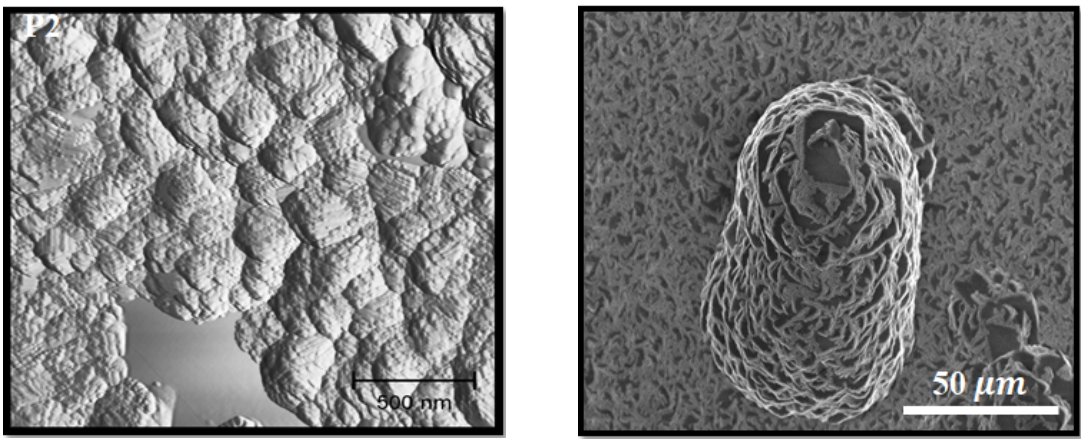

Figure 4.8: (a) High resolution AFM amplitude map of nanograined areas imaged in sample P2 (b) SEM surface morpholpogy of grain outgrowth in sample P3. The presence of abundant NV centres in this grain bulge could make it useful as a crude scanning probe.

is larger than some critical value [190, 191]. From an NV centre perspective, a high surface roughness of diamond induces thermal noise which can affect the minimum magnetic field sensitivity of the NV centres. For this reason, polycrystalline diamonds with high surface roughness are not desirable for an optimized NV magnetometer. To determine the surface roughness S_a (mean roughness) and S_q (RMS roughness) of the samples, AFM was used to characterize the morphology of the deposited films. The parameters S_a and S_q are defined as:

$$S_a = \frac{1}{A} \iint_A \mid P(x, y) \mid \, dx \, dy \tag{4.3}$$

$$S_q = \sqrt{\frac{1}{A} \iint_A P^2(x, y) \, dx \, dy} \tag{4.4}$$

where $P(x, y)$ and A are the current surface height and the area of sample in consideration respectively. Figure 4.9 shows a plot of the RMS and mean surface roughness of the PCD samples as a function of the surface nitrogen concentration. An increase in the surface roughness of the sample with increased nitrogen concentration was observed until a surface nitrogen concentration of about 8 sccm, where the surface roughness decreased. A 6 sccm surface nitrogen addition resulted in a high degree of surface roughness. Beyond $[N_2/CH_4 + N_2] = 0.8$, high surface nitrogen doping decreases the surface roughness.

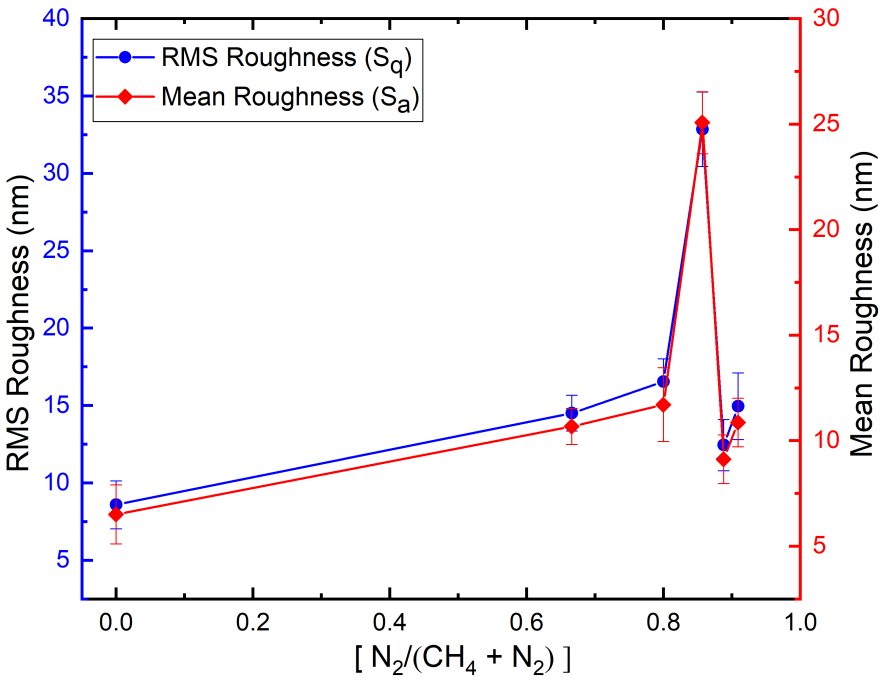

Figure 4.9: RMS and mean roughness vs concentration of surface nitrogen impurities. Roughness analysis was carried out at 5 μm × 5 μm scan range of the deposited films.

4.3.4 Structural Characterization

In order to examine the structure and texture of the films deposited at the surface of the PCDs under varying surface nitrogen flow rates, grazing incidence X-ray diffraction was used to characterize the surface of the films. Shown in Figure 4.10 are the GIXRD patterns of the films. Diffraction patterns were taken in the range $25° \leq 2\theta \leq 90°$. As shown in Figure 4.10, diamond diffraction peaks of (111) and (220) are observed around 43.9° and 75.3° respectively. In the XRD spectra presented, the broadening of the peaks is due to the combined effect of crystallite sizes and micro-strains. The FWHM obtained from the broadening of diffraction reflections, average grain sizes, and micro-strains ϵ for samples P2 - P4 were determined using the Williamson-Hall method [192]. According to our calculations, the average size D of the nano-grains for samples P2 - P4 was determined to be 130.80 ± 0.3 nm, 117.50 ± 0.5 nm, and 243.74 ± 0.1 nm. For larger grain sizes, for example in sample P5 and P6, it was more efficient to calculate the grain sizes from the SEM or AFM maps. This is because the diffraction reflection for diamond grains exceeding 250 nm in size are the same as that for the reference crystals selected. The average grain sizes for sample P5 and P6 were estimated

to be 808.38 ± 0.6 nm, and 1.76± 0.38 μm respectively. Additionally, the values of the micro-strain ϵ in the samples P2 - P6 were also determined to be 0.00683 ± 0.02, 0.00842 ± 0.07, 0.00534 ± 0.01, 0.00736 ± 0.05, and 0.00683 ± 0.02 for sample P2 - P6 respectively.

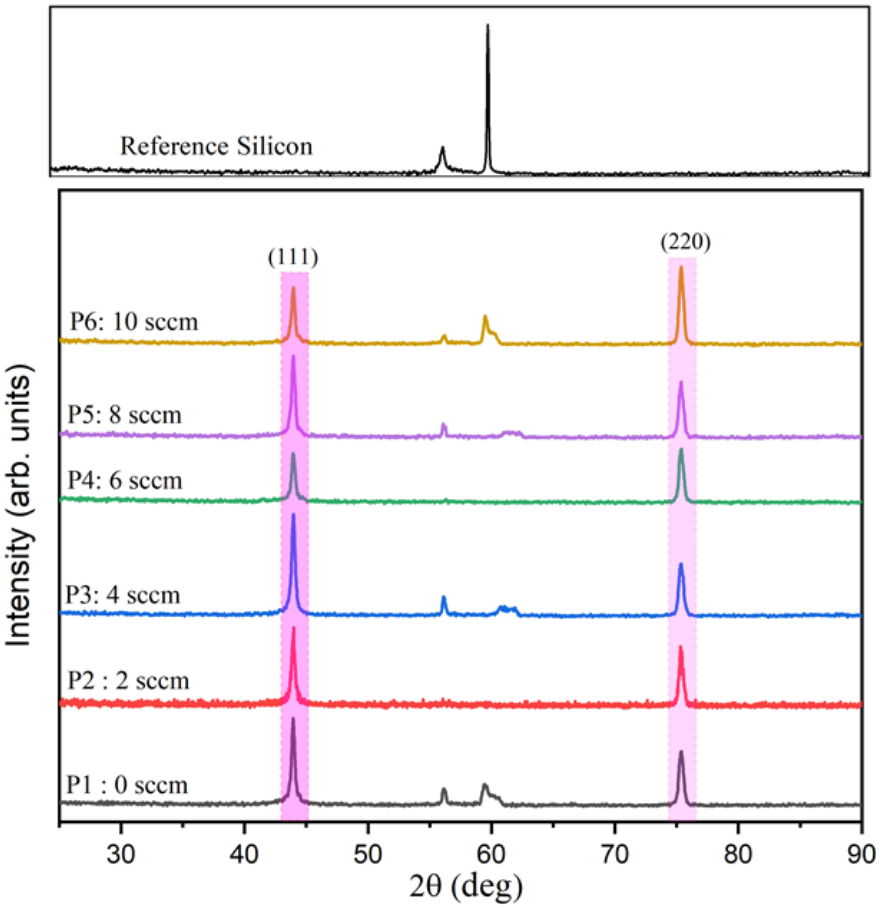

Figure 4.10: X-ray diffraction pattern of diamond films deposited on silicon substrate

As revealed in Figure 4.10, the intensity of the diffraction peaks observed vary with the concentration of surface nitrogen introduced. The ratio of the intensity of the (111) peak to that of the (220) peak, $I_{(111)}/I_{(220)}$ of sample P1 was calculated to be 1.6, which is larger than the 1.0 obtained for powders with no texture [193]. This indicates that a (111) texture is favoured in the undoped diamond film. For sample P2 and P3, a (111) textured is also favoured. Further increase in the surface nitrogen flow rate to about 10 sccm reduces the $I_{(111)}/I_{(220)}$ to 0.74 implying that a high surface nitrogen doping reduces the amount of grains in the (111) crystallographic direction.

4.4 Discussion

4.4.1 Formation of 1140 cm^{-1} and 1190 cm^{-1} Raman Peak

The 1140 cm^{-1} peak observed on the surface of sample P2 is hypothesized to be due to the formation of *trans* polyacetylene (*trans* PA) type bonds in the grain boundaries of the film. These *trans* PA type bonds have been shown in the literature [194, 195] to be a combination of C = C chain stretching and C−H wagging modes. In addition, the *trans* PA peaks are used as a characteristic signature of nanocrystalline diamonds [194]. Thus, the 1140 cm^{-1} feature on sample P2 suggests a high degree of nanocrystalline grain formation on the surface of the films doped with low surface nitrogen concentrations. This conclusion is consistent with the SEM micrographs of sample P2 shown in Figure 4.7. Also, of importance to this study is the origin of the 1190 cm^{-1} peak observed in the Raman spectra of the deposited films. Several authors in Refs. [196, 197, 198, 199] have reported the appearance of a similar 1190 cm^{-1} peak in nanocrystalline diamonds (NCDs) when using an excitation wavelength of 514 nm. Nevertheless, the origin of this peak still remains a source of controversy. Some researchers attribute the peak to the Raman photon scattering from C−N bonds positioned within the grains or grain boundaries, while others have attributed it to the Raman scattering of C=N−H bonds in the grain boundaries. Of utmost importance is that the 1190 cm^{-1} peak appears with an increase in the G-band, thus implying a strong correlation with the sp^2 bonded orbitals in diamond films [200]. The 1140 cm^{-1} and 1190 cm^{-1} peaks therefore indicate an increase in the amorphous carbon content in the films in which they appear. These peaks are missing in the Raman spectrum of sample P6, thus suggesting a low concentration of amorphous carbon content in the high nitrogen concentration film. The low amorphous carbon content in sample P6 is a possible reason for the appearance of NV^- centres in the film.

4.4.2 Surface Morphology and Topography of Films

Following the analysis of the morphology presented in Figure 4.7, it can be deduced that the growth of surface nano-grains are favoured at low surface nitrogen concentration while

the growth of micro-sized grains are hindered. This result is in agreement with the work of Kuntumalla et al. [195]. The introduction of low nitrogen concentration appears to enhance secondary diamond nucleation thereby inducing the formation of a large density of NCDs across the surface of the PCDs. According to Rabeau et al. [201], secondary nucleation may be accomplished by the partial replacement of hydrogen gas with inert gases (for example, argon, helium, or nitrogen) at low pressure during the CVD process. Overall, as the surface nitrogen flow rate increases (and the actual atomic nitrogen content in the PCD films increases), secondary diamond nucleation decreases thereby reducing the amount of sp^2/a-C content present in the NCDs deposited on the surface of the diamond films.

The reason for an increase in the area occupied by micro-grained diamond with increasing nitrogen flow rates may be understood from a grain size increment perspective. Yiming et al. [202] have shown theoretically that an increase in the concentration of nitrogen substitutionally positioned within the diamond surface will result in an increase in the grain size and a growth rate improvement of the diamond films. Additionally, the grain boundary analysis reveals a decrease in the grain boundary line densities as the nitrogen flow rate increases. The introduction of surface nitrogen in concentrations other than 10 sccm led to an increase in sp^2/a-C content in the films likely because of the increased grain boundary line density. An accumulated sp^2/a-C content in the grain boundaries results in the quenching of the PL intensity of the NV^- centres. It has also been shown from our previous studies in chapter 3 [90] that a further increase in the nitrogen flow rate beyond 10 sccm causes an absorption of the PL emission from the NV centres and degrades the crystalline quality of the diamond films. This sets an optimal limit of 10 sccm nitrogen flow rate for the formation of surface NV^- centres in polycrystalline diamonds at our low pressure of about 30 Torr. Although several authors [203, 204, 205] have demonstrated an increase in the sp^2/sp^3 bonding fraction as the nitrogen concentration increases for CVD diamonds, here we observe some degree of non-linearity in the sp^2/sp^3 bonding fraction as the nitrogen flow rate increases. An increase in the sp^2/sp^3 bonding fraction results in an increase in the surface conductivity of the deposited films. However, our previous result given in chapter 3 and Ref. [90] indicates a decrease in

the surface conductivity of the film grown with 10 sccm nitrogen flow rate compared to films grown at lower nitrogen flow rates. This result further confirms the non-linearity observed at 10 sccm flow rate. We speculate that the gas phase chemistry during nitrogen doping at the deposition parameters examined might be responsible for the non-linearity observed. In general, what can be inferred from the data here is that low nitrogen concentration leads to a grain refinement that introduces a high degree of disordered sp^2/a-C content in the grain boundaries which quenches NV^- centres.

The surface roughness analysis of the deposited films gave further information about the robustness of PCDs for use as NV based detectors. As anticipated, sample P6 demonstrates low surface roughness which is essential for reducing thermal noise due to heat dissipation at the surface. The reduced thermal noise aids in improving the detectable magnetic field if sample P6 were to be used for magnetic field sensing applications. It has been shown by Tang et al. [206] and Cicala et al. [207] that NCDs in general have low surface roughness, however, the result presented here shows a decrease in surface roughness with an increased grain size. Several factors can affect the surface roughness of deposited films, for example, the film material, the orientation of the grains, and surface state of the films. Here, the changes observed in the surface roughness of the deposited films is explained from a surface state perspective. It is conjectured that there is a linear relationship between the surface roughness and nucleation sites [208]. Surfaces with more nucleation sites (the appearance of more grains) tend to have a higher degree of roughness compared to those with less nucleation sites. Secondary nucleation occurring at the surface of the PCDs is the main reason for the changes in the surface roughness parameters. Undoped samples and samples doped at high concentration (8 - 10 sccm) have less secondary nucleation sites, hence the reason for their low surface roughness.

4.4.3 Effect of Surface Nitrogen on the Crystallographic Orientation

As may be observed in Figure 4.11, low surface nitrogen concentration induces an increased proportion of (111) textured grains, while a high concentration at 10 sccm reduces the proportion of (111) textured grains with a preferred orientation in the (220) direction. To further confirm our GIXRD results, another set of experiments was carried out and the results of these experiments were compared with the previous experiments in Figure 4.11. A summary of the orientation of the deposited films and the ratio of intensity of the (111) diamond peaks to the (220) peaks is reported in Table 4.5. From the comparison in Figure 4.11, it appears that the crystallographic orientation of films is mostly random at low surface nitrogen concentration; a preferred orientation is chosen randomly and the mechanism for this is still not well understood. In contrast, films were highly oriented in the (220) direction at high surface nitrogen concentration, for example, at 10 sccm. At 10 sccm, it may be possible that nitrogen dopant act as a grain refiner thus aiding in the transition from (111) texture to (220) texture. Possibilities exist that at high nitrogen flow rates, the nitrogen atoms are preferentially absorbed at the non - (111) planes of micro-size diamonds. Since nitrogen increases the growth rate, this may have lead to an increased amount of the non - (111) grains in the film. Furthermore, obtaining a favoured orientation in the (220) direction suggests the possibility of controlling the orientation of diamond grains in the (220) direction using high nitrogen concentration while keeping the methane and hydrogen concentration fixed. This result is complementary to the work of Jia et al. [209] where it was shown that the orientation of diamond films can be controlled by tuning the methane concentration and microwave power during CVD. Our approach may be a more favoured method because it is relatively easy and does not involve the control of more than one parameter.

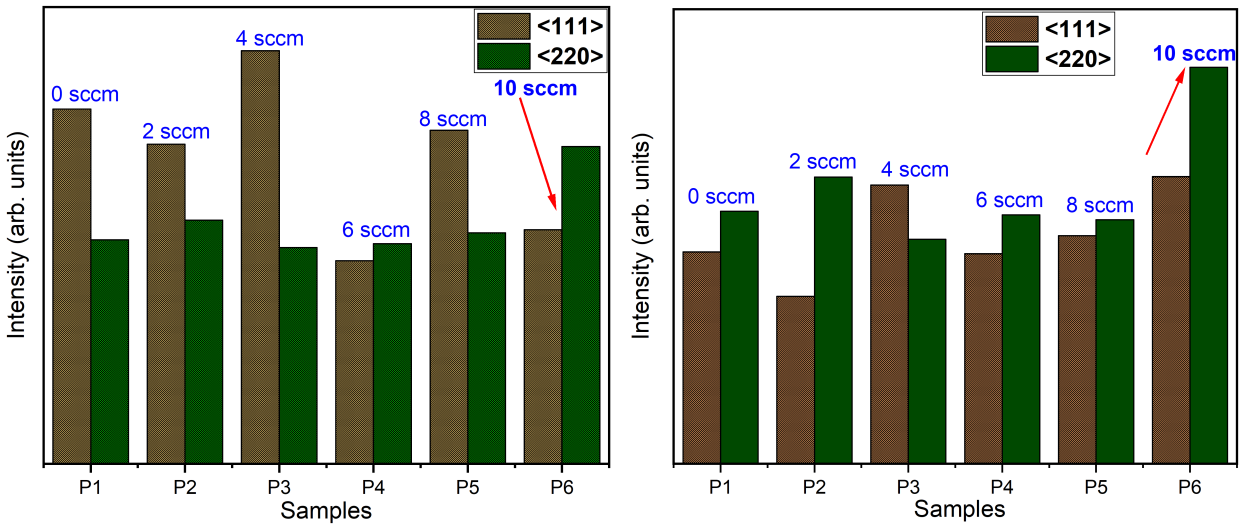

Figure 4.11: An intensity chart showing the orientation of the deposited films with varying nitrogen concentrations (a) ratio of $I_{(111)}/I_{(220)}$ for the first experiment (Experiment A) (b) ratio of $I_{(111)}/I_{(220)}$ for the second experiment (Experiment B). Introducing 10 sccm of surface nitrogen favours grain orientation in the < 220 > direction.

4.4.4 Possible NV^- Centres Creation Mechanism in Quasi-similarly Doped PCD Films

The PCD films synthesized in this paper are quasi-similarly doped and as revealed by XPS analyses of samples, we can infer that NV centres occur in their neutral states when the actual [N/C] is less than 0.0025, and as the [N/C] ratio increases NV centres in their negatively charged states are formed. This is because nitrogen acts as an electron donor and can transfer electron to the neutral charged centres. This result is in agreement with the work of Chen et al [91]. Also, inference from the Raman spectra results indicates a high degree of sp^2 structural disorder at low nitrogen concentration and this could explain the dominance of NV^0 centres at the surface of the films. Films with low structural disorder and high [N/C] ratio like sample P6 are therefore likely to hold more negatively charged NV's at the surface and this was indeed the case of the sample reported earlier by Ejalonibu et al. [90] (in chapter 3). Based on these correlations, a model for the formation of NV^- centers in quasi-similarly doped polycrystalline diamonds synthesized at low pressure is diagrammatically proposed in Figure 4.12:

Table 4.5: Preferential orientation of the deposited films under varying surface nitrogen concentration

Samples	Experiment A $[I_{(111)}/I_{(220)}]$	Experiment B $[I_{(111)}/I_{(220)}]$	Preferred Orientation
P1	1.583	0.532	Random
P2	1.313	0.584	Random
P3	1.912	1.242	< 111 >
P4	0.922	0.844	< 111 >
P5	1.444	0.935	Random
P6	0.738	0.724	< 220 >

1. At low surface nitrogen flow rates ([N/C] < 0.0020), the diamond growth mechanism is slow enhancing a secondary nucleation process that favours the growth of nanocrystalline grains. The nanocrystalline grains formed have large grain boundary density containing a large quantity of disordered sp^2/a-C content in the grain boundaries.

2. At medium surface nitrogen flow rates (0.0020 < [N/C] < 0.0022), grain size increases which introduces some degree of orderliness to the sp^2 content in the grains and at the grain boundaries. The quantity of sp^2/a-C phases present at this stage still prevents the formation of NV^- centres.

3. At high surface nitrogen flow rates([N/C] > 0.0025), the quantity of nano-grain sized diamond reduces except at the grain boundaries.The degree of disordered sp^2/a-C content decreases with increasing grain size thereby enabling the formation of NV^- centres on the grains. Also, the grain boundary line density is greatly reduced.

In the proposed mechanism, low surface nitrogen induces some level of non-diamond carbon phases which may inhibit the formation of NV^- centres. Importantly, the actual amount of atomic nitrogen present in the PCD films also plays a role. To locate stable NV^- optical centres in PCDs at low growth pressure, this experiment confirms that carefully chosen doping concentration is needed. In particular, reduced sp^2/a-C content, optimized $[N/C]$ ratio,

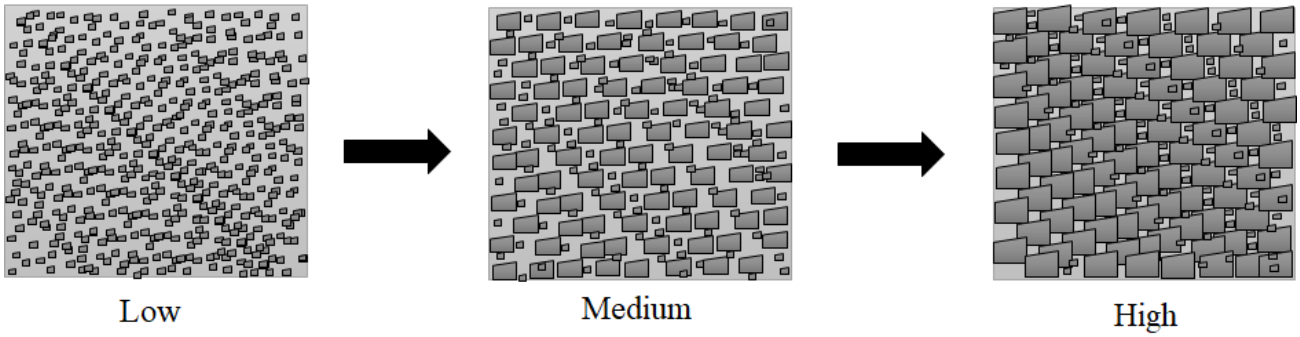

Figure 4.12: Proposed growth mechanism for the surface morphology of polycrytalline diamonds under step-wise surface nitrogen doping. NCD grains are dominant at low surface nitrogen flow rate while they aggregate into larger grains with an increase in nitrogen-flow rate. The lower disordered sp^2/a-C content and increased grain size in PCD films formed with high surface nitrogen flow rates enables the formation of NV^- centres.

and minimal grain boundary line density is desired for the formation of stable NV^- centres at low deposition pressure. Although other surface conditions such as hydrogen termination may result in the quenching of useful NV centres, here we have shown that using a 10 sccm surface nitrogen flow rate for 1 hour gives the desired sp^2/a-C content and grain boundary line density necessary for NV^- centres formation at low deposition pressure.

4.5 Conclusion

In summary, the effect of step-wise nitrogen doping and its consequences on the formation of useful NV centres in PCDs has been investigated in a MPCVD apparatus when the microwave power and substrate temperature are kept at 800 W and 700^{o}C respectively to understand the principle behind the formation of NV centres in PCDs deposited at low pressure. Surface properties of the deposited films were probed using Raman spectroscopy, PL spectroscopy, SEM, AFM, XPS, and GIXRD. The results obtained from Raman spectroscopy and validated by SEM micrographs revealed the formation of nano-grains with a high-degree of disordered sp^2/a-C phases at low nitrogen concentrations. The degree of disordered sp^2/a-C phases decreased with an increase in nitrogen flow rates. The degree of disorderliness of the sp^2 bonds and the actual nitrogen content in the films was found to have a strong influence on

the formation of NV^- centres in diamond grown at low pressure. In fact, in low sp^2 disordered grains, NV^- were found to be formed likely because there were little amounts of impurities available for quenching the NV^- centres. It was also found that high nitrogen flow rates limits grain boundary evolution thereby reducing the amount of sp^2/a-C phases found in the grain boundaries of the deposited films. Low surface roughness of approximately 8 - 10 nm were obtained for films with high nitrogen concentrations. The low surface roughness of high nitrogen doped diamonds enables their use for optimized NV center detectors. Finally, the results obtained from GIXRD indicate the formation of highly oriented grains in the (220) crystallographic direction, therefore indicating the possibility of obtaining highly textured films by changing the flow rate of the nitrogen gas during CVD. Ultimately, CVD diamonds are prone to hydrogen termination at the surface in addition to other impurity contents that may result in the quenching of NV^- centres. Implementing a series of heat and chemical treatment have been used by others to functionalize and stabilize NV^- centres in diamonds. We propose that tuning the nitrogen concentration during CVD as reported in this work is a more feasible approach to obtaining an ensemble of active NV^- centres in diamond grown at low pressure. It is anticipated that this work will provide a basis for understanding the principle for the formation of NV^- centres in PCDs grown at low pressure useful for magnetic field sensing and other quantum applications.

4.6 Future Outlook

The field of NV centre fabrication in PCDs is a scarcely researched area owing to the difficulties involved in the process. Nevertheless, the author of this dissertation has taken time to explore this area extensively in chapter 3 and chapter 4. The main highlight of these chapters is in the careful selection of an optimal parameter for the growth of NV optical centres in PCD diamonds and the understanding of a possible mechanism for the formation of NV centres at low pressure. While our experimental exploration goes a long way in the understanding of the formation processes of NV centres in PCDs deposited at low pressure, insights and interest in this area is still evolving. The following problems need a solution before films deposited using this method can be used for magnetic field sensing applications:

1. **Orientation of NV centres:** Preferential orientation of NV centres in diamond films is targeted at limiting unwanted background noise, increasing sensitivity, and simplifying device operations [111]. The preferential orientation of NV centres has been achieved in SCDs [117, 118], this result however remains a nightmare in PCDs because of the random orientation of grains. While it is not experimentally feasible to engineer perfectly preferentially oriented NV centres in PCDs, it is possible to have approximately 70% of the grains containing NV centres aligned in the same crystal direction. This can be achieved via careful deposition parameter(s) tuning as demonstrated in this chapter.

2. **Stabilizing surface charge state:** In most cases, NV centres located within a few nanometers from the diamond surface are found in their neutral charged states [90]. This becomes a critical problem in PCDs because of the presence of grain boundaries and nanocrystalline diamonds at the surface harbouring a huge amount of graphitic impurities. Certainly, there is a need to understand the mechanism of charge state conversion in both SCDs and PCDs. Commonly studied is the mechanism of NV centre formation and charge state conversions in SCDs. However, to date, there have been no studies explicitly detailing the same in PCDs.

The above listed are some challenges that need to be addressed before advancing in the use of PCDs for magnetic field sensing applications. Note that it is not the aim of this thesis to address all gaps listed but to establish the possibility of using this fabricated material for sensing applications. In the following chapter, a novel NV sensor magnetometer for wide-field magnetic sensing applications was designed and constructed. The detector developed was later tested for performance by utilizing it to sense inhomogeneous fields in a typical Halbach magnet configuration.

Chapter 5

On the design and performance testing of a scalable NV detector for magnetic sensing application.

"Whatever is in your magnetic field is attracting to itself, and so the more love in your field, the more power you have to attract the things you love."

– Rhonda Byrne

Some part of this chapter is based on the manuscript:

Ejalonibu, H., Sarty, G., & Bradley, M. (2021). Towards the design and operation of a uniformly illuminated NV detector for magnetic field mapping application. (to appear in the Journal of *Measurement Science and Technology*, IOP).

5.1 Introduction

In recent times, the unceasing demand for magnetically based medical devices has motivated research directed towards the development of novel sensors for the detection and characterization of magnetic fields. The rapid progress made in the development of magnetically based miniaturized medical devices integrated with field sensors has greatly improved the quality of everyday life [210]. Examples of magnetically based medical equipment include MRIs, blood separators, magnetic switches, e.t.c. [211]. Of the listed devices, MRIs are the

most interesting yet complicated devices which produce high-resolution images of internal organs and aid in the diagnosis of a variety of diseases. The magnet configuration in traditional low-field MRI systems is designed to have a uniform static B_0 field. Recently, however, low-field MRI magnets are now designed with inhomogeneous B_0 fields, where the B_0 field can be shaped in such a way that there is a region of a homogeneous field in the imaging field of view (FOV) surrounded by an inhomogeneous field. An example reference to a magnet configuration with an inhomogeneous B_0 field is in the work of Sarty and Vidarsson [212].

Several methods have been developed to sense and characterize inhomogeneous radially-varying static magnetic fields in low-field magnets. Static magnetic field sensing with SQUIDs, Hall effect sensors, and AVMs are common methods. An exact spatial quantification of the B_0 field in magnet configurations of such is needed to generate an accurate image from associated MRI systems. Reports on the use of SQUIDs and AVMs as magnetic field detectors at low and ultra-low fields have been discussed in chapter 1 and can also be found in Refs. [28, 29, 30, 31, 4, 36, 37]. Although SQUIDs offer exceptional sensitivity, the presence of magnetically shielded room and cooling of elements with liquid nitrogen or helium is needed for their operation [32, 33]. Additionally, to obtain high sensitivities and long T_1 times for the alkali spins, AVMs of size in the order of cm^3 are needed, thus making them bulky and not applicable for compact applications. Clearly, existing sensor types cannot satisfy the requirements of a combination of high magnetic field sensitivity and spatial resolution, compactness, and ambient temperature operations needed for low magnetic field sensing. Also, it would indeed be a huge time investment for a technician to utilize a SQUID or AVM for magnetic field characterization in the laboratory.

Here, it is proposed that the problem of bulkiness associated with the use of AVMs and other related magnetic field sensors can be solved using quantum materials based on spin qubits found in diamonds possessing remarkable magnetic properties. Given the rapid progress in the area of quantum sensing, one would expect that reasonable progress should have been made in the integration of such detectors with magnetically based medical devices e.g low-

field MRIs. Particularly, the technology we seek must be scalable and accessible outside the laboratory setting. Furthermore, it is expected that the construction and operation of these miniaturized sensors is made simple enough to be easily set up by nonspecialists (those with little or no experience working with NV centres). A few recent papers [213, 214] have targeted the development of compact devices based on NV centre magnetometers without comprehensive details. As a result, we feel it will be important and helpful to provide a comprehensive and detailed description of the construction and operation of a simple but scalable NV centre detector for magnetic field detection. The author of this dissertation would like to point out that there are major distinctions between papers published in the construction of NV centre magnetometers and the sensor designed here. The setup presented in this chapter is different from other setups found elsewhere because: (i) it reduces the complexity associated with confocal microscopy widely used for harnessing the properties of NV centres in diamond (ii) the system is simple and scalable; making it possible to further miniaturize by replacing bulky electrical and microwave components with integrated circuits and software-defined radios (SDRs).

In this chapter, the design and construction of a new NV sensor system is described; the main aspect of the design including the design parameters, optics, microwave engineering, and electronics were detailed. In addition, we tested the new system by comparing its emission line performance from experimental fluorescence (FL) maps obtained with that of a confocal system under varying optical powers. The new system status and proposed performance for sensitivity to fluorescence emission were accessed in terms of signal-to-noise ratio (SNR) and signal-to-background ratio (SBR). In conclusion, the extendibility, scalability, and limitations of the design are discussed.

5.2 Theory

Although the electronic structure, optical, and spin properties of the NV centre have been discussed in chapter 2, it is necessary to briefly highlight the main properties of the colour

centre which make it attractive to the bio-imaging community. The NV centre emits red fluorescence signals in the energy range 1.65 - 2.0 eV (637 - 750 nm) when pumped using a green laser of about 2.33 eV (532 nm) photon energy. The emitted fluorescence can be used to detect spin transitions induced by microwave radiation, thus leading to optically detected magnetic resonance (ODMR). The orbital ground and excited states of the NV centre are spin-triplets, labelled as ($^3A_2$), and (^3E) respectively. The $^3A_2$ and ^3E states have three sublevels with magnetic quantum numbers $m_s = 0, \pm 1$. Here, m_s is the spin projection along the NV centre quantization axis. To further understand the magnetic sensing applications of the NV centre, the ground state ($^3A_2$) Hamiltonian $\hat{\mathbf{H}}$ in the presence of static magnetic field is given by:

$$\hat{\mathbf{H}}/\hbar = D\left(\hat{\mathbf{S}_z}^2 - \frac{2}{3}\right) + \gamma_e \overrightarrow{\mathbf{B}} \cdot \overrightarrow{\mathbf{S}}, \tag{5.1}$$

where $\hbar$ is the Planck constant, $D = 2.87$ GHz is the zero-field splitting parameter, $\overrightarrow{\mathbf{B}}$ is the magnetic field vector, $\gamma_e = 28$ MHz/mT is the gyromagnetic ratio of the electron spin in the NV, and $\overrightarrow{\mathbf{S}}$ is the S = 1 spin operator. If the B_0 field is applied along the NV crystallographic axis (chosen as the **z** direction by convention), the Hamiltonian $\hat{\mathbf{H}}$ becomes:

$$\hat{\mathbf{H}}/\hbar = D\hat{\mathbf{S}_z}^2 + \gamma_e B_0 S_z, \tag{5.2}$$

under this condition a splitting in the $m_s = \pm 1$ sublevel is observed as given by $\Delta E = \gamma_e B_0$, and the applied B_0 field is determined through the detection of the Zeeman shifts of the NV defect ground state spin sublevels. Note that the energies of the $m_s = \pm 1$ sublevels is linearly proportional to the applied magnetic field B_0 - the principle of the NV centre sensor is based on the optical detection of this energy shift.

To compare optical instruments, it is important to choose a standard metric for performance comparison. Customarily, one is interested in how sensitive an optical design is, nonetheless, sensitivity can be measured in several different ways. Some common metrics used to measure sensitivity include SBR, SNR, the lower limit of detection (LLD), and the Z' factor to mention a few. In optical designs, an ideal metric will take into consideration the mean signal, mean

background, signal variation, and background variations. Here, two important metrics for performance comparison used in this chapter were defined.

1. SBR is the ratio of the mean signal level to the mean background level given by:

$$\text{SBR} = \frac{\text{Mean Signal}}{\text{Mean Background}} \tag{5.3}$$

   The SBR ratio is however regarded as an inadequate measure of sensitivity because it does not account for signal variation or background variation [215]. It does not provide a means of comparing between two instruments with different background variability.

2. SNR is regarded a better metric than the SBR and it is defined as:

$$\text{SNR} = \frac{\text{Mean Signal} - \text{Mean Background}}{\text{Standard Deviation of Background}} \tag{5.4}$$

   The SNR is widely used for determining the integrity of signals. In contrast to the SBR, SNR takes into account variations in the background. It takes into account that the signal quantification integrity increases as the variation in the background signal decreases.

5.3 Detector Design and Construction

A detector system based on an ensemble of NV centres in diamond was designed for the purpose of characterizing the B_0 field in a Halbach magnet configuration. It was required that the proposed design fulfills the following requirements: (a) the detector is sensitive in the mT range and has a sensitivity comparable to a confocal system of detection (b) the illumination or scan area covers the diamond sample at the heart of the NV detector system (c) the detector's power consumption is minimal (d) detector is simple enough to be scalable.

Figure 5.1 is a detailed schematic illustrating the system configuration incorporating optics, RF, and the magnet system highlighted in purple, blue, and red boxes respectively. To understand the design concept, we refer to the theory and role of each component shown in Figure 5.1 and discuss the rationale for choosing each component in the following sections. A

list of all components used in the experimental design with a detailed description of vendors is found in Table 5.1 and Table 5.2.

5.3.1 Optics

The optical components used in this setup are mainly commercial. Although similar confocal systems have been described earlier in Refs. [216, 217, 94], our system differs because of its simplicity and the presence of fewer optical components, thus eliminating optical redundancy. Figure 5.2 shows a photo of the laboratory set-up of this design.

Diamond

A (100) diamond plate (DNV-B1) of $3 \times 3 \times 0.5$ mm^3 (Element Six, Oxfordshire, OX, UK) laser-cut with +/-3° misorientation was placed in the bore of the magnet. The concentrations of NV centres in the crystal as measured by the manufacturer was 300 ppb with a T_2^* time of about 1 μs, and a T_2 value of 100 μs. The NV centres were homogeneously distributed over the diamond sample and randomly oriented along one of the four crystallographic axes of the SCD diamond lattice. It was assumed that the coherent properties of the diamond sample are sufficient for this application, hence no further annealing or chemical treatment was carried out on the sample to improve its properties. A silicon wafer was placed underneath conductive double-sided tape and the diamond sample was placed over the configuration - the same tape was used to transmit the microwave line. Silicon wafer was used because it absorbs approximately 70% of the incident green light, and does not emit red fluorescence. Contrary to the idea of a confocal laser illumination system where a small spot on the surface of the diamond sample is illuminated, the goal of this design was to illuminate the entire sample. The area of the illuminated spot depends on the wavelength of the laser light and the specifications of the beam expander (BE) used to obtain a larger output beam diameter. Since an objective lens was not included in this design, the diffraction-limited spatial resolution was proportional to the excitation wavelength, and the numerical aperture of the object illumination source. The requirement for a diffraction-limited resolution is never fulfilled in this design because every optical component has some imperfection or misalignment associ-

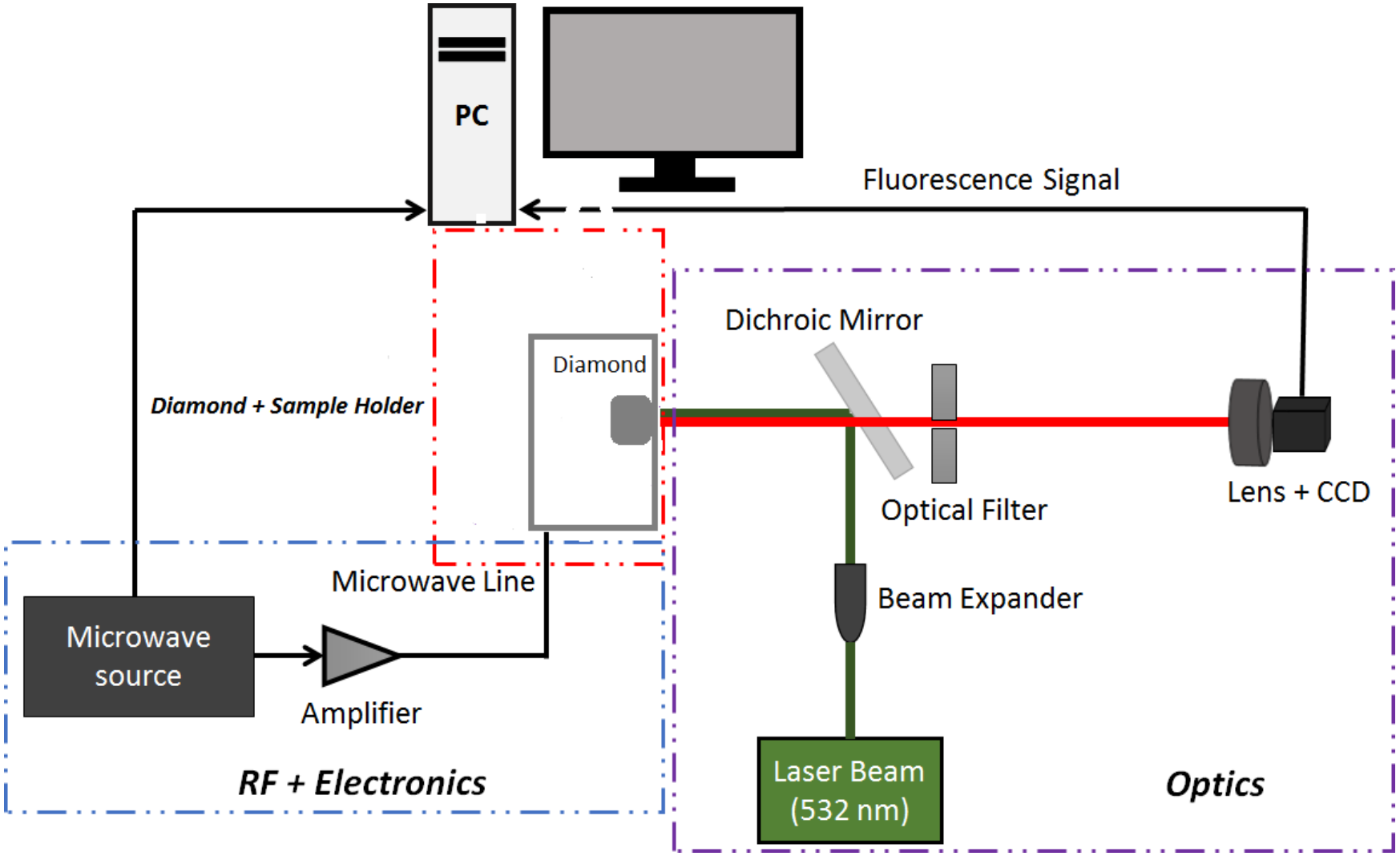

Figure 5.1: A schematic of the experimental design concept with optics, RF electronics, and sensor modules in purple, blue, and red boxes respectively. In the optics module, a green 532 nm laser beam initializes the NV diamond crystal located in the bore of the magnet. A beam expander (BE) placed in the optical path enables the full excitation of NV centres localized in the (001) diamond plane. Emitted fluorescence is transmitted through the dichroic mirror and later filtered by a 595 - 800 nm bandpass filter. Red-fluorescence quantifying the magnitude of magnetic field is collected on a CCD camera. NV defect spin state manipulation is realized by a copper strip placed beneath the diamond sample.

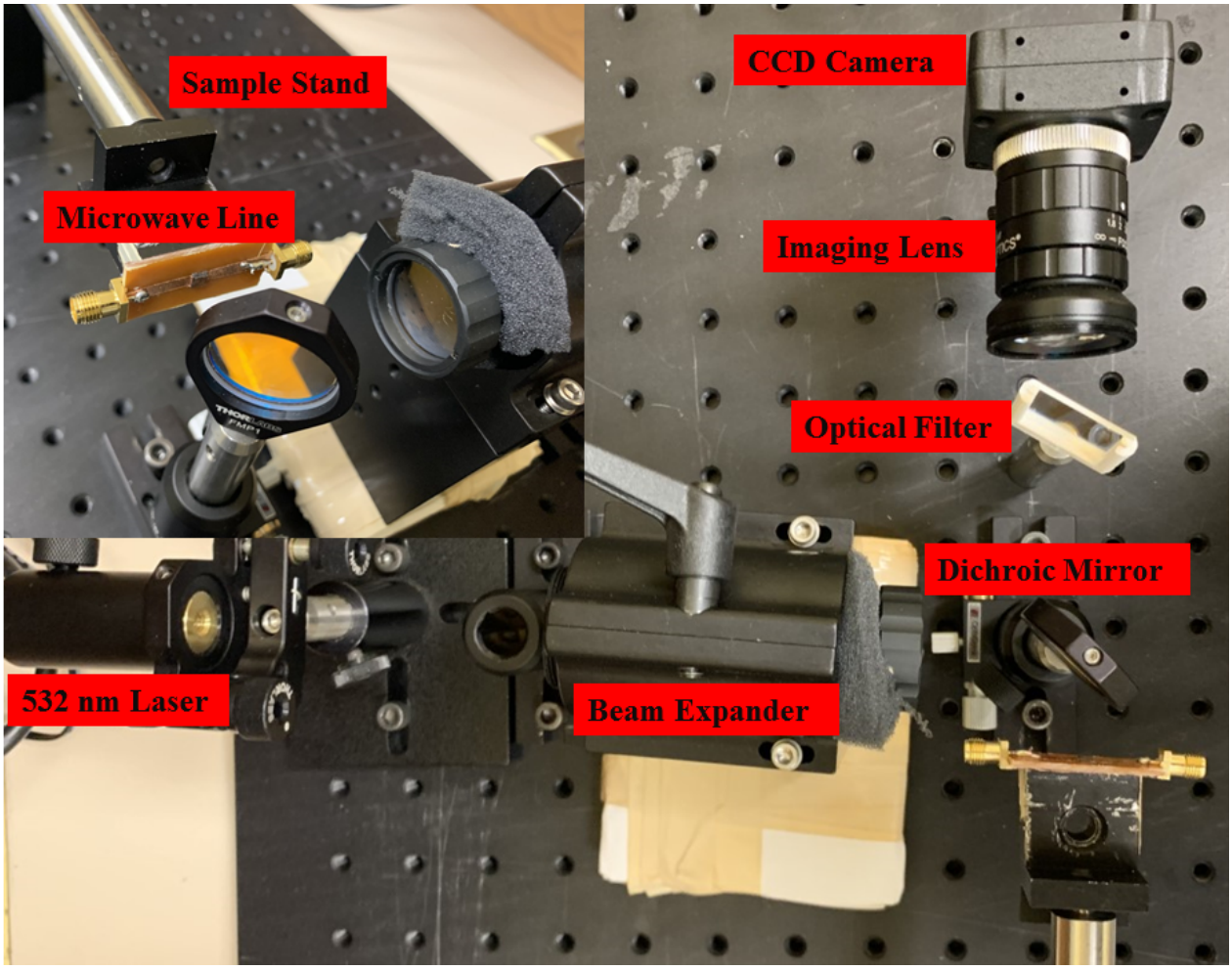

Figure 5.2: Photograph of the experimental design set-up on an optical bench from a top-down view. In the upper left of the image, a zoomed photograph of the dichroic filter at 45° focusing on the diamond sample mounted on a copper line delivering the microwave for NV spin manipulation is shown.

ated with it. Essentially, it was required that the entire (001) diamond plane is uniformly illuminated.

Laser

An ensemble of NV centres was diamond sample is then illuminated with a compact collimated laser-diode-pumped (DPSS), 532 nm laser module (Thorlabs Inc., Montpellier St. Laurent, QC, CA). The laser had a nominal power of about 4.5 mW and was surrounded by a Ø11 mm housing case. A 5 VDC regulated power supply, with a 6 ft cable and a 2.5 mm phono plug extending from the body of the power supply was used to power the laser. The ODMR technique utilized in this thesis is dependent on detecting relatively small changes in the fluorescence intensity [94], it is therefore required that the excitation laser was sufficiently stable at least during the period of measurement ($<$ 3 % RMS).

Beam Expander

The laser interfaces the BE (Edmund Optics Inc., Barrington, NJ, USA) which increases the diameter of the input beam into a larger output beam[1]. Modern-day laser BEs are afocal systems, meaning object rays enter parallel to the optical axis and exit parallel to them. The use of the BE is of importance in this design because they reduce beam power density and irradiance (diverging beam over large areas other than concentrating at a point); such reduction can increase the lifetime of laser components, and most importantly reduce laser-induced damage. A fixed magnification BE with 3X expansion power in the wavelength range between 500 - 570 nm with an entrance aperture of 10 mm, and an exit aperture of 23 mm was used in this design. To calculate the beam diameter at a distance L, the following Equation [218] was used:

$$D_L = (M_P + D_I) + L \cdot \tan\left(\frac{2\theta_I}{M_P}\right) \tag{5.5}$$

[1]The author acknowledges Doug Miller for the discussion on the use of the BE.

Table 5.1: Detector components specification and descriptions.

Component	Part	Description
Laser	CPS532	Collimated Laser-Diode-Pumped (DPSS) module; 532 nm wavelength; 4.5 mW power; Round beam.
DC power supply [a]	LDS5	5 VDC regulated power supply; 2.5 mm phone plug; 120 VAC.
Dichroic Mirror	DMLP567	Wavelength range is 584 - 700 nm; cut-off wavelength is 567 nm; angle of incidence is 45^o.
Optical Filter	PN-FDM000002	Reflect band range: 533 - 580 nm; Passband range: 595 - 800 nm.
Beam Expander	DA 35-098	Design wavelength is 532 nm; Expansion power 3X; Wavelength 500-570 nm.
Microwave Source	LMS7002M MIMO FPRF	Memory: 256 MBytes DDR2 SDRAM; USB 3.0 controller; Cypress USB 3.0 CYUSB3014-BZXC.
Power Amplifier	MPA-2-6G	Frequency range: 2000 - 6000 MHz; 1 Watt (30+ dBm) output RF Power Amplifier;28 VDC power supply.
CCD Camera	CMLN-13S2C-CS	1.3MP Color Chameleon USB 2.0; Camera 1/3" CCD CS-Mount [CE].
Imaging Lens	33-307	8 mm C series fixed focal length lens; C-Mount.
DC Power Supply[b]	NPS-1602	Generic Gophert: 0 - 60 V; 0 - 3 A; 180 W switching digital adjustable DC power supply.

[a]Power supply for the laser beam.
[b]Power supply for the amplifier.

Table 5.2: Detector components with a list of vendors and websites.

Component	Vendor	URL
Laser	Thorlabs	www.thorlabs.com
DC power supply	Thorlabs	www.thorlabs.com
Dichroic Mirror	Thorlabs	www.thorlabs.com
Optical Filter	Iridian Spectral Technologies	www.iridian.ca
Beam Expander	Edmund Optics	www.edmundoptics.com
Microwave Source	CROWDSUPPLY	www.limemicro.com
Power Amplifier	RFBay	www.rfbayinc.com
CCD Camera	FLIR	www.flir.ca
Imaging Lens	Edmund Optics	www.edmundoptics.com
DC Power Supply	-	www.amazon.ca

where L is the working distance, θ_I is the input beam divergence, M_P is the beam expander magnifying power, and D_I is the input beam diameter. All working distances and diameters here are measured in mm, while the input beam divergence is measured in radians. For the DPSS laser used, the input beam diameter was less than 2 mm and the input beam divergence was less than 1 mrad. The output beam diameter obtained was approximately 4.50 mm at an optimized distance L, thus satisfying the 3 mm $\times$ 3 mm sample area illumination needed.

Dichroic Mirror and Long Pass Filter

The long pass dichroic mirror (DMLP567) with a cut-on wavelength of 567 nm (Thorlabs Inc., Montpellier St. Laurent, QC, CA) placed at 45° reflects green light and transmits red. As shown in Figure 5.3, the mirror has a guaranteed transmission band from 584 - 800 nm; in this band, the average transmittance of the mirror is $T_{avg} > 90\%$. Also, the mirror has a guaranteed reflectance band in the range 380 - 550 nm with an average reflectance value $R_{avg} > 95\%$. Emitted red fluorescence from the diamond sample passes through the dichroic mirror and was filtered by a bandpass filter (Iridian Spectral Technologies, Ottawa, ON, CA)

in the wavelength range 595 - 800 nm. Every optical component in the detection path causes some form of intensity loss in the system. In particular, filters used in the optical system result in the largest intensity losses [219]. Filters are of three types: (i) interference filters made from transparent optics coated with several dielectric layers, (ii) hybrids made from absorbing optical flats coated with dielectric layers, and (iii) those from absorbing/coloured glass [220]. The dichroic filters used in this design are of the interference type. Specifications of the most suitable filter depend on the laser line used. Ideally, a dichroic filter incident at 45^0 with up to 80% transmission is required. For the bandpass filter, a transmission efficiency of 50 - 90% is highly desired - this requirement is met with the optical filters chosen.

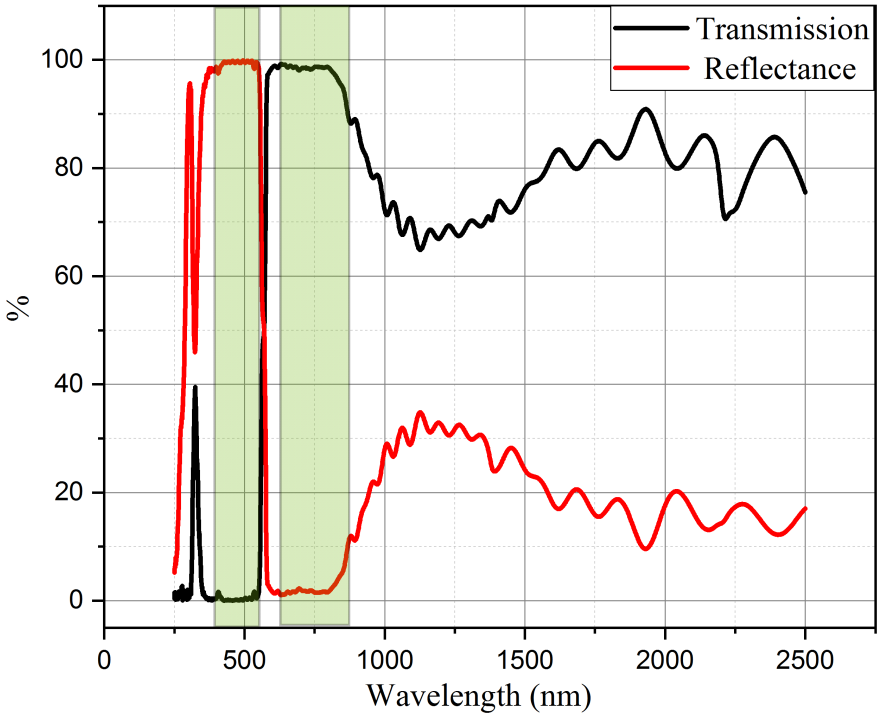

Figure 5.3: A graph showing the transmission and reflectance band in % of a DMLP567 dichroic mirror. The mirror has a transmission band from 584 - 800 nm and a reflectance band in the range 380 - 550 nm. The data plotted was adapted from `www.thorlabs.com`

Charged Coupled Device (CCD) and Imaging Lens

The emitted fluorescence is afterwards collected with a 3MP coloured Chameleon USB 2.0 camera (FLIR, Vancouver, BC, CA) with an imaging lens in the collection path. The design

employs a flat (2D) charge-coupled device (CCD) detector which gives a focus when the target falls within the depth of field of the lens. The sensor of the camera is a Sony ICX445, 1/3" CCD with 1296 x 964 resolution and a maximum frame rate of 18 frames per second (FPS). Although the camera has an exposure range of 0.01 ms to 10 seconds, it will be seen later that the exposure time also depends on the memory capacity of the computer used for read-out. The custom image settings used for fluorescence frame collection are shown in Figure 5.4.

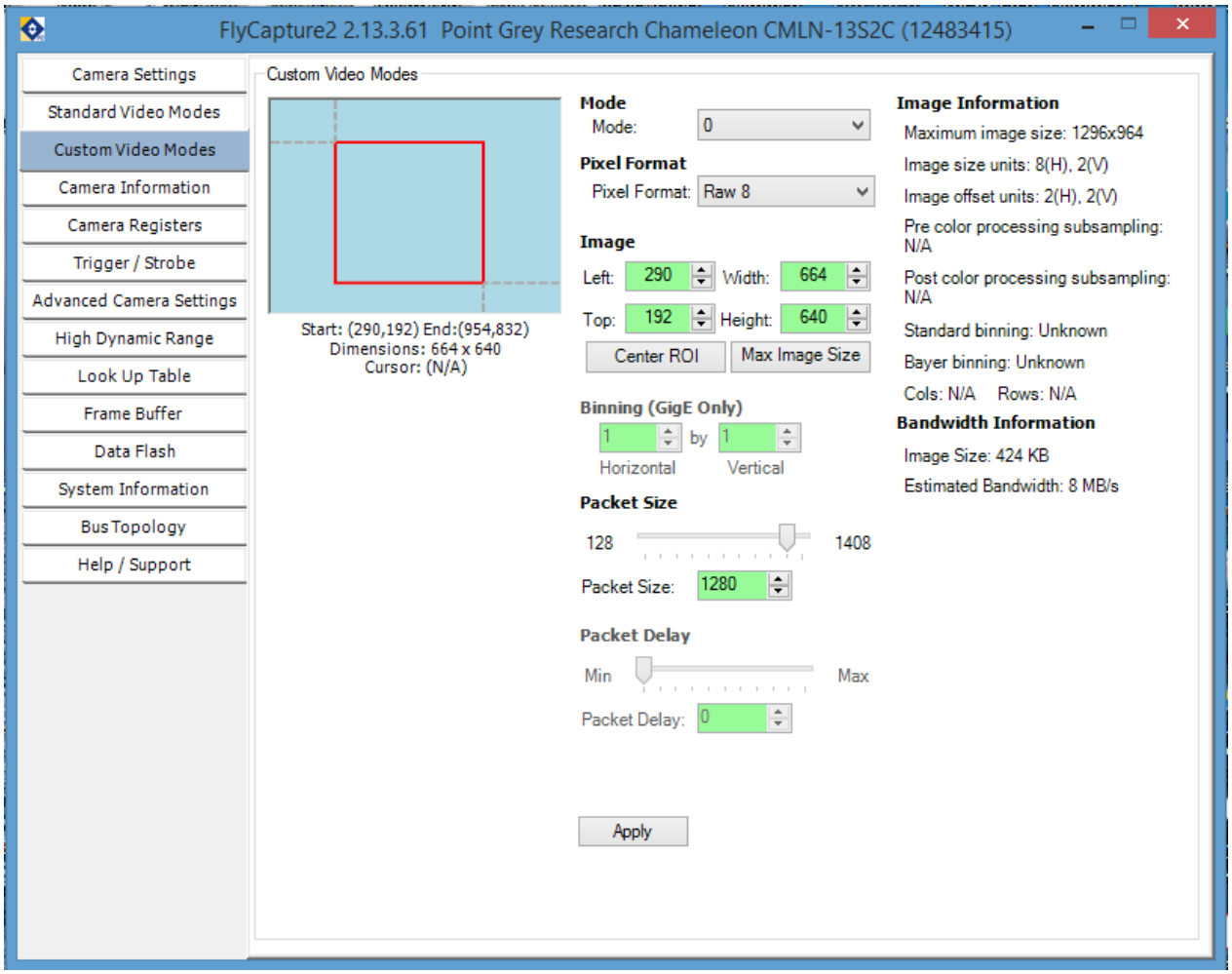

Figure 5.4: Custom image settings on the camera for collecting fluorescence frames.

In selecting an imaging lens for the CCD camera, several factors including the optical working distance, FOV, and cost were considered. Of the three metrics mentioned, the FOV is important to maximize the potential spatial resolution of the detector setup. Table 5.3 presents details of camera lenses considered with a FOV vs. price tradeoff table. The imaging lens chosen for this design had a focal length of 8.50 mm and a working distance of 100 - ∞ mm. With a 1/3" CCD sensor format, the horizontal, vertical, and diagonal FOV were 59.1 mm, 43.4 mm, and 76 mm respectively. Although 3D information cannot be obtained from this configuration, the blurred out-of-field target depth still contributes to the intensity obtained from the detector. Another difference between the proposed system and a confocal system is the ability of a confocal system to obtain 3D information by sacrificing the area of view. By collecting signals exclusively from a single illuminated point at a time, lateral and axial resolution is enhanced in the confocal system compared to the system described here. The efficiency in the illumination and detection path is often not of great importance in this design, as lost emission can be easily compensated for by shortening the collection path (L) and increasing the detector's integration time. To improve the detection efficiency, our proposed system has few optical elements in the detection path to avoid losses due to reflection or absorption [221]. Annular apertures were also avoided in this setup because they obscure large fractions of fluorescence light and reduces detectability limits by increasing Poisson noise [222, 223].

5.3.2 Microwave + Electronics

For manipulating NV spins in the diamond sample and recording ODMR spectra, microwave frequency in the GHz range was transmitted using a low-cost SDR operated in transmit (TX) mode driven with open-source GNU Radio software. The SDR was a LimeSDR (CROWD-SUPPLY, Guildford, Surrey, UK) operated in a continuous frequency range 100 kHz – 3.8 GHz with a bandwidth of 61.44 MHz. To take advantage of the wide-area illumination on the diamond sample, a feasible idea was to deliver the microwave line using a double-sided copper tape soldered to an SMA connector attached to the back of the diamond sample. The S11 parameter obtained from using this approach was about 3.88 dB which means about

Table 5.3: Detailed characteristics of the different imaging cameras considered. In considering a camera, the FOV Vs. price tradeoff as tabulated here was considered as the main metric.

Lens	**Minimum WD[a] (mm)**	**FOV[b] (mm)**	Price ($)	Specification Sheet
0 - ∞ @ F = 4 mm	0	16.1[c]	210	https://www.edmundoptics.com/p/4mm-uc-series-fixed-focal-length-lens/2966/
[d]50 - ∞ @ F = 8 mm	50	21.7	210	https://www.edmundoptics.com/p/8mm-uc-series-fixed-focal-length-lens/41864/
[d]75 - ∞ @ F = 8 mm	75	21.7	210	https://www.edmundoptics.com/p/8mm-uc-series-fixed-focal-length-lens/41864/
100 - ∞ @ F = 25 mm	100	19.0[c]	320	https://www.edmundoptics.com/p/25mm-c-series-fixed-focal-length-lens/16528/
500 - ∞ @ F = 100 mm	50	4.38	895	https://www.edmundoptics.com/p/100mm-ca-series-fixed-focal-length-lens/40814/

[a]WD is the working distance
[b]This is the FOV at 100 mm working distance
[c]Horizontal FOV on standard 4:3 sensor format
[d]The imaging lens would work for both working distance

50% power is reflected and 50% power entered the antenna. To detect B_0 fields using the ODMR approach, a microwave frequency sweep from 2.70 GHz through about 3.10 GHz is required depending on the strength of the field to be detected. The transmit power of the LimeSDR within this range was $\leq$ 2.31 dBm and was insufficient to fully resolve an ODMR spectrum. One problem using the LimeSDR as a microwave generator was that the transmit power at the frequency of interest was barely sufficient for microwave manipulation. Typical microwave power needed for adequate excitation is $\geq$ 10 dBm [224, 217, 225]. To bump up the power, an amplifier is needed. In choosing an amplifier, the P1 power is considered; this is defined as the output level at which the power has deviated from true linearity by 1 dB [226]. All classes of amplifiers have a P1 point as it is the most useful reference to output power and can be measured directly. Beyond the P1 point, an amplifier goes into compression as input power is increased. Therefore, if the desired power of about 30 - 35 dBm is needed, an amplifier having a P1 point of 10 dBm or more is needed. For amplification, an MPA series +30 dBm RF power amplifier (RFBAY Inc., Gaithersburg, MD, USA) in the frequency range 2000 - 6000 MHz with a gain of 33 dB was used. The amplifier was powered with a generic Gophert, 0 - 60 V, 0 - 3 A, and 110 V/220 V adjustable DC power supper supply. By using this amplifier for power boost, a 30% increase in the S11 parameter was obtained.

To transmit microwave frequency using the LimeSDR, we employed the use of an open-source GNU Radio software (`www.gnuradio.org`) interfaced with a simple python script(`www.python.org`) by connecting modular signal processing components into a flow graph to obtain frequency sweep functionality. Primarily, SDRs typically comprise analog-to-digital and digital-to-analog converters, signal down and upconverters, field-programmable gate array (FPGA), and a USB interface [227]. Figure 5.5 shows the software architecture and implementation package consisting of a python script and several C++ based GNU Radio flowgraph elements of the CW microwave transmitter. A GNU Radio flowgraph consists of a signal generator, signal processing, input and output blocks connected by virtual wires. Wires conduct signals in the direction indicated by the arrows. The flow graph in Figure 5.5 comprises a cosine waveform sent out in packets at a 10^6 sample rate with random noise

generated in the mix. The addition of the signal and noise source generated were then passed onto the LimeSDR for output. A python module containing a script to automate the microwave frequency sweep is included in the flow graph. In addition, a function probe with a poll rate of 1 Hz was introduced into the architecture to generate an exact timing for the microwave sweep.

5.4 Methods

Fluorescence maps obtained from the optical design were processed sequentially as diagrammatically shown in Figure 5.6. Optical excitation is first achieved using a 532 nm laser set to wide-area illumination with the aid of a BE as shown in Figure 5.6(a). The resulting two-dimensional fluorescence is projected onto a 1296×964 pixel CCD camera detecting the entire image with an integration time of 100 ms. For each laser illumination power, camera frames were appended to the computer memory to form a 3D volume of data giving the value of luminescence for each pixel (x,y) of the camera at each laser power (P) as shown in Figure 5.6(b). Subsequently, the CCD fluorescence frames obtained were corrected for dark current, bias, and sensitivity-related errors as shown in Figure 5.6(c),(d), and (e). In an ideal situation, the number of electrons collected in a pixel during exposure is proportional to the number of photons emitted from the NV diamond sensor. However, in practice, the number is impacted by thermal agitation in the pixel amidst other factors.

Furthermore, the number of electrons produced by the NV photons is dependent on the sensitivity of the camera's pixel to incident photons - mostly due to the efficiency of the optical system to deliver photons to various locations on the camera's chip. Depending on the temperature of the CCD chip, dark current fills each pixel with electrons at a steady rate. The total number of electrons contributed by the dark current depends on the temperature of the chip and the integration time. By standard practice, dark current is corrected by subtracting an image that contains only the dark current contribution to the main image (taken with the camera's shutter closed). The image to be subtracted is captured at the same CCD temperature, and integration time as the main image.

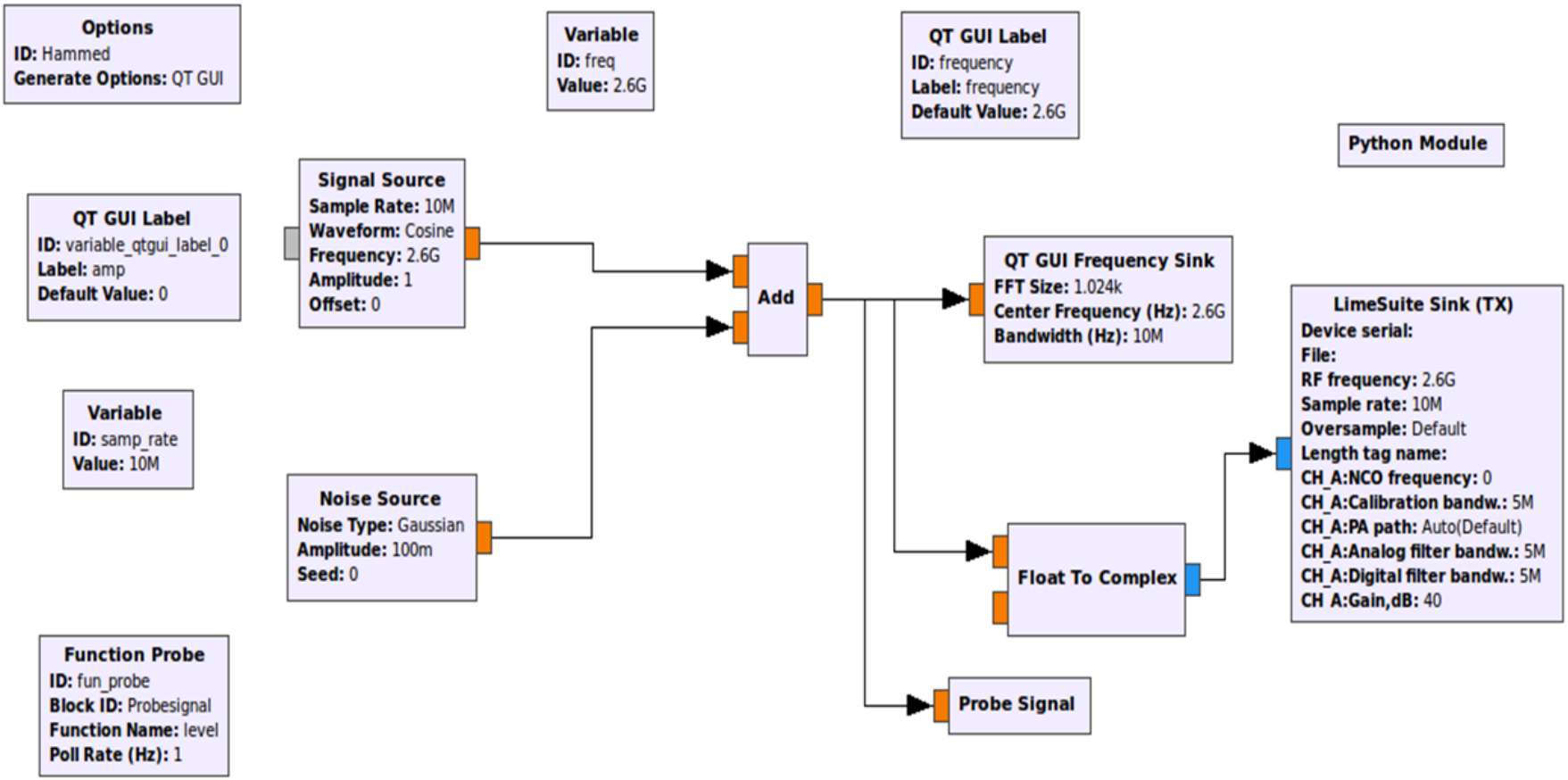

Figure 5.5: Software implementation of a CW microwave transmitter in GNU Radio. The implementation flowgraph is made up of a signal source with continuous cosine wave output. To mimic an ideal situation a random noise source was introduced with the addition of both sources fed into the LimeSDR for transmission. A python script was included in this implementation to automatically sweep frequencies from 2.6 GHz to 3.10 GHz.

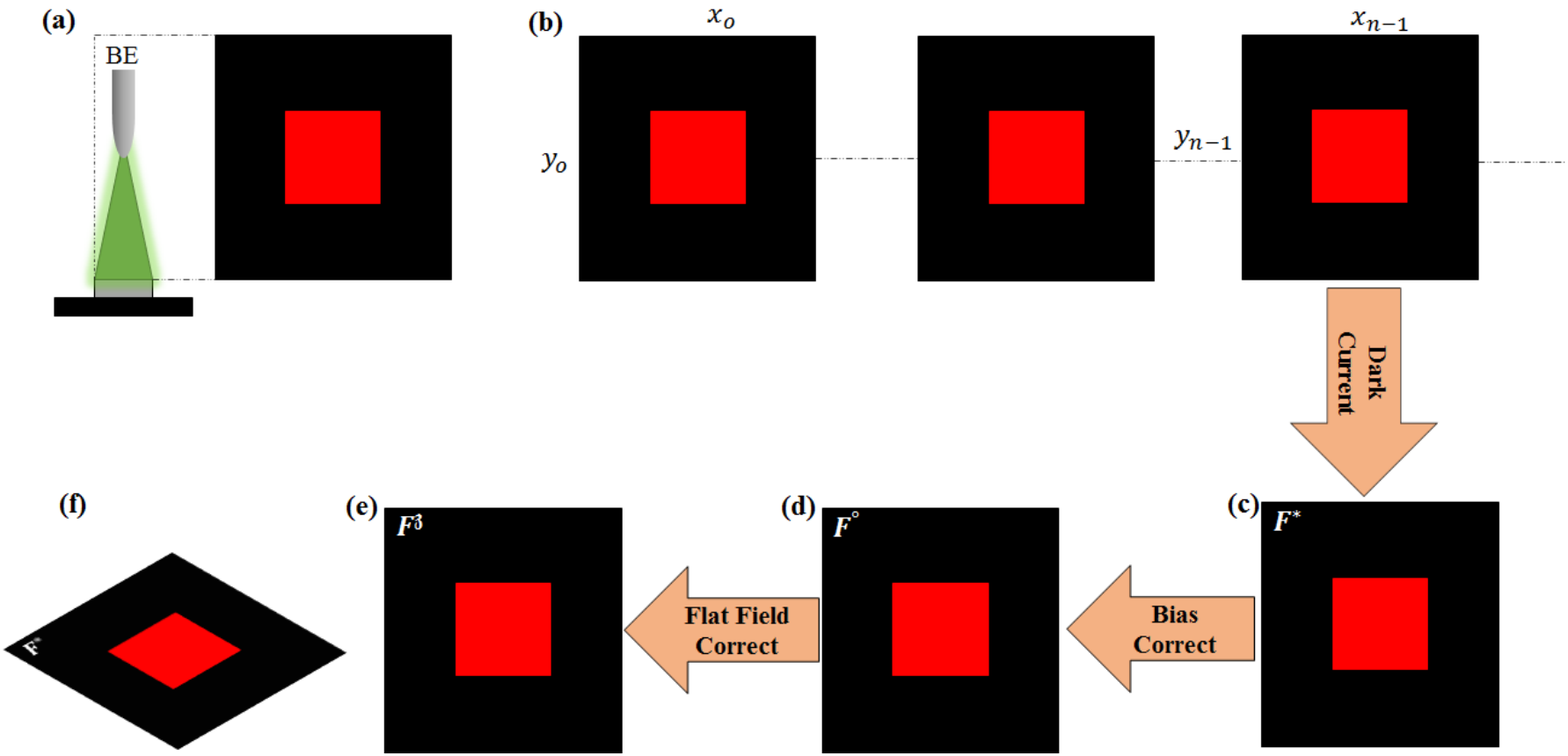

Figure 5.6: A summary of the process of the image corrections applied to the recorded camera frames. (a) Sample geometry of the full excitation of the diamond achieved with the aid of a BE (b) Camera frames recorded on a 1296 × 964 pixel camera detecting the entire diamond sample with an exposure time of 100 ms at different excitation laser power (c) All frames were corrected for dark current by subtracting an image that contains only the dark current contribution to the main image. (d) Subsequent frames were corrected for any bias. (e) Flat field corrections were carried out on the latter frames to correct for sensitivity and the final image obtained was characterized.

When a camera reads the data on a sensor, it generates a small amount of noise added to the value of the image recorded. Bias correction removes grid noise generated by the camera as it hits the pixel when photons hit the sensor. Correcting for bias error is made by subtracting a separate dark image taken at the fastest exposure time of the camera. Lastly, the CCD chips are not equally sensitive to light across the surface, flat field corrections account for the sensitivity variations across the chip. A flat field is taken with the camera surface exposed to a flat equally illuminated view in the linear exposure range of the camera.

To characterize the fluorescence emission performance of the new system described in this chapter, the SNR of the system was analyzed and compared with a traditional confocal system schematically shown in Figure 5.7. A spot size of about 6 mm^2 on the diamond sample is illuminated with the aid of an aspheric lens L2, (Thorlabs Inc., Montpellier St. Laurent, QC, CA). The same lens collects and directs red fluorescence obtained from the sample to a convex lens L1 placed in the optical path to suppress background fluorescence from the green light. The lens L1 is also used in this setup to focus collected light onto the camera. For averaging, each fluorescence intensity was obtained 5 times from the set-ups. The camera frames were again passed through the same processing cycle in Figure 5.5. It must be mentioned that the setup described in Figure 5.7 is common in the NV centre community.

5.5 Results and discussion

5.5.1 Performance comparison

As highlighted in the design requirement section of this chapter, detection efficiency and emission light performance are metrics influencing the sensitivity of the new NV sensor system. Results obtained from optical systems including ours must pass through high-resolution information and fluorescence intensity evaluation. For resolution measurements, it is standard to measure the FWHM of bright and well-separated fluorescent point sources. An alternative is by using two rather dim sources (Rayleigh criterion [228, 229]). Nevertheless, since the

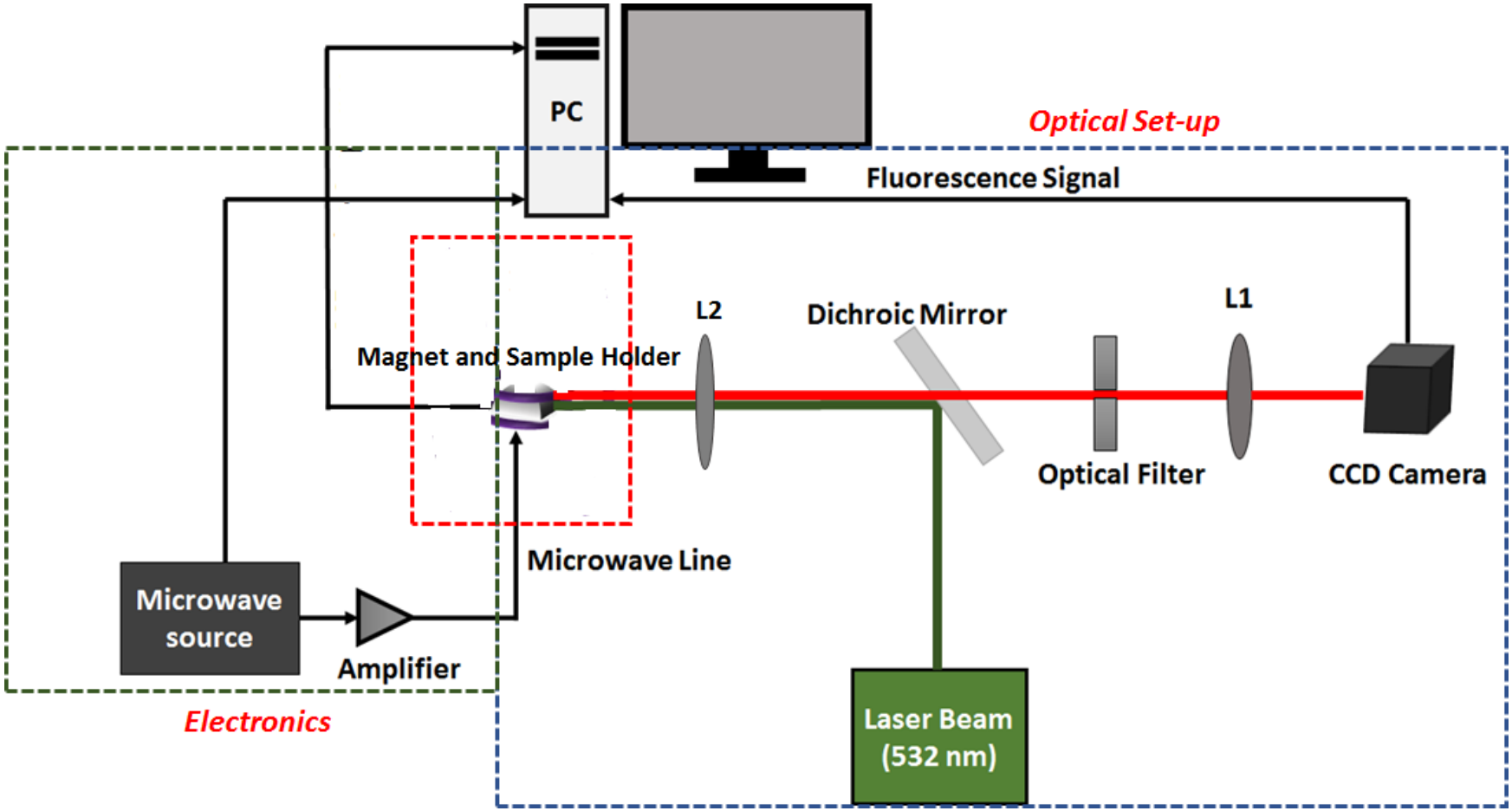

Figure 5.7: Schematic of a home-built confocal microscope built for assessing the performance of the new NV sensor system design. The 532 nm laser beam focused at a spot with the aid of the aspheric lens L2 initializes the NV diamond crystal located in the bore of the magnet, red-fluorescence quantifying the magnitude of magnetic field is collected on a CCD camera via the same focusing element.

system here was not yet intended for a magnetic imaging application, it was essential to confirm that the output of the sensor is sensitive enough for an eventual imaging application (having a reasonable signal that is suitably distinguishable from noise i.e high SNR). Having SNR information of a detector give valuable information on the sensitivity of the system. Central elements in the optical path contributing to SNR are the optical laser source and the detector. The laser source because it accounts for the fluorescence intensity emitted from the NV centre and the detector as it places a fundamental limit on the SNR. Additionally, for the given signal within a specific region-of-interest (ROI) to be detectable it needs to be greater in intensity than the background, hence the SBR. Work by Ferrand et al. 2019 [230] extensively analyzed the image quality in a confocal microscope setting using NoiSee workflow. A different approach was taken in this chapter by using the SBR/SNR metric to compare the emission light performance of our design and the confocal set-up under different optical excitation conditions.

First, it is necessary to identify the different optical power regimes for the optical system. The saturation regime (the region where the NV detector starts to give a non-linear response) was distinguished from the undersaturated regime (regions of low laser power that minimizes photobleaching of the NV centres) by carrying out a comparative power-dependent excitation. The fluorescence saturation curves in CW laser excitation were collected to characterize the influence of laser power on the spontaneous emission rate of the fluorescence NV centre as shown in Figure 5.8. The excitation power was varied with the use of a neutral density (ND) filters of varying optical densities. Using ND filters of optical densities 0.3, 0.5, 0.8, 1.0, and 2.0, laser powers of approximately 2.25 mW, 1.44 mW, 0.72 mW, 0.45 mW, and 45 μW were obtained respectively. The fluorescence intensity was obtained from both setups in the presence and absence of backgrounds. Larger fluorescence intensities were obtained when background signals weren't subtracted. In addition, an increase in the fluorescence intensity was observed in the confocal microscope set-up indicating the likelihood for a better SNR when compared to new the set-up. Saturation effects take place with increasing optical power. The approximate optical saturation power for both designs is about 2.1 ± 0.3

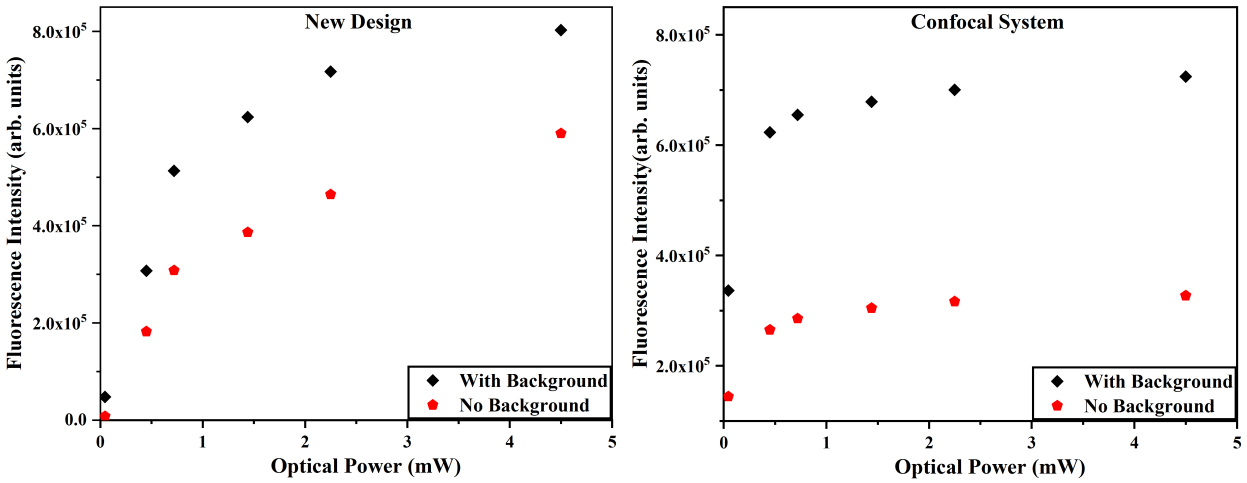

Figure 5.8: Fluorescence saturation plot comparison (a) saturation plot obtained by integrating fluorescence in the red region for our new design (b) saturation plot obtained by integrating fluorescence in the red region for the confocal system set-up. In both designs, optical saturation power is approximately 2.1 ± 0.3 mW.

mW. This result indicates that optical excitation below the 2.1 ± 0.3 mW range is in the undersaturation regime while optical excitation above is in the saturation region.

To have comparable performance measurements between the optical designs, several parameters needed to be set. First, the diamond NV sensor needed to be illuminated with fixed laser power and in the same area. This was achieved in the new design by completely illuminating the entire diamond sample with the unwanted background signal being suppressed by a bandpass filter. In the confocal system, emitted fluorescence was collected with an aspheric lens used for excitation. All emissions were collected then the entire region-of-interest (ROI) corresponding to the approximate area where the fluorescence is dispersed on the sample for analysis was selected on the CCD image - it should be mentioned that the method isn't an ideal confocal set-up but it allows for fair comparison. Further, the camera exposure, integration time, and collection path must be kept constant between the two set-ups. In addition to all these, the frame size in the CCD software was kept constant for comparability. In the measurement of SBR, background/dark current variability may exist, for this reason, 20 different dark current averages were collected to ensure we have a good account of the

background variability.

Emission light performance was compared at four varying optical powers corresponding to the saturation and undersaturation laser regions. Figure 5.9 shows the fluorescence maps acquired for both design set-ups. It is important to mention that maps presented for comparison were acquired using the same conditions - laser optical power, integration time, and collection distance (L). Fluorescence maps were collected at different optical excitation powers to ensure the capability of the sensor was tested under different CCD detection ranges, thus maps were collected at saturation and just below saturation. Figure 5.9 (a,b,c,d) represents fluorescence maps obtained from our design, while Figure 5.9 (e,f,g,h) are fluorescence maps obtained from the confocal system set-up (only a selected ROI was considered here). A trusted comparison metric for an optical sensor of this kind is the SNR/SBR and these calculations were carried out with a macro developed in Fiji software. At varying laser power, 5 repeated measurements were made to allow for averaging.

Table 5.4 summarizes the results obtained from the two different sensor designs at varying optical power. From the table, it is evident that the conventional confocal set-up outperforms our new design in terms of SNR at both saturation and undersaturation optical power regions. This is in agreement with what was observed earlier in the intensity vs. optical power curve in Figure 5.8. The higher SNR of the confocal system was expected and comes as a result of the extra background noise suppression mechanism employed [231]. In a confocal setting, most of the out-of-focus light is obstructed using a pin-hole, thus limiting the intensity of the background. In the optical power saturation region, the SNR and SBR of both designs are comparable, while in the undersaturation power region, the confocal system greatly outperforms the new design in terms of SNR and SBR. The confocal system shows higher SBR in the undersaturation excitation region when compared to our newly designed system. This is partly because low background intensity hence lower noise value is obtained in the undersaturation region, therefore, resulting in a higher SBR. In the new design, a slight decrease in the SBR value is observed as the laser intensity increases - the result is expected

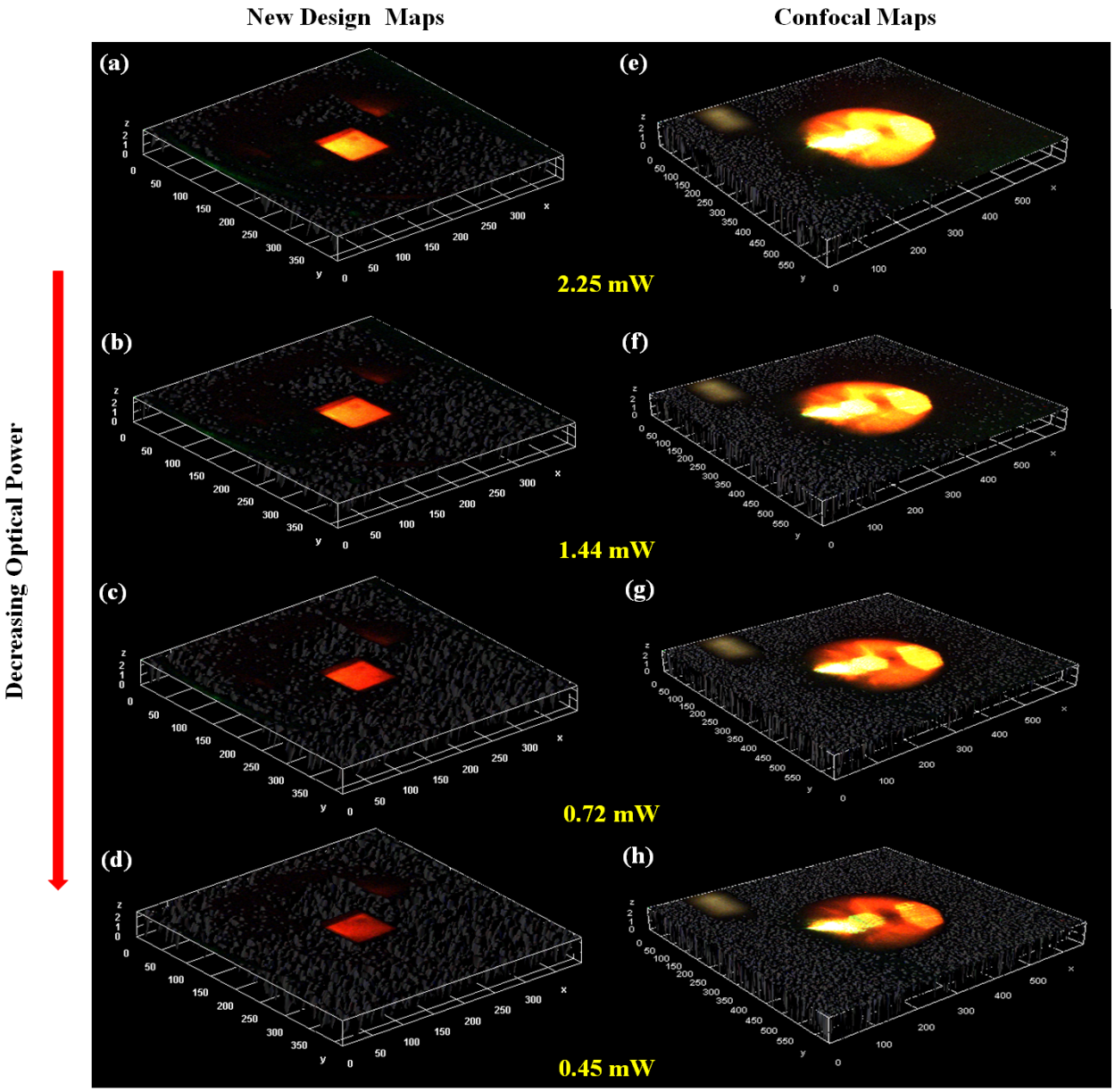

Figure 5.9: Fluorescence maps as a function of decreasing laser power from top to bottom. Figure 5.9 (**a,b,c,d**) represents fluorescence maps obtained from our design. Figure 5.9 (**e,f,g,h**) are fluorescence maps obtained from the confocal system set-up.

Table 5.4: Results from analysis at different sensor design and varying laser optical power

	New Design				
	Signal Mean	Background Mean	Background Standard Deviation	SBR [a]Mean	SNR [b]Mean
Power (mW)					
2.25	199.10	15.09	14.39	13.19	12.78
1.44	173.80	13.46	10.43	12.90	15.40
0.72	145.50	11.84	6.95	12.30	19.25
0.45	91.10	7.70	2.73	11.87	30.63
	Confocal Set-up				
	Signal Mean	Background Mean	Background Standard Deviation	SBR [a]Mean	SNR [b]Mean
Power (mW)					
2.25	254.64	18.32	14.47	13.90	16.33
1.44	254.14	13.44	10.78	18.91	22.33
0.72	252.79	9.64	7.46	26.22	32.61
0.45	250.45	7.00	4.27	35.80	57.10

[a] Signal-to-background ratio (SBR) = $\frac{\text{Signal Mean}}{\text{Background Mean}}$

[b] Signal-to-noise ratio (SNR) = $\frac{\text{Signal Mean}-\text{Mean Background}}{\text{Background Standard Deviation}}$

because there are no means for additional background suppression other than the bandpass filter used. Results from background analysis reveal a slight difference in the background averages of both methods implying that both designs were at least optimized for background noise. The high value of the standard deviation of the background may indicate a mechanical or electronic defect on the CCD detection side [230]. In contrast to the mean SBR of the confocal system which increases at decreasing optical power, the SBR of our design decreases with a decrease in optical power. In the low optical power region, our proposed design shows almost the same changes in the background intensity as the confocal system. Further, the mean signal in the confocal system is about 1.5 times that of our set-up, as a consequence resulting in a better SNR for the confocal system. The implication of these results is that the utmost performance of our system is guaranteed in the undersaturation region (region of low power excitation) and thus our design system excitation is best utilized in this region.

To ensure the repeatability of measurements in Table 5.4. Measurements were again collected at two minute intervals while varying the optical power of the laser. For each measurement, four different frames were collected. Two minutes was considered an appropriate interval in order to avoid long spacing in measurements and to avoid photobleaching and a reduction in laser intensity. Figure 5.10 shows the result of the measurement. For the given time interval there was no significant difference between the measurements made both for SBR and SNR hence validating the repeatability of the measurements under the same conditions. In the new design proposed, SNRs were generally constant when compared to their SBR. On the contrary, the confocal system exhibits a fairly constant SBR and SNR indicating that there were no changes in the background which constitute about 2% of the overall intensity measured from the system [230]. Slight fluctuations in the intensity measurement can be attributed to laser power fluctuations - this is a topic for discussion in chapter 6.

5.5.2 Power consumption

An analysis of the total power consumption in the new system is presented in Figure 5.11, this was done to ensure that the system meets the required power specification. From the

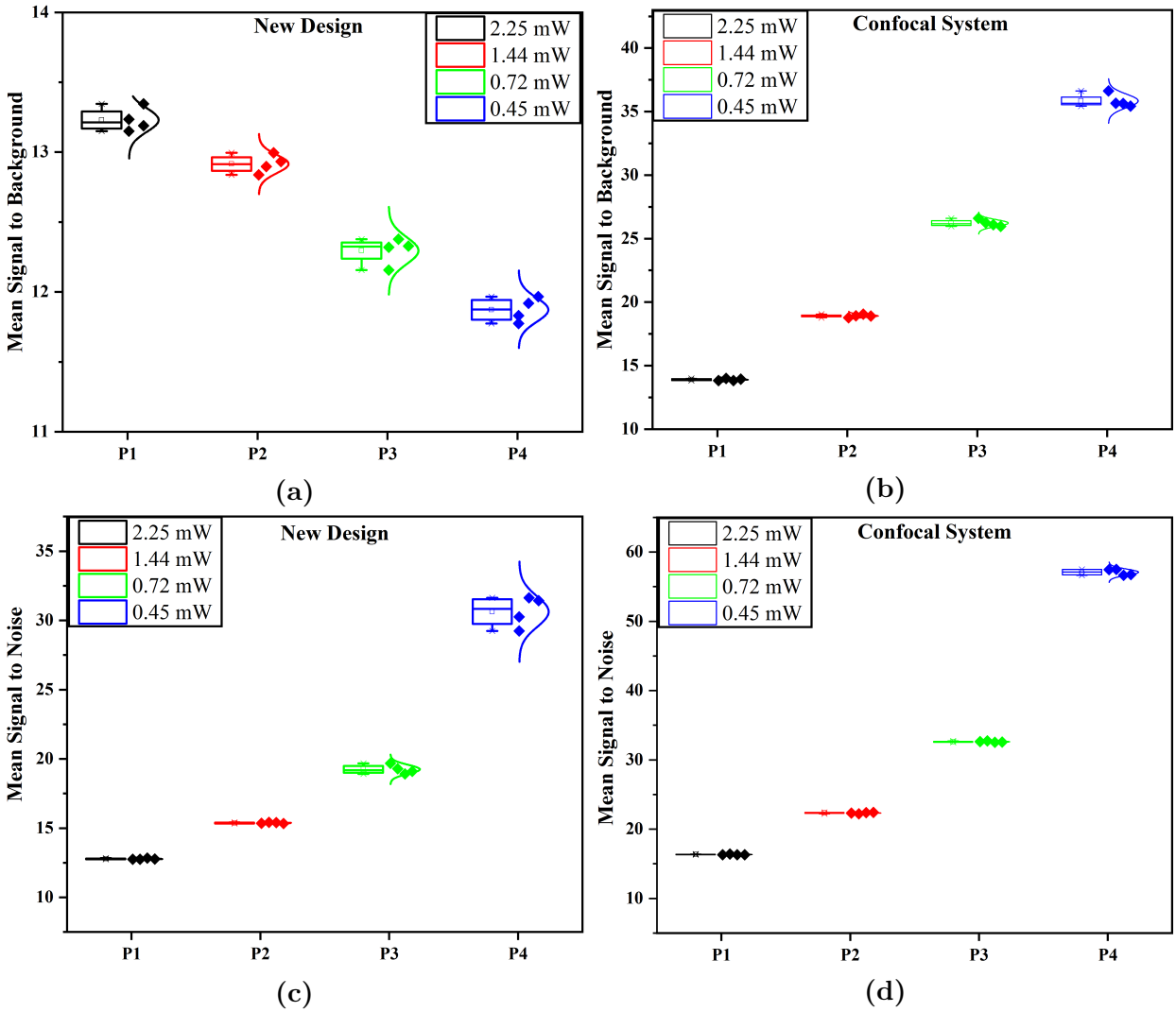

Figure 5.10: Repeated measurements showing reliability of the adopted method. The distribution of SBR and SNR under varying optical power is shown in a box and whiskers plot. (a),(b) SBR comparison of the two designs under different optical powers (2.25 mW in black, 1.44 mW in red, 0.72 mW in green, and 0.45 mW in blue) collected with a 2 minute interval between each measurement. (c),(d) SNR comparison of the two designs under different optical powers (2.25 mW in black, 1.44 mW in red, 0.72 mW in green, and 0.45 mW in blue) collected in 2 minutes interval between each measurement.

graphical representation in Figure 5.11, the total power consumption of the system is estimated as 107 dBm. 30 dBm of the power consumed is attributed to the microwave source used in driving the circuit, 16.5 dBm is from the laser source, 26.5 dBm is due to the CCD camera used, and the rest due to the power consumed by electronic circuits. All electronic components not powered by a DC supply were USB powered. Most computer USB ports supply 5 V of electricity with a maximum current of 0.5 A bringing the overall maximum power output for the electronics to about 33 dBm. The total power consumption seems to be in a fair range of what is obtainable in an optics laboratory setting. Nonetheless, for compact applications, there is a need to reduce power consumption requirements. Power requirement is mostly limited by available resources and technology. Essentially, we seek minimal power requirements at the expense of the design's sensitivity. For this reason, a further miniaturized model of the design presented in this chapter with a lesser power consumption requirement is proposed. The proposed conceptual scalable design will make use of cheaper off-the-shelf optical and 3D printed components.

A schematic overview of the proposed sensor is shown in Figure 5.11. We anticipate the total construction volume of the 3D model to be about 88 cm^2, as a result, it is possible for the device to be handheld. All components are arranged in a multilayer design in a cylindrical like structure shown in Figure 5.11. The main elements in the design are the LED (A) functioning as the green light source, glass lens double concave mirror acting as a BE (D), a distributed Bragg reflector (E) placed between the BE and the diamond sample to reflect fluorescence red light. The diamond sample is placed on a red glass (G) serving as a sample stage and also allowing transmitted fluorescence to be collected on the photo-detector (H). B is the casing of the hand held detector, C and C^* are the inside lining material of the detector. Lastly, F is the diamond sample containing NV centres to be excited. It must be mentioned that the present design uses an external power supply and microwave manipulation source. Possibilities for expansion also exist, for example, the stage can accommodate more than one diamond sample and the double concave lens can be combined in situations where multi-sensors (multiple diamond samples) need to be excited. Although the light emission

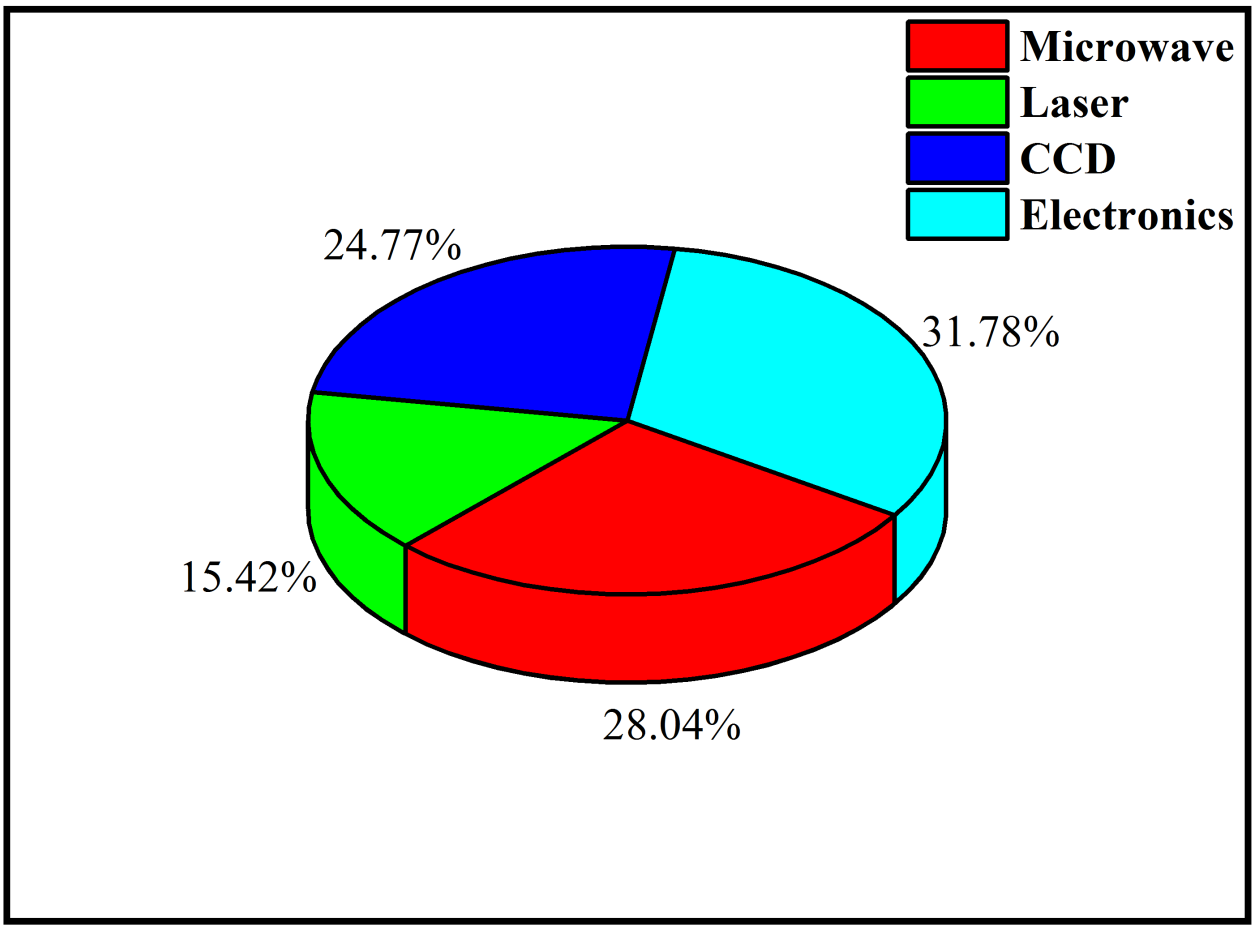

Figure 5.11: Power consumption of the new sensor. Total power consumption is estimated as 107 dBm. Approximately 28% of the total power is estimated to be used by the microwave source used in driving the circuit, 15.4% is due to the laser source used for optical excitation, 24.8% from the camera source used for detection, and the remaining 32% from the electronics used in driving-related circuits.

performance of the proposed scalable NV sensors hasn't been tested, the sensor may better our cost, excitation, and power requirements application in different magnetic field detection environments.

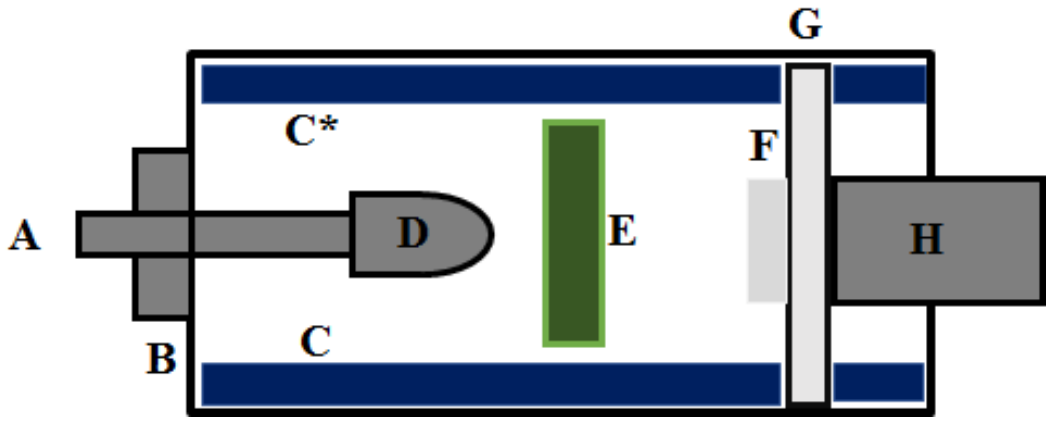

Figure 5.12: A cross-sectional schematic of the proposed miniaturized NV detector including components labelled from A to H. External power is supplied to the microwave circuit, LED, and photo-detector.

5.6 Conclusion

In this chapter, a NV sensor with a different light excitation and collection method was conceptualized and designed for magnetic field sensing applications - we call this sensor the "Sparrow NV sensor". The main aspect of the design including the design parameters, optics, microwave engineering, and electronics was detailed. Optical excitation was achieved using a 532 nm laser set to wide-area illumination with the aid of a BE. The resulting two-dimensional fluorescence was projected onto a CCD camera detecting the entire image of the diamond. The CCD fluorescence frames obtained were corrected for dark current, bias, and sensitivity-related errors. To characterize the emission light performance of the new system, the SBR/SNR of the system was analyzed and compared with a traditional confocal system under different optical excitation conditions corresponding to the saturation and undersaturation laser regions. Results obtained from performance metrics indicates that the conventional confocal set-up outperforms our new design in terms of their SNR at both saturation and undersaturation optical power regions. In the optical power saturation region,

the SNR and SBR of both designs are comparable, while in the undersaturation power region, the confocal system greatly outperforms the new design in terms of SNR and SBR. In the low optical power region, our proposed design shows almost the same changes in the background intensity as the confocal system. The implication of these a result is that the utmost performance of both systems is guaranteed in the undersaturation region (region of low power excitation) and thus our new system excitation performance is best in this region.

While the SBR can be controlled during fluorescence testing by using better NV sensor mounts and minimizing background noise, the SNR is inherent in the fluorescence detection process. Aside from the excitation laser power having an influence on the SNR, the detecting element contributes largely to the SNR, thus CCD detectors with highly effective QE are desired for an optimized detection scheme. The new system has a total power consumption of 107 dBm, nonetheless, we seek minimal power requirements. For this reason, a further miniaturized model of the design presented in this chapter with a lesser power consumption requirement is proposed. Although the sensitivity of the proposed scalable NV sensors hasn't been tested, it speculated confirmed that the miniaturized sensor meets our cost, excitation, and power requirement need for several magnetic sensing applications. Lastly, the quantitative results obtained for SNR and SBR represents the emission light performance of our system and contributes to a better understanding of the contrast of the ODMR spectrum obtained in following chapter as contrast is influenced by both SNR and SBR [230, 232].

Chapter 6

Magnetic Field Detection Potential and Sensitivity of the Sparrow NV Sensor.

"The mind is a magnetic field. When it a attract good thoughts, it will produce good deeds."

– Lailah Gifty Akita

Some part of this chapter is based on the manuscripts:

Ejalonibu, H., Sarty, G., & Bradley, M. (2021). Towards the design and operation of a uniformly illuminated NV detector for magnetic field mapping application. (to appear in the Journal of *Measurement Science and Technology*, IOP).

6.1 Introduction

Research aimed at engineering sensors for the detection, imaging, and quantification of magnetic fields will continue to gain wide interest owing to their numerous applications. For example, magnetic field sensors are enabling instruments for the fundamental studies of magnetism and symmetries [4, 5], spin dynamics [6], mechanical motions [7, 8], and neuronal activities in biological systems [233]. Furthermore, magnetic field sensors have applications in medical imaging devices, current and position sensing, as well as in motor diagnostics devices [1, 2, 3]. Over the years, several methods have been developed to sense and image magnetic fields with a majority of these methods further integrated with medical imaging

modalities operated at low fields e.g., MRIs. One common but classical method of detection will make use of the inductive coils operated based on Faraday's law of induction. SQUIDs and AVMs have also been used for detection in the past. Interested readers are referred to the following literature: Dabek et al., 2012 [28], Zotev et al., 2007 [29], Clarke et al., 2005 [30], and Savukov et al., 2013 [37] to mention a few. However, the significant drawbacks of the SQUIDs and the AVMs explained earlier in chapter 1 limit their use for everyday detection.

Magnetometers based on NV centres in diamond render an alternative with the potential to replace other detection protocols and with a sensitivity well above the classical limit. The NV centres in diamond have numerous properties making it a sought after candidate for magnetic field sensing applications. Its long spin coherence time at room temperature and efficient method of initialization and optical readout of electronic spins make it an ideal candidate for magnetometry. Above all, NV-based sensors can be operated over a wide range of temperatures with high spatial resolution. Since NV centres have not gained much popularity for magnetic field detection in medical imaging devices, it is the main purpose of this part of the thesis to detect the B_0 field at the magnet bore of a Halbach magnet of a prototype compact MRI at the Space MRI Laboratory, University of Saskatchewan. The aim is to detect magnetic fields by measuring the NV fluorescence which depends on the magnitude and orientation of the B_0 field with respect to the NV axis. Here, the measurement principle of a quantum magnetic field sensor will be described and the experimental demonstration of the detection of the magnetic field in the bore of a Halbach magnet configuration with an ensemble of NV centres in diamond will be shown. Several works of literature have demonstrated this principle in other magnet configurations using a confocal detector setup. Our method in this chapter differs in the sense that a non-confocal system designed in chapter 5 was used, hence making it possible to define wide-area magnetic field detection. The detector designed in chapter 5 called the "Sparrow NV sensor" here is tested for its magnetic field detection potential using the continuous wave ODMR sensing protocol.

6.2 Theory

Probing static fields in low-field MRIs is becoming an important characterization technique most especially for MRIs developed with non-uniform B_0 fields, for example in Ref. [212]. Two common protocols exist for detecting static magnetic fields, these are the continuous wave optically detected magnetic resonance (CW-ODMR) and the Ramsey sequence. The CW-ODMR technique being a commonly used technique is an easy method because optical excitation, microwave manipulation and optical read-out are carried out simultaneously. In this technique, a 532 nm laser continuously excites the NV^- spins into the darker excited state. If the ^{14}N hyperfine interaction is not considered, the fluorescence intensity of Lorentzian CW-ODMR spectrum when written as a function of the microwave frequency f_m, is given as:

$$I(f_m) = I_o \left[1 - C_o F \left(\frac{(\Delta\nu/2)^2}{(\nu - \nu_o)^2 + (\Delta\nu/2)^2}\right)\right], \tag{6.1}$$

where I_o is the fluorescence intensity when the spins are off-resonant, F is the spectral line shape, C_o is the spectral line contrast, and $\Delta\nu$ is the full width at half maximum (FWHM). Consider a situation where the NV^- centre is coupled to a substitutional nitrogen centre (P1), we account for the P1 spin-flip rate, λ_{P1} into the formula of $\Delta\nu$. In the work of Jensen et al. [234], λ_{P1} is expressed as:

$$\lambda_{P_1} = \gamma f_R^2 / \left(1 + \frac{f_R^2}{f_{sat}^2}\right), \tag{6.2}$$

where f_R is the Rabi frequency (measured in MHz), f_{sat} is the saturated Rabi frequency, and γ is the fit parameter. Both f_{sat} and γ are determined by laser power from CW-ODMR measurements. In the weak laser excitation regime, $\Delta\nu$ can be expressed as:

$$\Delta\nu = \Gamma_{inh} + \sqrt{\frac{4\lambda_2^{eff} f_R^2}{\lambda_1 + \lambda_P + \lambda_{P1}} + \left(\frac{\lambda_2^{eff}}{\pi}\right)^2}, \tag{6.3}$$

where Γ_{inh} is the inhomogeneous linewidth, $\lambda_2^{eff} = \lambda_2 + 1/\lambda_P$, λ_1 is the longitudinal relaxation time, λ_2 is the transverse relaxation, and λ_P is the polarization rate. From Equation 6.1, the CW-ODMR contrast C_o can then be re-written as:

$$C_o = \frac{\epsilon\lambda_p}{(1-\epsilon)\lambda_1 + \lambda_P} \frac{(2\pi f_R)^2}{\left[(2\pi f_R)^2 + \lambda_2^{eff}(\lambda_1 + \lambda_P)\right]}, \tag{6.4}$$

ϵ in Equation 6.4 is the difference in fluorescence intensity. The derived Equation 6.4 represents the contrast C_o of the CW-ODMR technique.

Next, we derive the minimum sensitivity of an NV magnetometer using the CW-ODMR approach to measure DC magnetic fields by considering a typical ODMR spectrum in Figure 6.1, where the intensity of the profile is given by Equation 6.4.

The line width $\delta\nu$ is limited by the dephasing time T_2^*, which in turn is characterized by the inhomogenieties in the environment of the NV ensemble. The fluorescence intensity I is most sensitive to tiny changes in the magnetic field at the point of maximum slope:

$$\max\left|\frac{\delta I}{\delta\nu}\right| = \frac{C_0}{\delta\nu F} \tag{6.5}$$

The numerical parameter F is related to the specific profile of the NV resonance and always fixed between 0.7 and 0.77 for a Gaussian and Lorentzian shape of the resonance [235, 150]. If a measurement of duration t_m is considered, the fluorescence count collected per measurement $C = C_0 t_m$, and its corresponding photon shot noise is given by $\delta C \approx \sqrt{C_0 t_m}$, hence the shot-noise-limited detectable field η for the measurement can be calculated from the photon-shot noise at the point of maximum slope in Figure 6.1

$$\eta = \frac{\delta C}{\max\left|\frac{\delta C_0}{\delta\nu}\right|} \approx \frac{\sqrt{C_0 t_m}}{t_m \max\left|\frac{\delta C_0}{\delta\nu}\right|} \tag{6.6}$$

Substituting Equation 6.5 into Equation 6.6, we obtain the value of the optimized minimum magnetic field sensitivity of NV detection protocol as:

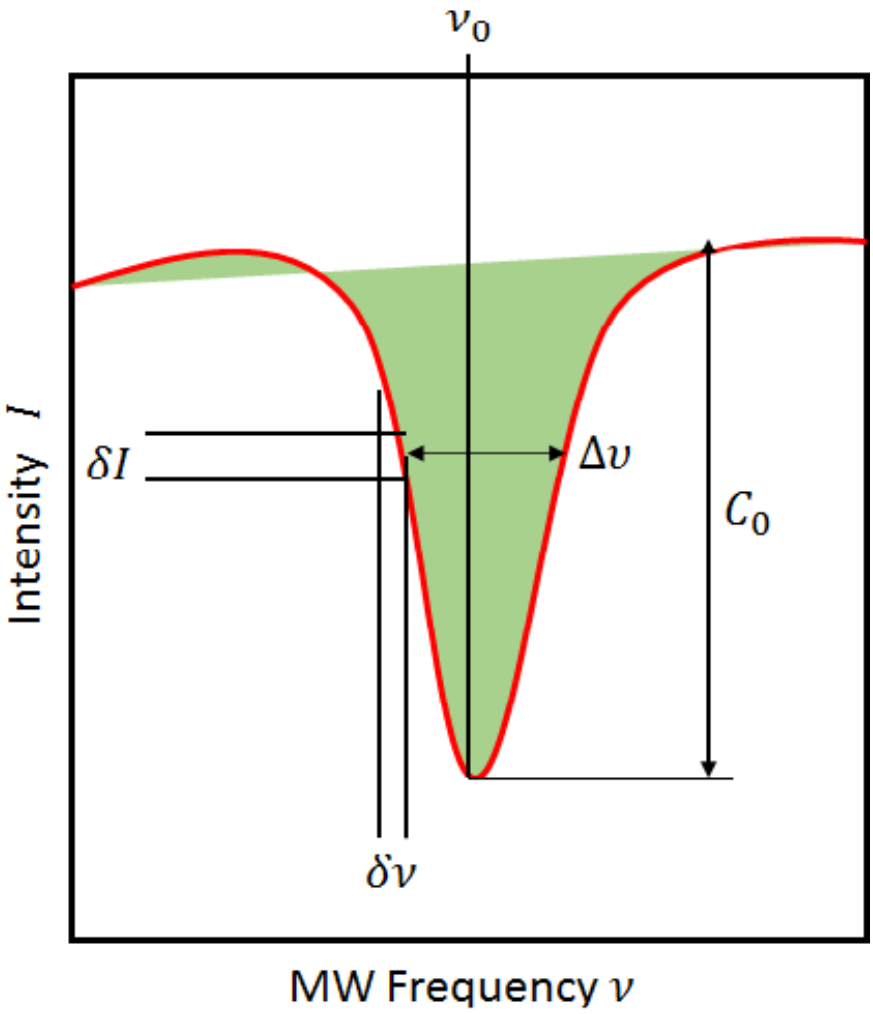

Figure 6.1: Intensity profile of an NV ODMR spectrum used to derive the sensitivity of a DC magnetic field measurement.

$$\eta = R\frac{\hbar}{g\mu_B}\frac{\Delta\nu}{\sqrt{NC_0T_2^*}} \tag{6.7}$$

from Equation 6.7, it is clear that the sensitivity of an NV detection protocol largely depends on C_0, $\Delta\nu$, and the NV spin dephasing time T_2^*. These parameters are not independent of each other; for example the resonance contrast C_0 may be increased by increasing the power of microwave excitation line but at the expense of increasing $\Delta\nu$ due to power broadening [236, 237, 238].

6.3 Experimental

6.3.1 Material

The sample used for this experiment is a bulk diamond (Element Six, Oxfordshire, OX, UK) of dimension $3 \times 3 \times 0.5$ mm^3 grown via the CVD technique. The ensemble of NV centres in the diamond crystal has a T_2^* time of about 1 μs, and a T_2 value of 100 μs as measured by the manufacturer. The NV centres in the SCD sample are randomly oriented along one of the four crystallographic axes of the diamond lattice. The four NV centre crystallographic orientation in an ensemble of NV centres can be exploited for the vectorial reconstruction of the static magnetic field.

6.3.2 Optical System

Figure 6.2 is a photograph of the laboratory setup of the magnetic field detection system. The detection system harnessed here has been well studied for its emission light performance in chapter 5. The detector element is a diamond with an ensemble of NV centres placed in the bore of the magnet. The diamond sample was illuminated with a compact collimated laser-diode-pumped (DPSS), 532 nm laser module (Thorlabs Inc., Montpellier St. Laurent, QC, CA) with a power of 4.5 mW. The laser interfaces the BE (Edmund Optics Inc., Barrington, NJ, USA) increases its diameter. A long pass dichroic mirror with a cut-on wavelength of 567 nm (Thorlabs Inc., Montpellier St. Laurent, QC, CA) placed 45° reflects green light and

transmits red. Emitted red fluorescence from the diamond sample then passes through the dichroic mirror and is filtered by a bandpass filter (Iridian Spectral Technologies, Ottawa, ON, CA) in the wavelength range 595 - 800 nm. The emitted fluorescence is afterwards collected with a 3MP coloured Chameleon USB 2.0 camera (FLIR, Vancouver, BC, CA) with a 8 mm C-series fixed focal length imaging lens (Edmund Optics Inc., Barrington, NJ, USA) in the collection path. Finally, microwave frequency was delivered to the diamond sample by using a double-sided copper tape soldered to an SMA connector attached to the back of the diamond sample. The antenna shape has been chosen to provide a uniform microwave magnetic field over the FOV of the camera. The main characteristics of the experimental setup are summarized in Table 6.1.

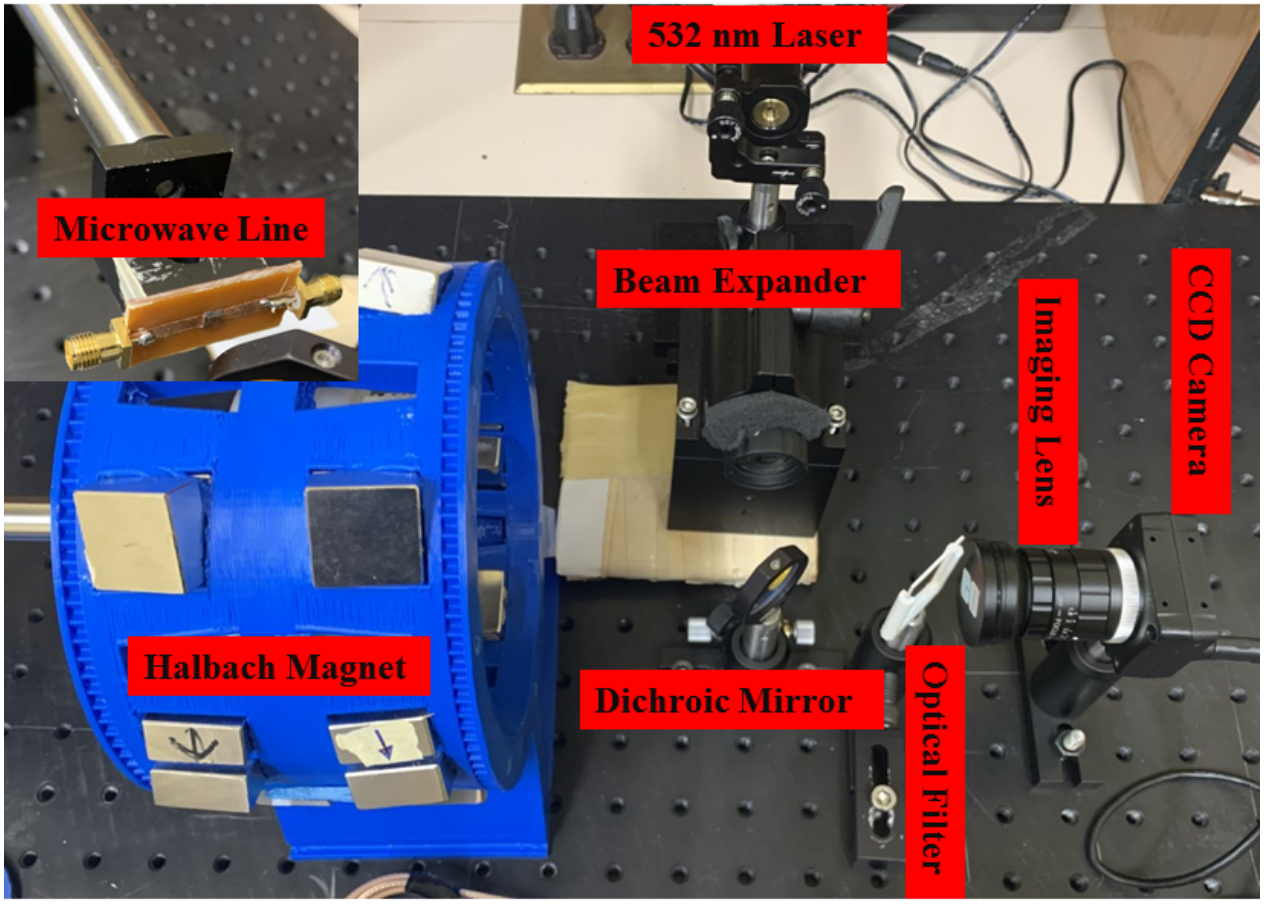

Figure 6.2: Photograph of the experimental detection system. The diamond sample placed on a microwave line is stationed in the bore of the Halbach magnet. At the top left corner is an expanded view of the diamond sample on the microwave line in the bore of the magnet.

Table 6.1: Main characteristics of the optical beam, and the imaging system used for the experiment.

Parameter	Value
Laser wavelength	532 nm
Laser power	4.5 mW
Exposure length	1 sec
Size of CCD pixel (integrated bunch of pixel)	1/3”
Microwave resolution	10 MHz
Camera resolution	1296 ×964
Line width ($\Delta\nu$)	20 MHz
Total acquisition time (T)	30 secs
Contrast of ODMR (C_0)	0.24

6.3.3 Data Acquisition and Processing

Before every data acquisition, the stability of the illumination source was checked. A rough estimate of the laser power is measured with a home-built photometer. The photometer detected the approximate variability in the intensity of the laser light source. Since the laser was not equipped with a constant current source, random fluctuations in the laser intensity was observed. Fluorescence frames were obtained from the optical design simultaneously as the microwave frequency is swept. The camera frames were appended to the computer memory to form a 3D volume of data giving the value of luminescence for each pixel (x,y) of the camera at different frequency sweep value (ν). Software triggers incorporated with the camera enabled synchronization of the microwave source swept from 2.60 GHz - 3.00 GHz in steps of 10 MHz[1]. The total acquisition time is about 30 secs. Although the frequency spectrum was only collected from 2.70 GHz to about 3.0 GHz in this experiment, frequency sweeps were started at 2.60 GHz to remove spurious oscillations associated with the use of the LimeSDR [239]. Subsequently, the CCD fluorescence frames obtained were corrected for

[1]Frequency steps of 61.44 MHz were obtainable on the LimeSDR, however, the limit was pushed to 10 MHz in our design.

dark current, bias, and sensitivity-related errors as explained in chapter 5. The processed 3D data volume was later used to reconstruct an ODMR spectrum with each image frame representing a microwave frequency point. To improve sensitivity, it was necessary to repeat measurements at least twice and then average because the sensitivity is proportional to $1/\sqrt{N}$.

6.4 Results

Figure 6.3 shows the measured ODMR spectrum in the absence of an applied magnetic field $B_0 = 0$. The recorded ODMR fitted with a sum of Lorentzian exhibits two dips corresponding to the $m_s = 0 \longrightarrow m_s = \pm 1$ transition due to the intrinsic properties of the host diamond material. This separation results from transitions occurring from lifting of spin degeneracy [43, 240]. The ODMR dips have a linewidth $\Delta\nu$ with FWHM of approximately 1.77 MHz. The strain parameter measured from the spectrum in Figure 6.3 is approximately 3.17 ± 0.2 MHz and because of its value, this splitting cannot be attributed to the earth's magnetic field. The earth's magnetic field mostly induces a splitting less than 2 MHz [241]. The strain parameter largely depends on the temperature and intrinsic properties of the NV defect. The strain value can range from a few KHz to MHz depending on the purity and nature of the NV hosting diamond. The zero-field splitting parameter which is the average of both resonance dips is 2.871 GHz, nonetheless, in general, $E \ll D$ is always satisfied [242].

Figure 6.4 shows the distribution of the different NV centres in the diamond sensor. A randomly oriented magnetic field generated by a Halbach magnet configuration was measured using the ODMR technique. The measured spectra in Figure 6.4 clearly exhibit four resonance dips in contrast to the eight resonance dips obtained when the magnetic field is not aligned with any of the four NV centres. The applied magnetic field in the bore of the magnet can be deduced by solving the eigenvalue of the spin Hamiltonian in Equation 5.2. According to the separation of the dip profiles observed, each NV centre experiences static magnetic field in the range 2.14 - 6.07 mT of the Halbach magnet. It should be noted that the value of the magnet field detected here is approximate due to the frequency resolution limitations

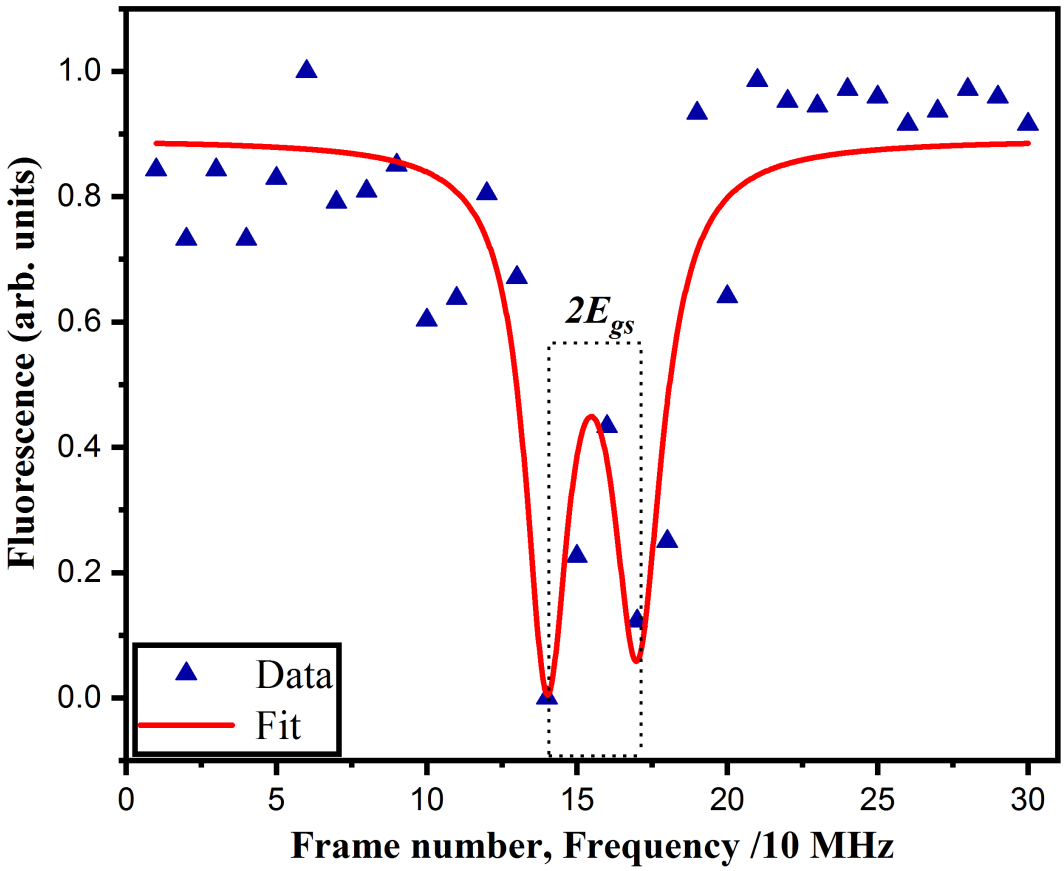

Figure 6.3: Optically detected magnetic resonance (ODMR) spectrum measured at room temperature showing the fluorescence signal of an ensemble of NV^- in the absence of applied magnetic field B_0.

of the microwave generator in this experiment.

The magnetic field sensitivity of the Sparrow detector was then evaluated. The sensitivity was calculated using Equation 6.6 with required parameters extracted from the ODMR spectrum in Figure 6.4 and in Table 6.1. The value of η is estimated to be approximately 0.2 $\mu T/\sqrt{Hz}$.

6.5 Discussion

The magnetic field detection potential and sensitivity of the Sparrow NV sensor were tested and reported in this chapter. Measurement uncertainties related to the use of this technique are partly related to the miscut of the diamond (orientation) and misalignment in the optical

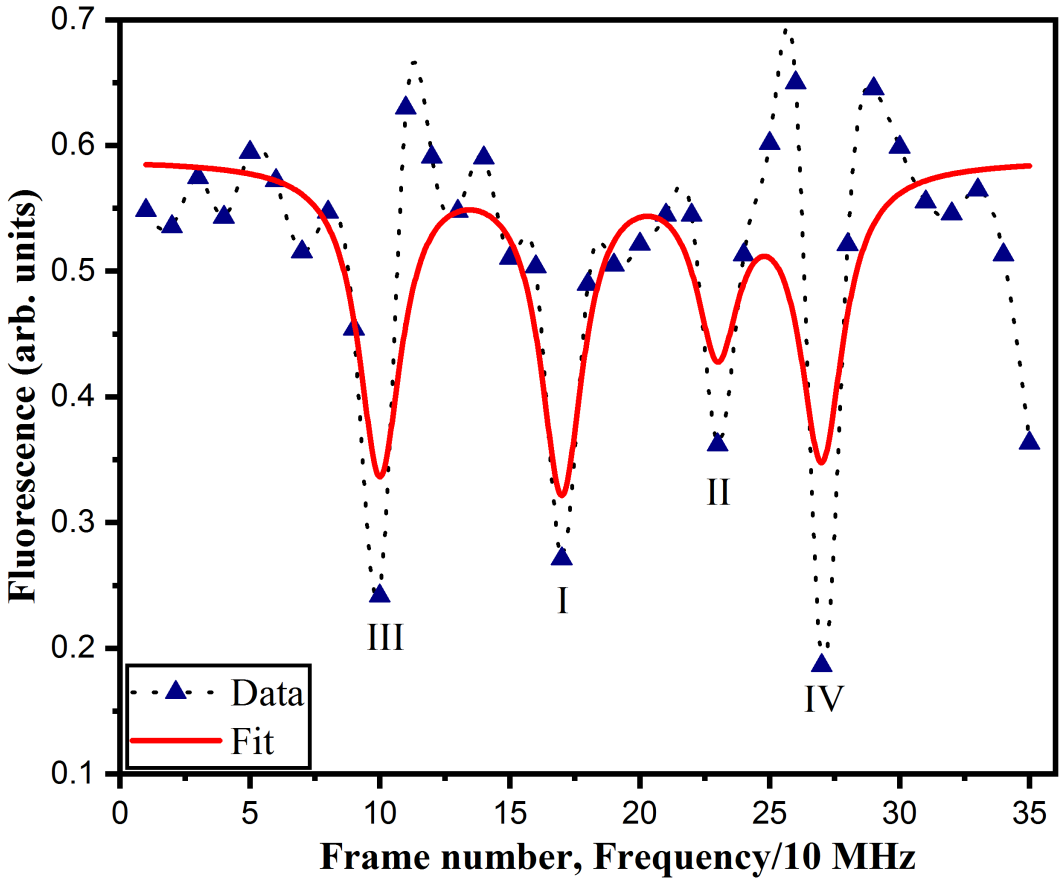

Figure 6.4: ODMR spectra measured at ambient temperature with a magnetic field B_0 showing the experimental data fitted with a sum of Lorentzian. The raw data obtained from data frames are composed of a full ODMR spectrum for each pixel. Under the static magnetic field of a permanent magnet, four NV orientations produced visible dips based on the Zeeman effect.

setup. In Figure 6.4, eight resonance line dips were expected in theory, nonetheless, four dips were resolvable. This is accounted for by the resolution of the ODMR spectrum. The ODMR resolution of the technique here was limited by the frequency resolution of the microwave source and the stability of the laser line used. Typically, microwave frequency resolutions in the kHz range as demonstrated in Ref. [243, 241] are desired. Earlier work on the characterization of B_0 in the Sparrow MRI in Ref. [244] measured approximately 8 mT in the bore of the magnet. However, during the time this experiment was set up, the Halbach magnet was reassembled resulting in the variation of the magnetic field observed. A Hall probe sensor was used to confirm our result and it was found that the B_0 in the bore of the re-assembled magnet is around 6 mT.

The magnetic field sensitivity of the Sparrow NV sensor was estimated to be approximately 0.2 $\mu\mathrm{T}/\sqrt{Hz}$ - this result is in agreement with the work of Lee et al. [245] stating that the magnetic field sensitivity of the CW-ESR method is limited to about $1\mu\mathrm{T}/\sqrt{Hz}$. The value of the minimum detectable magnetic field sensitivity is dependent on C_0, $\Delta\nu$, and the NV spin dephasing time T_2^*. The line width, $\Delta\nu$ observed in this experiment is large (20 MHz). This is due to the power broadening resulting from continuous laser pumping. Using pulsed ODMR measurement protocols [246] can help avoid the broadening effect and result in sharper ODMR linewidth. In a similar vein, line broadening can also result from the high quantity of nitrogen atoms that are not converted into NV centres. The manufacturer's specifications guide indicates that the nitrogen concentration in the diamond sample used for this experiment is about 800 ppb before treatment. Increasing the yield of nitrogen to NV centre conversion will help decrease the line broadening effect. In particular, using an isotopically enriched diamond is an adequate approach to eliminate the effect of the nuclear spin bath due to $^{13}\mathrm{C}$ present in natural diamond [243].

In general, enhanced magnetic field sensitivity can be achieved using different methods. For example, sophisticated pulse sequences [247, 248, 131, 236] have proven effective in improving sensitivity of the NV sensing protocol. It is not untrue that the sensitivity of magnetometers using colour centres is limited by poor photon collection and detection efficiency, therefore methods designed for efficient excitation and collection of light from a dense ensemble of NV centres are also needed for ramping up the sensitivity of detection. An example is the light-trapping diamond waveguide (LTDW) geometry developed by Clevenson et al. [249] which was used to realize more than 3 orders of magnitude improvement in the ODMR signal in comparison to single-pass geometry. Following the work of Clevenson et al. [249] on LTDW, Ma et al. [250] presented an optical-frequency modulated microwave collection method achieving unprecedented sensitivity for static magnetic-field detection. Their proposed collection technique enables a fluorescence collection of over 40% and an efficient pump absorption. By applying a frequency modulated (FM) microwave followed by a lock-in technique on the reso-

nance frequency point, a magnetic field sensitivity of approximately 14 nT/$\sqrt{Hz}$ was achieved.

6.6 Conclusion

In this chapter, the magnetic field detection potential and sensitivity of the Sparrow NV sensor were tested using a homebuilt Halbach magnet configuration. Fluorescence frames were obtained from the optical design simultaneously as the microwave frequency was swept. The camera frames were appended to the computer memory to form a 3D volume of data giving the value of luminescence for each pixel (x,y) of the camera at different frequency sweep (ν) with a total acquisition time of about 30 secs. ODMR measurement was carried out both in the presence and absence of an applied magnetic field B_0. The measured spectra in the presence of a magnetic field exhibit four resonance dips in contrast to the eight resonance dip obtained when the magnetic field is not aligned with any of the four NV centres. According to the dip profiles observed, each NV centre experiences a static magnetic field in the range 2.14 - 6.07 mT of the Halbach magnet. The sensitivity was estimated and found to be approximately 0.2 μT/$\sqrt{Hz}$. These results pave way for the development of scalable NV sensors using the excitation and collection methods adopted in this thesis.

Chapter 7

Conclusion

"There is no real ending. It's just the place where you stop the story"

– Frank Herbert

7.1 Summary

The overall aim of this dissertation was to address specific problems in the material science, microwave engineering, and magnetometry aspect of the NV centre discipline. Additionally, it also establishes the feasibility of this approach in the characterization of low-magnetic field experimental MRIs. In particular, the aim was (i) to fabricate NV sensors based on nitrogen-vacancy (NV) centres in polycrystalline diamonds (PCDs) for magnetic field sensing applications, and (ii) design, construct and test the performance of an NV detector using a different excitation scheme from the traditionally well known confocal system of measurement.

To realize the above-listed goals, the parameter space(s) for the fabrication of negatively charged NV centres in PCDs was first explored. In this part of the study, we investigated the effect of nitrogen flow rate on the morphology, optical, and photoluminescence (PL) properties of PCDs deposited at low-pressure conditions. This study not only offers a standard recipe to grow inexpensive diamonds with NV centres over large areas, but also revealed interesting findings on the effect of nitrogen flow rates on the morphology, physical properties,

and optical properties of PCDs deposited at low-pressure conditions. The study was crucial in benchmarking optimal parameters space for the growth of nitrogen-doped polycrystalline diamonds suitable for sensing applications. Once a growth parameter space was identified, it was essential to study the influence of a step-wise surface nitrogen doping process on PCDs and this was used to explain the dominance of neutral charged NV (NV^0) centres in PCDs deposited at low pressure using the chemical vapour deposition (CVD) technique. This aspect of our study helps to give a better understanding of the formation of negatively charged NV centres (NV^-) in PCDs deposited at low pressure. By using a step-wise doping technique, it was possible to explain the formation of NV centres at low pressure. At the end of chapter4, we identified issues relating to NV centre orientations and the poor sensitivities in PCDs and made recommendations for future research.

Furthermore, we designed, constructed, and tested the performance of a scalable NV-based detector for magnetic sensing applications. In this part of the dissertation, an NV centre optical detector was conceptualized and designed for magnetic field detection. The instrumentation and automation of the setup were detailed. The system status and proposed performance for sensitivity were accessed in terms of signal-to-noise ratio (SNR) and signal-to-background ratio (SBR). The study established a metric to compare the newly designed detection system to the conventional confocal system of detection. For magnetometry applications, it is important to design an optical setup for detection. The magnetic field detection potential and sensitivity of the Sparrow NV sensor built was tested using a homebuilt Halbach magnet configuration. According to the ODMR dip profiles observed, each NV centre experienced a static magnetic field in the range 2.14 - 6.07 mT of the Halbach magnet. The sensitivity was estimated and found to be approximately 0.2 $\mu T/\sqrt{Hz}$. These results pave way for the development of scalable NV sensors using the excitation and collection methods adopted in this thesis.

7.2 Future Directions

Our work in this thesis is mostly limited by time and the availability of resources. Although several areas including fabrication to the application of NV sensors were touched, future directions to this work are stated below:

1. **Orientation of NV centres:** Preferential orientation of NV centres in diamond films is targeted at limiting unwanted background noise, increasing sensitivity, and simplifying device operations [111]. The preferential orientation of NV centres has been achieved in SCDs [117, 118], this result however remains a nightmare in PCDs because of the random orientation of grains. While it is not experimentally feasible to engineer perfectly preferentially oriented NV centres in PCDs, it is possible to have approximately 70% of the grains containing NV centres aligned in the same crystal direction. This can be achieved via careful deposition parameter(s) tuning as demonstrated in chapter 3.

2. **Stabilizing surface charge state:** In most cases, NV centres located within a few nanometers from the diamond surface are found in their neutral charged states [90]. This becomes a critical problem in PCDs because of the presence of grain boundaries and nanocrystalline diamonds at the surface harbouring a huge amount of graphitic impurities. Certainly, there is a need to understand the mechanism of charge state conversion in both SCDs and PCDs. Commonly studied is the mechanism of NV centre formation and charge state conversions in SCDs. However, to date, there have been no studies explicitly detailing the same in PCDs.

3. **Detecting dynamic magnetic field (B_1 in MRI):** Aside from detecting static and slowly varying magnetic fields, the NV centre can also be used to detect dynamic fields. The large bandwidth sensing capability (up to GHz) of NV centres is important in the study of the spin dynamics in solid-state and biological samples [245], for example, nuclear spins precession in bio-samples occurs in the MHz regime. This is the ultimate goal as we envisage the use of this method to improve the SNR in low-field MRIs -

research aimed at this will be pursued in the future. The detection of dynamic magnetic fields needs to be carried out using a spin Hahn-echo sequence.

4. **Improving sensitivity:** Aside from the methods used in obtaining better sensitivities discussed in chapter 6, superb sensitivities for NV magnetometers require a low-noise mode of operation at cryogenic temperatures, thus constituting an obstacle for our proposed room temperature low-field MRI application. For every magnetic field sensing protocol, the precision of the phase ϕ is usually improved by repeating the spin measurement procedure. However, accumulated readout overhead remarkably reduces the sensitivity of NV magnetometers [251, 252, 253]. The increase in total sensing time due to repeated measurements and the time is taken to prepare experiments decreases the sensitivity of the NV sensing scheme. Therefore, there is a need to explore machine learning algorithms applied to NV sensors detection at room temperature, maybe in the end we might be able to obtain sensitivities that scale as the Heisenberg limit and surpass the classical standard measurement sensitivity.

References

[1] Vivien Schukar, Enrico Köppe, Detlef Hofmann, Anja Westphal, Mario Sahre, Xin Gong, Matthias Bartholmai, and Uwe Beck. Magnetic field detection with an advanced fbg-based sensor device. *Procedia Engineering*, 168:1270–1274, 2016.

[2] Yong-Seok Kim, Seong-Cho Yu, Jeong-Bong Lee, and Heebok Lee. A new class of lc-resonator for micro-magnetic sensor application. *Journal of magnetism and magnetic materials*, 304(1):117–121, 2006.

[3] Pavel Ripka. Security applications of magnetic sensors. In *Journal of Physics: Conference Series*, volume 450, page 012001. IOP Publishing, 2013.

[4] HB Dang, Adam C Maloof, and Michael V Romalis. Ultrahigh sensitivity magnetic field and magnetization measurements with an atomic magnetometer. *Applied Physics Letters*, 97(15):151110, 2010.

[5] Dmitry Budker and Michael Romalis. Optical magnetometry. *Nature physics*, 3(4):227–234, 2007.

[6] CL Degen. Scanning magnetic field microscope with a diamond single-spin sensor. *Applied Physics Letters*, 92(24):243111, 2008.

[7] Olivier Arcizet, Vincent Jacques, Alessandro Siria, Philippe Poncharal, Pascal Vincent, and Signe Seidelin. A single nitrogen-vacancy defect coupled to a nanomechanical oscillator. *Nature Physics*, 7(11):879–883, 2011.

[8] Shimon Kolkowitz, Ania C Bleszynski Jayich, Quirin P Unterreithmeier, Steven D Bennett, Peter Rabl, JGE Harris, and Mikhail D Lukin. Coherent sensing of a mechanical resonator with a single-spin qubit. *Science*, 335(6076):1603–1606, 2012.

[9] Michael J Caruso, Tamara Bratland, Carl H Smith, and Robert Schneider. A new perspective on magnetic field sensing. *SENSORS-PETERBOROUGH-*, 15:34–47, 1998.

[10] Whittier Myers, Daniel Slichter, Michael Hatridge, Sarah Busch, Michael Mößle, Robert McDermott, Andreas Trabesinger, and John Clarke. Calculated signal-to-noise ratio of mri detected with squids and faraday detectors in fields from 10 μt to 1.5 t. *Journal of Magnetic Resonance*, 186(2):182–192, 2007.

[11] Claude Cavoit. Closed loop applied to magnetic measurements in the range of 0.1–50 mhz. *Review of scientific instruments*, 77(6):064703, 2006.

[12] Slawomir Tumanski. Induction coil sensors—a review. *Measurement Science and Technology*, 18(3):R31, 2007.

[13] VE Korepanov. The modern trends in space electromagnetic instrumentation. *Advances in Space Research*, 32(3):401–406, 2003.

[14] HC Séran and P Fergeau. An optimized low-frequency three-axis search coil magnetometer for space research. *Review of scientific instruments*, 76(4):044502, 2005.

[15] Kunihisa Tashiro. Induction coil magnetometers. In *High sensitivity magnetometers*, pages 1–39. Springer, 2017.

[16] V Korepanov, R Berkman, L Rakhlin, Ye Klymovych, A Prystai, A Marussenkov, and M Afanassenko. Advanced field magnetometers comparative study. *Measurement*, 29(2):137–146, 2001.

[17] Christophe Coillot, Joel Moutoussamy, Richard Lebourgeois, Sébastien Ruocco, and Gérard Chanteur. Principle and performance of a dual-band search coil magnetometer: A new instrument to investigate fluctuating magnetic fields in space. *IEEE Sensors Journal*, 10(2):255–260, 2009.

[18] Matthias Schmelz and Ronny Stolz. Superconducting quantum interference device (squid) magnetometers. In *High Sensitivity Magnetometers*, pages 279–311. Springer, 2017.

[19] Seong-Joo Lee, Keunhong Jeong, Jeong Hyun Shim, Hyun Joon Lee, Sein Min, Heelim Chae, Sung Keon Namgoong, and Kiwoong Kim. Squid-based ultralow-field mri of a hyperpolarized material using signal amplification by reversible exchange. *Scientific reports*, 9(1):1–8, 2019.

[20] D Drung, C Abmann, J Beyer, A Kirste, M Peters, F Ruede, and Th Schurig. Highly sensitive and easy-to-use squid sensors. *IEEE Transactions on Applied Superconductivity*, 17(2):699–704, 2007.

[21] Rainer Körber, Jan-Hendrik Storm, Hugh Seton, Jyrki P Mäkelä, Ritva Paetau, Lauri Parkkonen, Christoph Pfeiffer, Bushra Riaz, Justin F Schneiderman, Hui Dong, et al. Squids in biomagnetism: a roadmap towards improved healthcare. *Superconductor Science and Technology*, 29(11):113001, 2016.

[22] Ethan Y Cho, Hao Li, Jay C LeFebvre, Yuchao W Zhou, RC Dynes, and Shane A Cybart. Direct-coupled micro-magnetometer with y-ba-cu-o nano-slit squid fabricated with a focused helium ion beam. *Applied physics letters*, 113(16):162602, 2018.

[23] E Trabaldo, R Arpaia, M Arzeo, E Andersson, D Golubev, F Lombardi, and T Bauch. Transport and noise properties of ybco nanowire based nanosquids. *Superconductor Science and Technology*, 32(7):073001, 2019.

[24] VV Danilov, KK Likharev, and OV Snigirev. Signal and noise parameters of squids. In *SQUID'80. Superconducting Quantum Interference Devices and their Applications*, pages 473–507. De Gruyter, 2019.

[25] Jörg Wrachtrup and Amit Finkler. Single spin magnetic resonance. *Journal of Magnetic Resonance*, 269:225–236, 2016.

[26] M Nisenoff and S Wolf. Observation of a cos φ term in the current-phase relation for" dayem"-type weak link contained in an rf-biased superconducting quantum interference device. *Physical Review B*, 12(5):1712, 1975.

[27] Robert Rifkin, Daniel A Vincent, Bascom S Deaver Jr, and Paul K Hansma. rf squid's in the nonhysteretic mode: detailed comparison of theory and experiment. *Journal of Applied Physics*, 47(6):2645–2650, 1976.

[28] Juhani Dabek, Panu T Vesanen, Koos CJ Zevenhoven, Jaakko O Nieminen, Raimo Sepponen, and Risto J Ilmoniemi. Squid-sensor-based ultra-low-field mri calibration with phantom images: Towards quantitative imaging. *Journal of Magnetic Resonance*, 224:22–31, 2012.

[29] Vadim S Zotev, Andrei N Matlashov, Petr L Volegov, Algis V Urbaitis, Michelle A Espy, and Robert H Kraus Jr. Squid-based instrumentation for ultralow-field mri. *Superconductor Science and Technology*, 20(11):S367, 2007.

[30] John Clarke, Robert McDermott, Alexander Pines, and Andreas Heinz Trabesinger. Squid detected nmr and mri at ultralow fields, April 26 2005. US Patent 6,885,192.

[31] Andrei N Matlachov, Petr L Volegov, Michelle A Espy, John S George, and Robert H Kraus Jr. Squid detected nmr in microtesla magnetic fields. *Journal of Magnetic Resonance*, 170(1):1–7, 2004.

[32] Jialei Wang, Kang Yang, Ruihu Yang, Xiangyan Kong, and Wei Chen. Squid gradiometer module for fetal magnetocardiography measurements inside a thin magnetically shielded room. *IEEE Transactions on Applied Superconductivity*, 29(2):1–4, 2018.

[33] YP Pan, SY Wang, XY Liu, YS Lin, LX Ma, Y Feng, Z Wang, L Chen, and YH Wang. 3d nano-bridge-based squid susceptometers for scanning magnetic imaging of quantum materials. *Nanotechnology*, 30(30):305303, 2019.

[34] IK Kominis, TW Kornack, JC Allred, and Michael V Romalis. A subfemtotesla multichannel atomic magnetometer. *Nature*, 422(6932):596–599, 2003.

[35] Arnold L Bloom. Principles of operation of the rubidium vapor magnetometer. *Applied Optics*, 1(1):61–68, 1962.

[36] IM Savukov, VS Zotev, PL Volegov, MA Espy, AN Matlashov, JJ Gomez, and RH Kraus Jr. Mri with an atomic magnetometer suitable for practical imaging applications. *Journal of Magnetic Resonance*, 199(2):188–191, 2009.

[37] I Savukov and T Karaulanov. Anatomical mri with an atomic magnetometer. *Journal of Magnetic Resonance*, 231:39–45, 2013.

[38] SJ Seltzer and MV Romalis. High-temperature alkali vapor cells with antirelaxation surface coatings. *Journal of Applied Physics*, 106(11):114905, 2009.

[39] Ahmed L Elrefai, Ichiro Sasada, and Shoumu Harada. Gradiometer and magnetometer integration using a pair of fundamental mode orthogonal fluxgate sensor heads. *IEEE Transactions on Magnetics*, 51(11):1–4, 2015.

[40] Jen-Tzong Jeng, Chih-Cheng Lu, Hsiang-Wei Ku, Bo-Rei Huang, Meng-Huan Chia, and Xuan Thang Trinh. Three-axis micofluxgate with a fluxguide. *IEEE Transactions on Magnetics*, 55(7):1–4, 2019.

[41] E Yarar, S Salzer, V Hrkac, A Piorra, M Höft, R Knöchel, L Kienle, and E Quandt. Inverse bilayer magnetoelectric thin film sensor. *Applied Physics Letters*, 109(2):022901, 2016.

[42] Yaojin Wang, David Gray, David Berry, Junqi Gao, Menghui Li, Jiefang Li, and Dwight Viehland. An extremely low equivalent magnetic noise magnetoelectric sensor. *Advanced materials*, 23(35):4111–4114, 2011.

[43] A Gruber, A Dräbenstedt, C Tietz, L Fleury, J Wrachtrup, and C Von Borczyskowski. Scanning confocal optical microscopy and magnetic resonance on single defect centers. *Science*, 276(5321):2012–2014, 1997.

[44] Gopalakrishnan Balasubramanian, Philipp Neumann, Daniel Twitchen, Matthew Markham, Roman Kolesov, Norikazu Mizuochi, Junichi Isoya, Jocelyn Achard, Johannes Beck, Julia Tissler, et al. Ultralong spin coherence time in isotopically engineered diamond. *Nature materials*, 8(5):383–387, 2009.

[45] Liam P McGuinness, Yuling Yan, Alastair Stacey, David A Simpson, Liam T Hall, Dougal Maclaurin, Steven Prawer, P Mulvaney, J Wrachtrup, F Caruso, et al. Quantum measurement and orientation tracking of fluorescent nanodiamonds inside living cells. *Nature nanotechnology*, 6(6):358, 2011.

[46] Florian Dolde, Helmut Fedder, Marcus W Doherty, Tobias Nöbauer, Florian Rempp, Gopalakrishnan Balasubramanian, Thomas Wolf, Friedemann Reinhard, Lloyd CL Hollenberg, Fedor Jelezko, et al. Electric-field sensing using single diamond spins. *Nature Physics*, 7(6):459–463, 2011.

[47] Victor M Acosta, Erik Bauch, Micah P Ledbetter, Amir Waxman, L-S Bouchard, and Dmitry Budker. Temperature dependence of the nitrogen-vacancy magnetic resonance in diamond. *Physical review letters*, 104(7):070801, 2010.

[48] David R Glenn, Kyungheon Lee, Hongkun Park, Ralph Weissleder, Amir Yacoby, Mikhail D Lukin, Hakho Lee, Ronald L Walsworth, and Colin B Connolly. Single-cell magnetic imaging using a quantum diamond microscope. *Nature methods*, 12(8):736–738, 2015.

[49] David A Simpson, Robert G Ryan, Liam T Hall, Evgeniy Panchenko, Simon C Drew, Steven Petrou, Paul S Donnelly, Paul Mulvaney, and Lloyd CL Hollenberg. Electron paramagnetic resonance microscopy using spins in diamond under ambient conditions. *Nature communications*, 8(1):1–8, 2017.

[50] David Le Sage, Koji Arai, David R Glenn, Stephen J DeVience, Linh M Pham, Lilah Rahn-Lee, Mikhail D Lukin, Amir Yacoby, Arash Komeili, and Ronald L Walsworth. Optical magnetic imaging of living cells. *Nature*, 496(7446):486–489, 2013.

[51] HJ Mamin, M Kim, MH Sherwood, CT Rettner, K Ohno, DD Awschalom, and D Rugar. Nanoscale nuclear magnetic resonance with a nitrogen-vacancy spin sensor. *Science*, 339(6119):557–560, 2013.

[52] Tobias Staudacher, Fazhan Shi, S Pezzagna, Jan Meijer, Jiangfeng Du, Carlos A Meriles, Friedemann Reinhard, and Joerg Wrachtrup. Nuclear magnetic resonance spectroscopy on a (5-nanometer) 3 sample volume. *Science*, 339(6119):561–563, 2013.

[53] IM Savukov, SJ Seltzer, and Michael V Romalis. Detection of nmr signals with a radio-frequency atomic magnetometer. *Journal of Magnetic Resonance*, 185(2):214–220, 2007.

[54] Wei-Tang Chang, Kawin Setsompop, Jyrki Ahveninen, John W Belliveau, Thomas Witzel, and Fa-Hsuan Lin. Improving the spatial resolution of magnetic resonance inverse imaging via the blipped-caipi acquisition scheme. *Neuroimage*, 91:401–411, 2014.

[55] Milica Medved, Weiliang Du, Marta A Zamora, Xiaobing Fan, Olufunmilayo I Olopade, Peter M MacEneaney, Gillian Newstead, and Gregory S Karczmar. The effect of varying spectral resolution on the quality of high spectral and spatial resolution magnetic resonance images of the breast. *Journal of Magnetic Resonance Imaging: An Official Journal of the International Society for Magnetic Resonance in Medicine*, 18(4):442–448, 2003.

[56] S Chandra Shekar, Daniel T Hallinan Jr, Deanne M Taylor, and Eduard Y Chekmenev. Limits of spatial resolution of phase encoding dimensions in mri of metals, 2019.

[57] MI Faley, U Poppe, K Urban, DN Paulson, and RL Fagaly. A new generation of the hts multilayer dc-squid magnetometers and gradiometers. In *Journal of Physics: Conference Series*, volume 43, page 1199. IOP Publishing, 2006.

[58] F Baudenbacher, LE Fong, JR Holzer, and M Radparvar. Monolithic low-transition-temperature superconducting magnetometers for high resolution imaging magnetic fields of room temperature samples. *Applied Physics Letters*, 82(20):3487–3489, 2003.

[59] M Vengalattore, JM Higbie, SR Leslie, J Guzman, LE Sadler, and DM Stamper-Kurn. High-resolution magnetometry with a spinor bose-einstein condensate. *Physical review letters*, 98(20):200801, 2007.

[60] Zoran D Grujić, Peter A Koss, Georg Bison, and Antoine Weis. A sensitive and accurate atomic magnetometer based on free spin precession. *The European Physical Journal D*, 69(5):135, 2015.

[61] Stefan Groeger, Anatoly S Pazgalev, and Antoine Weis. Comparison of discharge lamp and laser pumped cesium magnetometers. *Applied Physics B*, 80(6):645–654, 2005.

[62] Vishal Shah, Svenja Knappe, Peter DD Schwindt, and John Kitching. Subpicotesla atomic magnetometry with a microfabricated vapour cell. *Nature Photonics*, 1(11):649–652, 2007.

[63] A Sandhu, A Okamoto, I Shibasaki, and AHMET Oral. Nano and micro hall-effect sensors for room-temperature scanning hall probe microscopy. *Microelectronic Engineering*, 73:524–528, 2004.

[64] Adarsh Sandhu, Kouichi Kurosawa, Munir Dede, and Ahmet Oral. 50 nm hall sensors for room temperature scanning hall probe microscopy. *Japanese journal of applied physics*, 43(2R):777, 2004.

[65] Yuhong Liu, David A Maurer, Gerald A Navratil, and Nicholas Rivera. High spatial resolution hall sensor array for edge plasma magnetic field measurements. *Review of Scientific Instruments*, 76(9):093501, 2005.

[66] MUNIR Dede, RİZWAN Akram, and Ahmet Oral. 3d scanning hall probe microscopy with 700 nm resolution. *Applied Physics Letters*, 109(18):182407, 2016.

[67] Roland Wiesendanger. Spin mapping at the nanoscale and atomic scale. *Reviews of Modern Physics*, 81(4):1495, 2009.

[68] U Hartmann. Magnetic force microscopy. *Annual review of materials science*, 29(1):53–87, 1999.

[69] JM Taylor, P Cappellaro, L Childress, L Jiang, D Budker, PR Hemmer, A Yacoby, R Walsworth, and MD Lukin. High-sensitivity diamond magnetometer with nanoscale resolution. *Nature Physics*, 4(10):810–816, 2008.

[70] Liam T Hall, Jared H Cole, Charles D Hill, and Lloyd CL Hollenberg. Sensing of fluctuating nanoscale magnetic fields using nitrogen-vacancy centers in diamond. *Physical review letters*, 103(22):220802, 2009.

[71] Albert Boretti and Stefania Castelletto. Nanometric resolution magnetic resonance imaging methods for mapping functional activity in neuronal networks. *MethodsX*, 3:297–306, 2016.

[72] Matthew Pelliccione, Alec Jenkins, Preeti Ovartchaiyapong, Christopher Reetz, Eve Emmanouilidou, Ni Ni, and Ania C Bleszynski Jayich. Scanned probe imaging of nanoscale magnetism at cryogenic temperatures with a single-spin quantum sensor. *Nature nanotechnology*, 11(8):700–705, 2016.

[73] Amila Ariyaratne, Dolev Bluvstein, Bryan A Myers, and Ania C Bleszynski Jayich. Nanoscale electrical conductivity imaging using a nitrogen-vacancy center in diamond. *Nature communications*, 9(1):1–7, 2018.

[74] Peter Hess. The mechanical properties of various chemical vapor deposition diamond structures compared to the ideal single crystal. *Journal of Applied Physics*, 111(5):3, 2012.

[75] JE Field. The mechanical and strength properties of diamond. *Reports on Progress in Physics*, 75(12):126505, 2012.

[76] V Blank, M Popov, G Pivovarov, N Lvova, and S Terentev. Mechanical properties of different types of diamond. *Diamond and related materials*, 8(8-9):1531–1535, 1999.

[77] Ali Erdemir, OL Eryilmaz, IB Nilufer, and GR Fenske. Synthesis of superlow-friction carbon films from highly hydrogenated methane plasmas. *Surface and Coatings Technology*, 133:448–454, 2000.

[78] S Cygan, L Jaworska, P Putyra, W Ratuszek, J Cyboron, and P Klimczyk. Thermal stability and coefficient of friction of the diamond composites with the titanium compound bonding phase. *Journal of Materials Engineering and Performance*, 26(6):2593–2598, 2017.

[79] D Meng, W Yue, F Lin, C Wang, and Z Wu. Thermal stability of ultrahard polycrystalline diamond composite materials. *Journal of Superhard Materials*, 37(2):67–72, 2015.

[80] A Grill. Electrical and optical properties of diamond-like carbon. *Thin solid films*, 355:189–193, 1999.

[81] K Honglertkongsakul, PW May, and B Paosawatyanyong. Electrical and optical properties of diamond-like carbon films deposited by pulsed laser ablation. *Diamond and Related Materials*, 19(7-9):999–1002, 2010.

[82] Richard P Mildren et al. Intrinsic optical properties of diamond. *Optical Engineering of Diamond*, 1:1–34, 2013.

[83] LS Hounsome, R Jones, PM Martineau, MJ Shaw, PR Briddon, Sven Öberg, AT Blumenau, and N Fujita. Optical properties of vacancy related defects in diamond. *physica status solidi (a)*, 202(11):2182–2187, 2005.

[84] Huimin Liu and David S Dandy. *Diamond chemical vapor deposition: nucleation and early growth stages*. Elsevier, 1996.

[85] Simon C Lawson, David Fisher, Damian C Hunt, and Mark E Newton. On the existence of positively charged single-substitutional nitrogen in diamond. *Journal of Physics: Condensed Matter*, 10(27):6171, 1998.

[86] ZZ Liang, H Kanda, X Jia, HA Ma, PW Zhu, Qing-Feng Guan, and CY Zang. Synthesis of diamond with high nitrogen concentration from powder catalyst-c-additive nan3 by hpht. *Carbon*, 44(5):913–917, 2006.

[87] Yoshihiko Takano. Superconductivity in cvd diamond films. *Journal of Physics: Condensed Matter*, 21(25):253201, 2009.

[88] Hisao Kanda, Minoru Akaishi, and Shinobu Yamaoka. Synthesis of diamond with the highest nitrogen concentration. *Diamond and related materials*, 8(8-9):1441–1443, 1999.

[89] C Descamps, D Tromson, MJ Guerrero, C Mer, E Rzepka, M Nesladek, and P Bergonzo. Nitrogen-doped diamond: Thermoluminescence and dosimetric applications. *Diamond and related materials*, 15(4-8):833–837, 2006.

[90] Hammed A Ejalonibu, Gordon E Sarty, and Michael P Bradley. Optimal parameter (s) for the synthesis of nitrogen-vacancy (nv) centres in polycrystalline diamonds at low pressure. *Journal of Materials Science: Materials in Electronics*, 30(11):10369–10382, 2019.

[91] Liangchao Chen, Xinyuan Miao, Hongan Ma, Longsuo Guo, Zhanke Wang, Zhiqiang Yang, Chao Fang, and XiaoPeng Jia. Synthesis and characterization of diamonds with different nitrogen concentrations under high pressure and high temperature conditions. *CrystEngComm*, 20(44):7164–7169, 2018.

[92] Joseph W Haus. *Fundamentals and applications of nanophotonics*. Woodhead Publishing, 2016.

[93] Adam Gali, Maria Fyta, and Efthimios Kaxiras. Ab initio supercell calculations on nitrogen-vacancy center in diamond: Electronic structure and hyperfine tensors. *Physical Review B*, 77(15):155206, 2008.

[94] Haimei Zhang, Carina Belvin, Wanyi Li, Jennifer Wang, Julia Wainwright, Robbie Berg, and Joshua Bridger. Little bits of diamond: Optically detected magnetic resonance of nitrogen-vacancy centers. *American Journal of Physics*, 86(3):225–236, 2018.

[95] Paul Delaney, James C Greer, and J Andreas Larsson. Spin-polarization mechanisms of the nitrogen-vacancy center in diamond. *Nano letters*, 10(2):610–614, 2010.

[96] Marcus W Doherty, Neil B Manson, Paul Delaney, and Lloyd CL Hollenberg. The negatively charged nitrogen-vacancy centre in diamond: the electronic solution. *New Journal of Physics*, 13(2):025019, 2011.

[97] Jeronimo R Maze, Adam Gali, Emre Togan, Yiwen Chu, Alexei Trifonov, Efthimios Kaxiras, and Mikhail D Lukin. Properties of nitrogen-vacancy centers in diamond: the group theoretic approach. *New Journal of Physics*, 13(2):025025, 2011.

[98] Kasper Jensen, Pauli Kehayias, and Dmitry Budker. Magnetometry with nitrogen-vacancy centers in diamond. In *High sensitivity magnetometers*, pages 553–576. Springer, 2017.

[99] Lucio Robledo, Hannes Bernien, Toeno Van Der Sar, and Ronald Hanson. Spin dynamics in the optical cycle of single nitrogen-vacancy centres in diamond. *New Journal of Physics*, 13(2):025013, 2011.

[100] JP Tetienne, L Rondin, P Spinicelli, M Chipaux, T Debuisschert, JF Roch, and V Jacques. Magnetic-field-dependent photodynamics of single nv defects in diamond: an application to qualitative all-optical magnetic imaging. *New Journal of Physics*, 14(10):103033, 2012.

[101] Kevin Kai Chang. *Scanning magnetometry with NV centers in diamond*. PhD thesis, ETH Zurich, 2016.

[102] A Jarmola, VM Acosta, K Jensen, S Chemerisov, and D Budker. Temperature-and magnetic-field-dependent longitudinal spin relaxation in nitrogen-vacancy ensembles in diamond. *Physical review letters*, 108(19):197601, 2012.

[103] DA Redman, S Brown, RH Sands, and SC Rand. Spin dynamics and electronic states of n-v centers in diamond by epr and four-wave-mixing spectroscopy. *Physical review letters*, 67(24):3420, 1991.

[104] Boris Naydenov, Florian Dolde, Liam T Hall, Chang Shin, Helmut Fedder, Lloyd CL Hollenberg, Fedor Jelezko, and Jörg Wrachtrup. Dynamical decoupling of a single-electron spin at room temperature. *Physical Review B*, 83(8):081201, 2011.

[105] Linh My Pham, David Le Sage, Paul L Stanwix, Tsun Kwan Yeung, D Glenn, Alexei Trifonov, Paola Cappellaro, Philip R Hemmer, Mikhail D Lukin, Hongkun Park, et al. Magnetic field imaging with nitrogen-vacancy ensembles. *New Journal of Physics*, 13(4):045021, 2011.

[106] Michael Loretz, JM Boss, Tobias Rosskopf, HJ Mamin, D Rugar, and Christian L Degen. Spurious harmonic response of multipulse quantum sensing sequences. *Physical Review X*, 5(2):021009, 2015.

[107] ED Herbschleb, H Kato, Y Maruyama, T Danjo, T Makino, S Yamasaki, I Ohki, K Hayashi, H Morishita, M Fujiwara, et al. Ultra-long coherence times amongst room-temperature solid-state spins. *Nature communications*, 10(1):1–6, 2019.

[108] Fedor Jelezko and Jörg Wrachtrup. Single defect centres in diamond: A review. *physica status solidi (a)*, 203(13):3207–3225, 2006.

[109] Romana Schirhagl, Kevin Chang, Michael Loretz, and Christian L Degen. Nitrogen-vacancy centers in diamond: nanoscale sensors for physics and biology. *Annual review of physical chemistry*, 65:83–105, 2014.

[110] Eric Van Oort and Max Glasbeek. Electric-field-induced modulation of spin echoes of nv centers in diamond. *Chemical Physics Letters*, 168(6):529–532, 1990.

[111] Jocelyn Achard, Vincent Jacques, and Alexandre Tallaire. Cvd diamond single crystals with nv centres: a review of material synthesis and technology for quantum sensing applications. *Journal of Physics D: Applied Physics*, 2020.

[112] Y Romach, C Müller, T Unden, LJ Rogers, T Isoda, Kohei M Itoh, M Markham, A Stacey, J Meijer, S Pezzagna, et al. Spectroscopy of surface-induced noise using shallow spins in diamond. *Physical review letters*, 114(1):017601, 2015.

[113] Moloud Kaviani, Peter Deak, Balint Aradi, Thomas Frauenheim, Jyh-Pin Chou, and Adam Gali. Proper surface termination for luminescent near-surface nv centers in diamond. *Nano letters*, 14(8):4772–4777, 2014.

[114] Sora Kawai, Hayate Yamano, Takahiro Sonoda, Kanami Kato, Jorge J Buendia, Taisuke Kageura, Ryosuke Fukuda, Takuma Okada, Takashi Tanii, Taisei Higuchi, et al. Nitrogen-terminated diamond surface for nanoscale nmr by shallow nitrogen-vacancy centers. *The Journal of Physical Chemistry C*, 123(6):3594–3604, 2019.

[115] Ch Schreyvogel, V Polyakov, R Wunderlich, J Meijer, and CE Nebel. Active charge state control of single nv centres in diamond by in-plane al-schottky junctions. *Scientific reports*, 5(1):1–12, 2015.

[116] Jens M Boss, KS Cujia, Jonathan Zopes, and Christian L Degen. Quantum sensing with arbitrary frequency resolution. *Science*, 356(6340):837–840, 2017.

[117] Christian Osterkamp, Martin Mangold, Johannes Lang, Priyadharshini Balasubramanian, Tokuyuki Teraji, Boris Naydenov, and Fedor Jelezko. Engineering preferentially-aligned nitrogen-vacancy centre ensembles in cvd grown diamond. *Scientific reports*, 9(1):1–7, 2019.

[118] M Lesik, T Plays, A Tallaire, J Achard, O Brinza, L William, M Chipaux, L Toraille, T Debuisschert, A Gicquel, et al. Preferential orientation of nv defects in cvd diamond films grown on (113)-oriented substrates. *Diamond and Related Materials*, 56:47–53, 2015.

[119] M Capelli, AH Heffernan, T Ohshima, H Abe, J Jeske, A Hope, AD Greentree, P Reineck, and BC Gibson. Increased nitrogen-vacancy centre creation yield in diamond through electron beam irradiation at high temperature. *Carbon*, 143:714–719, 2019.

[120] Tobias Nöbauer, Kathrin Buczak, Andreas Angerer, Stefan Putz, Georg Steinhauser, Johanna Akbarzadeh, Herwig Peterlik, Johannes Majer, Jörg Schmiedmayer, and Michael Trupke. Creation of ensembles of nitrogen-vacancy centers in diamond by neutron and electron irradiation. *arXiv preprint arXiv:1309.0453*, 2013.

[121] Anna Maria Ferrari, Simone Salustro, Francesco Silvio Gentile, William C Mackrodt, and Roberto Dovesi. Substitutional nitrogen in diamond: A quantum mechanical investigation of the electronic and spectroscopic properties. *Carbon*, 134:354–365, 2018.

[122] FC Waldermann, Paolo Olivero, J Nunn, K Surmacz, ZY Wang, D Jaksch, RA Taylor, IA Walmsley, M Draganski, P Reichart, et al. Creating diamond color centers for quantum optical applications. *Diamond and Related Materials*, 16(11):1887–1895, 2007.

[123] JO Orwa, AD Greentree, I Aharonovich, ADC Alves, J Van Donkelaar, A Stacey, and S Prawer. Fabrication of single optical centres in diamond—a review. *Journal of luminescence*, 130(9):1646–1654, 2010.

[124] Edwin Kim, Victor M Acosta, Erik Bauch, Dmitry Budker, and Philip R Hemmer. Electron spin resonance shift and linewidth broadening of nitrogen-vacancy centers in diamond as a function of electron irradiation dose. *Applied physics letters*, 101(8):082410, 2012.

[125] A Jarmola, A Berzins, J Smits, K Smits, J Prikulis, F Gahbauer, R Ferber, D Erts, M Auzinsh, and D Budker. Longitudinal spin-relaxation in nitrogen-vacancy centers in electron irradiated diamond. *Applied Physics Letters*, 107(24):242403, 2015.

[126] Moriyoshi Haruyama, Shinobu Onoda, Taisei Higuchi, Wataru Kada, Atsuya Chiba, Yoshimi Hirano, Tokuyuki Teraji, Ryuji Igarashi, Sora Kawai, Hiroshi Kawarada, et al. Triple nitrogen-vacancy centre fabrication by c 5 n 4 h n ion implantation. *Nature communications*, 10(1):1–9, 2019.

[127] Roman A Khmelnitsky, Valeriy A Dravin, Alexey A Tal, Evgeniy V Zavedeev, Andrey A Khomich, Alexander V Khomich, Alexander A Alekseev, and Sergey A Terentiev. Damage accumulation in diamond during ion implantation. *Journal of Materials Research*, 30(9):1583–1592, 2015.

[128] Ariful Haque and Sharaf Sumaiya. An overview on the formation and processing of nitrogen-vacancy photonic centers in diamond by ion implantation. *Journal of Manufacturing and Materials Processing*, 1(1):6, 2017.

[129] JR Rabeau, Patrick Reichart, Grigori Tamanyan, DN Jamieson, Steven Prawer, Fedor Jelezko, Torsten Gaebel, Iulian Popa, Michael Domhan, and J Wrachtrup. Implantation of labelled single nitrogen vacancy centers in diamond using n 15. *Applied Physics Letters*, 88(2):023113, 2006.

[130] T Yamamoto, T Umeda, K Watanabe, S Onoda, ML Markham, DJ Twitchen, B Naydenov, LP McGuinness, T Teraji, S Koizumi, et al. Extending spin coherence times of diamond qubits by high-temperature annealing. *Physical Review B*, 88(7):075206, 2013.

[131] Boris Naydenov, Friedemann Reinhard, Anke Lämmle, V Richter, Rafi Kalish, Ulrika FS D'Haenens-Johansson, Mark Newton, Fedor Jelezko, and Jörg Wrachtrup. Increasing the coherence time of single electron spins in diamond by high temperature annealing. *Applied Physics Letters*, 97(24):242511, 2010.

[132] T Staudacher, F Ziem, L Häussler, R Stöhr, S Steinert, F Reinhard, J Scharpf, A Denisenko, and J Wrachtrup. Enhancing the spin properties of shallow implanted nitrogen vacancy centers in diamond by epitaxial overgrowth. *Applied Physics Letters*, 101(21):212401, 2012.

[133] Jianhua Wang Jun Weng Sun, Qi and Fan Liu. Surface structure and electric properties of nitrogen incorporated ncd films. *Vacuum*, 137:155–162, 2017.

[134] David G Goodwin. Scaling laws for diamond chemical-vapor deposition. i. diamond surface chemistry. *Journal of Applied Physics*, 74(11):6888–6894, 1993.

[135] Toyofumi Ishikawa, Kai-Mei C Fu, Charles Santori, Victor M Acosta, Raymond G Beausoleil, Hideyuki Watanabe, Shinichi Shikata, and Kohei M Itoh. Optical and spin coherence properties of nitrogen-vacancy centers placed in a 100 nm thick isotopically purified diamond layer. *Nano letters*, 12(4):2083–2087, 2012.

[136] Robert G Ryan, Alastair Stacey, Kane M O'Donnell, Takeshi Ohshima, Brett C Johnson, Lloyd CL Hollenberg, Paul Mulvaney, and David A Simpson. Impact of surface functionalization on the quantum coherence of nitrogen-vacancy centers in nanodiamonds. *ACS applied materials & interfaces*, 10(15):13143–13149, 2018.

[137] Julia Michl, Tokuyuki Teraji, Sebastian Zaiser, Ingmar Jakobi, Gerald Waldherr, Florian Dolde, Philipp Neumann, Marcus W Doherty, Neil B Manson, Junichi Isoya, et al. Perfect alignment and preferential orientation of nitrogen-vacancy centers during chemical vapor deposition diamond growth on (111) surfaces. *Applied Physics Letters*, 104(10):102407, 2014.

[138] Hitoshi Ishiwata, Makoto Nakajima, Kosuke Tahara, Hayato Ozawa, Takayuki Iwasaki, and Mutsuko Hatano. Perfectly aligned shallow ensemble nitrogen-vacancy centers in (111) diamond. *Applied Physics Letters*, 111(4):043103, 2017.

[139] Marcus W Doherty, Neil B Manson, Paul Delaney, Fedor Jelezko, Jörg Wrachtrup, and Lloyd CL Hollenberg. The nitrogen-vacancy colour centre in diamond. *Physics Reports*, 528(1):1–45, 2013.

[140] Soumen Mandal. Nucleation of diamond films on heterogeneous substrates: a review. *RSC Advances*, 11(17):10159–10182, 2021.

[141] Cvd-based reactors. *https://www.plasmionique.com/cvd-mocvd-horizontal-furnace*, 1999.

[142] Steven Prawer and Robert J Nemanich. Raman spectroscopy of diamond and doped diamond. *Philosophical Transactions of the Royal Society of London A: Mathematical, Physical and Engineering Sciences*, 362(1824):2537–2565, 2004.

[143] Andrea Carlo Ferrari and John Robertson. Raman spectroscopy of amorphous, nanostructured, diamond–like carbon, and nanodiamond. *Philosophical Transactions of the Royal Society of London A: Mathematical, Physical and Engineering Sciences*, 362(1824):2477–2512, 2004.

[144] Lucky Krishnia and Pawan K Tyagi. Growth and characterization of polycrystalline diamond films on silicon using sugarcane bagasse as carbon precursor at atmospheric pressure by thermal chemical vapor deposition. *Diamond and Related Materials*, 87:18–26, 2018.

[145] Kalyan S Pal, Awadesh K Mallik, Nandadulal Dandapat, Nihar R Ray, Someswar Datta, Sandip Bysakh, and Bichitra K Guha. Microscopic properties of mpcvd diamond coatings studied by micro-raman and micro-photoluminescence spectroscopy. *Bulletin of Materials Science*, 38(2):537–549, 2015.

[146] LG Cançado, K Takai, T Enoki, M Endo, YA Kim, H Mizusaki, A Jorio, LN Coelho, R Magalhaes-Paniago, and MA Pimenta. General equation for the determination of the crystallite size l a of nanographite by raman spectroscopy. *Applied Physics Letters*, 88(16):163106, 2006.

[147] Robert E Clausing, MA Prelas, G Popovici, and LK Bigelow. Diamond morphology. *Handbook of industrial diamonds and diamond films, Marcel Dekker, New York*, pages 19–48, 1997.

[148] MA Lobaev, AM Gorbachev, SA Bogdanov, AL Vikharev, DB Radishev, VA Isaev, VV Chernov, and MN Drozdov. Influence of cvd diamond growth conditions on nitrogen incorporation. *Diamond and Related Materials*, 72:1–6, 2017.

[149] Hideyuki Watanabe, Hitoshi Umezawa, Toyofumi Ishikawa, Kazuki Kaneko, Shinichi Shikata, Junko Ishi-Hayase, and Kohei M Itoh. Formation of nitrogen-vacancy centers in homoepitaxial diamond thin films grown via microwave plasma-assisted chemical vapor deposition. *IEEE Transactions on Nanotechnology*, 15(4):614–618, 2016.

[150] Adam M Wojciechowski, Mürsel Karadas, Alexander Huck, Christian Osterkamp, Steffen Jankuhn, Jan Meijer, Fedor Jelezko, and Ulrik L Andersen. Contributed review: Camera-limits for wide-field magnetic resonance imaging with a nitrogen-vacancy spin sensor. *Review of Scientific Instruments*, 89(3):031501, 2018.

[151] JX Yang, CM Li, FX Lu, GC Chen, WZ Tang, and YM Tong. Microstructure and fracture strength of different grades of freestanding diamond films deposited by a dc arc plasma jet process. *Surface and Coatings Technology*, 192(2-3):171–176, 2005.

[152] JX Yang, XF Duan, FX Lu, CM Li, TC Zuo, and FL Wang. The influence of dark feature on optical and thermal property of dc arc plasma jet cvd diamond films. *Diamond and related materials*, 14(10):1583–1587, 2005.

[153] James Birrell, JA Carlisle, O Auciello, DM Gruen, and JM Gibson. Morphology and electronic structure in nitrogen-doped ultrananocrystalline diamond. *Applied physics letters*, 81(12):2235–2237, 2002.

[154] Peter Zapol, Michael Sternberg, Larry A Curtiss, Thomas Frauenheim, and Dieter M Gruen. Tight-binding molecular-dynamics simulation of impurities in ultrananocrystalline diamond grain boundaries. *Physical Review B*, 65(4):045403, 2001.

[155] Kenichi Ohno, F Joseph Heremans, Lee C Bassett, Bryan A Myers, David M Toyli, Ania C Bleszynski Jayich, Christopher J Palmstrøm, and David D Awschalom. Engineering shallow spins in diamond with nitrogen delta-doping. *Applied Physics Letters*, 101(8):082413, 2012.

[156] CM Yap, K Ansari, S Xiao, SY Yee, R Chukka, and DS Misra. Properties of near-colourless lightly boron doped cvd diamond. *Diamond and Related Materials*, 88:118–122, 2018.

[157] Bingmin Yan, Xiaopeng Jia, Chao Fang, Ning Chen, Yadong Li, Shishuai Sun, and Hong-An Ma. The effect of phosphorus and nitrogen co-doped on the synthesis of diamond at high pressure and high temperature. *International Journal of Refractory Metals and Hard Materials*, 54:309–314, 2016.

[158] Jagdish Narayan and Anagh Bhaumik. Novel synthesis and properties of pure and nv-doped nanodiamonds and other nanostructures. *Materials Research Letters*, 5(4):242–250, 2017.

[159] Tingting Gu and Wuyi Wang. Optical defects in milky type iab diamonds. *Diamond and Related Materials*, 89:322–329, 2018.

[160] Charles Santori, Paul E Barclay, Kai-Mei C Fu, and Raymond G Beausoleil. Vertical distribution of nitrogen-vacancy centers in diamond formed by ion implantation and annealing. *Physical Review B*, 79(12):125313, 2009.

[161] J Ristein. Electronic properties of diamond surfaces—blessing or curse for devices? *Diamond and Related Materials*, 9(3-6):1129–1137, 2000.

[162] MV Hauf, B Grotz, B Naydenov, M Dankerl, S Pezzagna, J Meijer, F Jelezko, J Wrachtrup, M Stutzmann, FJPRB Reinhard, et al. Chemical control of the charge state of nitrogen-vacancy centers in diamond. *Physical Review B*, 83(8):081304, 2011.

[163] K-MC Fu, C Santori, PE Barclay, and RG Beausoleil. Conversion of neutral nitrogen-vacancy centers to negatively charged nitrogen-vacancy centers through selective oxidation. *Applied Physics Letters*, 96(12):121907, 2010.

[164] Alastair Stacey, Igor Aharonovich, Steven Prawer, and James E Butler. Controlled synthesis of high quality micro/nano-diamonds by microwave plasma chemical vapor deposition. *Diamond and related materials*, 18(1):51–55, 2009.

[165] Wolfgang Jacob, Achim von Keudell, and Thomas Schwarz-Selinger. Infrared analysis of thin films: amorphous, hydrogenated carbon on silicon. *Brazilian Journal of Physics*, 30(3):508–516, 2000.

[166] Yuri V Shvyd'ko, Stanislav Stoupin, Alessandro Cunsolo, Ayman H Said, and Xianrong Huang. High-reflectivity high-resolution x-ray crystal optics with diamonds. *Nature Physics*, 6(3):196–199, 2010.

[167] Christopher D Zuiker, Dieter M Gruen, and Alan R Krauss. In situ laser reflectance interferometry measurement of diamond film growth. *Journal of Applied Physics*, 79(7):3541–3547, 1996.

[168] AM Zaitsev, KS Moe, and W Wang. Defect transformations in nitrogen-doped cvd diamond during irradiation and annealing. *Diamond and Related Materials*, 88:237–255, 2018.

[169] S Bhattacharyya, O Auciello, J Birrell, JA Carlisle, LA Curtiss, AN Goyette, DM Gruen, AR Krauss, J Schlueter, A Sumant, et al. Synthesis and characterization of highly-conducting nitrogen-doped ultrananocrystalline diamond films. *Applied Physics Letters*, 79(10):1441–1443, 2001.

[170] Masato Tsuchiya, Kazuki Murakami, Kohei Magara, Kazuki Nakamura, Haruka Ohashi, Kengo Tokuda, Takahiro Takami, Haruka Ogasawara, Yoshiharu Enta, Yushi Suzuki, et al. Structural and electrical properties and current–voltage characteristics of

nitrogen-doped diamond-like carbon films on si substrates by plasma-enhanced chemical vapor deposition. *Japanese Journal of Applied Physics*, 55(6):065502, 2016.

[171] C Bradac, T Gaebel, N Naidoo, MJ Sellars, J Twamley, LJ Brown, AS Barnard, T Plakhotnik, AV Zvyagin, and JR Rabeau. Observation and control of blinking nitrogen-vacancy centres in discrete nanodiamonds. *Nature nanotechnology*, 5(5):345–349, 2010.

[172] Sean Lourette, Lykourgos Bougas, Metin Kayci, Shoujun Xu, and Dmitry Budker. Noncovalent force spectroscopy using wide-field optical and diamond-based magnetic imaging. *Journal of Applied Physics*, 126(19):194502, 2019.

[173] Huijie Zheng, Jingyan Xu, Geoffrey Z Iwata, Till Lenz, Julia Michl, Boris Yavkin, Kazuo Nakamura, Hitoshi Sumiya, Takeshi Ohshima, Junichi Isoya, et al. Zero-field magnetometry based on nitrogen-vacancy ensembles in diamond. *Physical Review Applied*, 11(6):064068, 2019.

[174] G Liaugaudas, G Davies, K Suhling, RUA Khan, and DJF Evans. Luminescence lifetimes of neutral nitrogen-vacancy centres in synthetic diamond containing nitrogen. *Journal of Physics: Condensed Matter*, 24(43):435503, 2012.

[175] A Stacey, TJ Karle, LP McGuinness, BC Gibson, K Ganesan, S Tomljenovic-Hanic, AD Greentree, A Hoffman, RG Beausoleil, and S Prawer. Depletion of nitrogen-vacancy color centers in diamond via hydrogen passivation. *Applied Physics Letters*, 100(7):071902, 2012.

[176] Ingrid De Wolf. Micro-raman spectroscopy to study local mechanical stress in silicon integrated circuits. *Semiconductor science and technology*, 11(2):139, 1996.

[177] Deepak Kallepalli Lakshmi Narayana, Soma Venugopal Rao, and Desai Narayana Rao. Spectroscopic investigation of fs laser-induced defects in polymer and crystal media. In *Laser-Induced Damage in Optical Materials: 2012*, volume 8530, page 853004. International Society for Optics and Photonics, 2012.

[178] Andrea C Ferrari and John Robertson. Interpretation of raman spectra of disordered and amorphous carbon. *Physical review B*, 61(20):14095, 2000.

[179] Grzegorz Greczynski and Lars Hultman. X-ray photoelectron spectroscopy: towards reliable binding energy referencing. *Progress in Materials Science*, 107:100591, 2020.

[180] Vladimir Yu Osipov, François Treussart, Soroush Abbasi Zargaleh, Kazuyuki Takai, Fedor M Shakhov, Benjamin T Hogan, and Anna Baldycheva. Photoluminescence from nv- centres in 5 nm detonation nanodiamonds: identification and high sensitivity to magnetic field. *Nanoscale research letters*, 14(1):1–14, 2019.

[181] Hong-Quan Zhao, Masazumi Fujiwara, and Shigeki Takeuchi. Suppression of phonon sidebands in the spectrum of nitrogen vacancy centers in diamond nano-crystals. In *Advances in Photonics of Quantum Computing, Memory, and Communication V*, volume 8272, page 82720W. International Society for Optics and Photonics, 2012.

[182] Yangming Lin, Xiaoyan Sun, Dang Sheng Su, Gabriele Centi, and Siglinda Perathoner. Catalysis by hybrid sp 2/sp 3 nanodiamonds and their role in the design of advanced nanocarbon materials. *Chemical Society Reviews*, 47(22):8438–8473, 2018.

[183] Markus Mohr, Layal Daccache, Sebastian Horvat, Kai Brühne, Timo Jacob, and Hans-Jörg Fecht. Influence of grain boundaries on elasticity and thermal conductivity of nanocrystalline diamond films. *Acta Materialia*, 122:92–98, 2017.

[184] Josephus G Buijnsters, Menelaos Tsigkourakos, Thomas Hantschel, Francis OV Gomes, Thomas Nuytten, Paola Favia, Hugo Bender, Kai Arstila, Jean-Pierre Celis, and Wilfried Vandervorst. Effect of boron doping on the wear behavior of the growth and nucleation surfaces of micro-and nanocrystalline diamond films. *ACS applied materials & interfaces*, 8(39):26381–26391, 2016.

[185] Grzegorz W Bak, Kazimierz Fabisiak, Leszek Klimek, Marcin Kozanecki, and Elżbieta Staryga. Investigation of biaxial stresses in diamond films deposited on a silicon substrate by the hf cvd method. *Optical Materials*, 30(5):770–773, 2008.

[186] Stephanie R Sails, Derek J Gardiner, Michael Bowden, James Savage, and Don Rodway. Monitoring the quality of diamond films using raman spectra excited at 514.5 nm and 633 nm. *Diamond and Related Materials*, 5(6-8):589–591, 1996.

[187] CFARJ Casiraghi, AC Ferrari, and J Robertson. Raman spectroscopy of hydrogenated amorphous carbons. *Physical Review B*, 72(8):085401, 2005.

[188] AC Ferrari and J Robertson. Origin of the 1 1 5 0- cm- 1 raman mode in nanocrystalline diamond. *Physical review B*, 63(12):121405, 2001.

[189] Laia Ginés, Soumen Mandal, Chia-Liang Cheng, Maabur Sow, Oliver A Williams, et al. Positive zeta potential of nanodiamonds. *Nanoscale*, 9(34):12549–12555, 2017.

[190] CL He, WJ Zong, ZM Cao, and T Sun. Theoretical and empirical coupled modeling on the surface roughness in diamond turning. *Materials & Design*, 82:216–222, 2015.

[191] E Clayton Teague, Theodore V Vorburger, Daniel Maystre, and RD Young. Light scattering from manufactured surfaces. *CIRP Annals*, 30(2):563–569, 1981.

[192] AI Gusev and AS Kurlov. Production of nanocrystalline powders by high-energy ball milling: model and experiment. *Nanotechnology*, 19(26):265302, 2008.

[193] Shreya Nad, Amanda Charris, and Jes Asmussen. Mpacvd growth of single crystalline diamond substrates with pcd rimless and expanding surfaces. *Applied Physics Letters*, 109(16):162103, 2016.

[194] Diane S Knight and William B White. Characterization of diamond films by raman spectroscopy. *Journal of Materials Research*, 4(2):385–393, 1989.

[195] Mohan Kumar Kuntumalla, Sergey Elfimchev, Maneesh Chandran, and Alon Hoffman. Raman scattering of nitrogen incorporated diamond thin films grown by hot filament chemical vapor deposition. *Thin Solid Films*, 653:284–292, 2018.

[196] Vitor Baranauskas, Steven F Durrant, Marcelo C Tosin, Alfredo C Peterlevitz, Bin Bin Li, and Sandra G Castro. Nitrogenated diamond produced by introducing ammonia into the gas feed in hot-filament cvd. *Thin Solid Films*, 355:157–161, 1999.

[197] L Bergman, MT McClure, JT Glass, and RJ Nemanich. The origin of the broadband luminescence and the effect of nitrogen doping on the optical properties of diamond films. *Journal of applied physics*, 76(5):3020–3027, 1994.

[198] M Park, AT Sowers, C Lizzul Rinne, R Schlesser, L Bergman, RJ Nemanich, Z Sitar, JJ Hren, JJ Cuomo, VV Zhirnov, et al. Effect of nitrogen incorporation on electron emission from chemical vapor deposited diamond. *Journal of Vacuum Science & Technology B: Microelectronics and Nanometer Structures Processing, Measurement, and Phenomena*, 17(2):734–739, 1999.

[199] LC Nistor, J Van Landuyt, Victor G Ralchenko, ED Obraztsova, and AA Smolin. Nanocrystalline diamond films: transmission electron microscopy and raman spectroscopy characterization. *Diamond and Related Materials*, 6(1):159–168, 1997.

[200] Sh Cherf, M Chandran, Sh Michaelson, S Elfimchev, R Akhvlediani, and A Hoffman. Nitrogen and hydrogen content, morphology and phase composition of hot filament chemical vapor deposited diamond films from nh3/ch4/h2 gas mixtures. *Thin Solid Films*, 638:264–268, 2017.

[201] JR Rabeau, P John, JIB Wilson, and Y Fan. The role of c 2 in nanocrystalline diamond growth. *Journal of Applied Physics*, 96(11):6724–6732, 2004.

[202] Z Yiming, F Larsson, and Karin Larsson. Effect of cvd diamond growth by doping with nitrogen. *Theoretical Chemistry Accounts*, 133(2):1432, 2014.

[203] James Birrell, JE Gerbi, O Auciello, JM Gibson, DM Gruen, and JA Carlisle. Bonding structure in nitrogen doped ultrananocrystalline diamond. *Journal of Applied Physics*, 93(9):5606–5612, 2003.

[204] P Achatz, JA Garrido, M Stutzmann, Oliver Aneurin Williams, DM Gruen, A Kromka, and D Steinmüller. Optical properties of nanocrystalline diamond thin films. *Applied Physics Letters*, 88(10):101908, 2006.

[205] Tomohiro Ikeda, Kungen Teii, C Casiraghi, J Robertson, and AC Ferrari. Effect of the sp 2 carbon phase on n-type conduction in nanodiamond films. *Journal of Applied Physics*, 104(7):073720, 2008.

[206] CJ Tang, AJS Fernandes, Marco Granada, JP Leitao, S Pereira, XF Jiang, JL Pinto, and H Ye. High rate growth of nanocrystalline diamond films using high microwave power and pure nitrogen/methane/hydrogen plasma. *Vacuum*, 122:342–346, 2015.

[207] G Cicala, V Magaletti, GS Senesi, G Carbone, D Altamura, C Giannini, and Ruben Bartali. Superior hardness and young's modulus of low temperature nanocrystalline diamond coatings. *Materials Chemistry and Physics*, 144(3):505–511, 2014.

[208] AV Novak and VR Novak. Roughness of amorphous, polycrystalline and hemispherical-grained silicon films. *Technical Physics Letters*, 39(10):858–861, 2013.

[209] Xinyi Jia, Nan Huang, Yuning Guo, Lusheng Liu, Peng Li, Zhaofeng Zhai, Bing Yang, Ziyao Yuan, Dan Shi, and Xin Jiang. Growth behavior of cvd diamond films with enhanced electron field emission properties over a wide range of experimental parameters. *Journal of Materials Science & Technology*, 34(12):2398–2406, 2018.

[210] Elina A Vitol, Valentyn Novosad, and Elena A Rozhkova. Microfabricated magnetic structures for future medicine: from sensors to cell actuators. *Nanomedicine*, 7(10):1611–1624, 2012.

[211] Levin Sliker, Gastone Ciuti, Mark Rentschler, and Arianna Menciassi. Magnetically driven medical devices: a review. *Expert review of medical devices*, 12(6):737–752, 2015.

[212] Gordon E Sarty and Logi Vidarsson. Magnetic resonance imaging with rf encoding on curved natural slices. *Magnetic resonance imaging*, 46:47–55, 2018.

[213] Felix M Stürner, Andreas Brenneis, Julian Kassel, Uwe Wostradowski, Robert Roelver, Tino Fuchs, Kazuo Nakamura, Hitoshi Sumiya, Shinobu Onoda, Junichi Isoya, et al. Compact integrated magnetometer based on nitrogen-vacancy centres in diamond. *Diamond and Related Materials*, 93:59–65, 2019.

[214] James L Webb, Joshua D Clement, Luca Troise, Sepehr Ahmadi, Gustav Juhl Johansen, Alexander Huck, and Ulrik L Andersen. Nanotesla sensitivity magnetic field sensing using a compact diamond nitrogen-vacancy magnetometer. *Applied Physics Letters*, 114(23):231103, 2019.

[215] Ji-Hu Zhang, Thomas DY Chung, and Kevin R Oldenburg. A simple statistical parameter for use in evaluation and validation of high throughput screening assays. *Journal of biomolecular screening*, 4(2):67–73, 1999.

[216] James L Webb, Luca Troise, Nikolaj W Hansen, Jocelyn Achard, Ovidiu Brinza, Robert Staacke, Michael Kieschnick, Jan Meijer, Jean-François Perrier, Kirstine Berg-Sørensen, et al. Optimization of a diamond nitrogen vacancy centre magnetometer for sensing of biological signals. *Frontiers in Physics*, 8:430, 2020.

[217] Daiki Misonou, Kento Sasaki, Shuntaro Ishizu, Yasuaki Monnai, Kohei M Itoh, and Eisuke Abe. Construction and operation of a tabletop system for nanoscale magnetometry with single nitrogen-vacancy centers in diamond. *AIP Advances*, 10(2):025206, 2020.

[218] An-Chi Wei and Han-Ping D Shieh. Design and analyses of a planar zoom module as a beam expander. *Japanese journal of applied physics*, 43(8S):5752, 2004.

[219] Philipp J Keller, Annette D Schmidt, Anthony Santella, Khaled Khairy, Zhirong Bao, Joachim Wittbrodt, and Ernst HK Stelzer. Fast, high-contrast imaging of animal development with scanned light sheet–based structured-illumination microscopy. *Nature methods*, 7(8):637–642, 2010.

[220] Jan Huisken, Jim Swoger, Filippo Del Bene, Joachim Wittbrodt, and Ernst HK Stelzer. Optical sectioning deep inside live embryos by selective plane illumination microscopy. *Science*, 305(5686):1007–1009, 2004.

[221] AJ Gatesman, J Waldman, M Ji, C Musante, and S Yagvesson. An anti-reflection coating for silicon optics at terahertz frequencies. *IEEE microwave and guided wave letters*, 10(7):264–266, 2000.

[222] I Abdulhalim, Ron Friedman, Lior Liraz, and Ronen Dadon. Full field frequency domain common path optical coherence tomography with annular aperture. In *European Conference on Biomedical Optics*, page 6627_58. Optical Society of America, 2007.

[223] Jianhua Mo, Mattijs de Groot, and Johannes F de Boer. Focus-extension by depth-encoded synthetic aperture in optical coherence tomography. *Optics express*, 21(8):10048–10061, 2013.

[224] Eisuke Abe and Kento Sasaki. Tutorial: Magnetic resonance with nitrogen-vacancy centers in diamond—microwave engineering, materials science, and magnetometry. *Journal of Applied Physics*, 123(16):161101, 2018.

[225] Khadijeh Bayat, Jennifer Choy, Mahdi Farrokh Baroughi, Srujan Meesala, and Marko Loncar. Efficient, uniform, and large area microwave magnetic coupling to nv centers in diamond using double split-ring resonators. *Nano letters*, 14(3):1208–1213, 2014.

[226] Héctor Solar, Roc Berenguer, Joaquín de No, Iñaki Gurutzeaga, Unai Alvarado, and Jon Legarda. A fully integrated 23.2 dbm p1 db cmos power amplifier for the ieee 802.11 a with 29% pae. *Integration*, 42(1):77–82, 2009.

[227] Christopher J Hasselwander, Zhipeng Cao, and William A Grissom. gr-mri: A software package for magnetic resonance imaging using software defined radios. *Journal of Magnetic Resonance*, 270:47–55, 2016.

[228] E Wang, CM Babbey, and Kenneth W Dunn. Performance comparison between the high-speed yokogawa spinning disc confocal system and single-point scanning confocal systems. *Journal of microscopy*, 218(2):148–159, 2005.

[229] Susanne Beater, Mario Raab, and Philip Tinnefeld. Toward quantitative fluorescence microscopy with dna origami nanorulers. *Methods in cell biology*, 123:449–466, 2014.

[230] Alexia Ferrand, Kai D Schleicher, Nikolaus Ehrenfeuchter, Wolf Heusermann, and Oliver Biehlmaier. Using the noisee workflow to measure signal-to-noise ratios of confocal microscopes. *Scientific reports*, 9(1):1–12, 2019.

[231] Giulia De Luca, Ronald Breedijk, Ron Hoebe, Sjoerd Stallinga, and Erik Manders. Re-scan confocal microscopy (rcm) improves the resolution of confocal microscopy and increases the sensitivity. *Methods and applications in fluorescence*, 5(1):015002, 2017.

[232] Denis G Pelli and Peter Bex. Measuring contrast sensitivity. *Vision research*, 90:10–14, 2013.

[233] LT Hall, GCG Beart, EA Thomas, DA Simpson, LP McGuinness, JH Cole, JH Manton, RE Scholten, Fedor Jelezko, Jörg Wrachtrup, et al. High spatial and temporal resolution wide-field imaging of neuron activity using quantum nv-diamond. *Scientific reports*, 2(1):1–9, 2012.

[234] K Jensen, VM Acosta, A Jarmola, and D Budker. Light narrowing of magnetic resonances in ensembles of nitrogen-vacancy centers in diamond. *Physical Review B*, 87(1):014115, 2013.

[235] A Dréau, M Lesik, L Rondin, P Spinicelli, O Arcizet, J-F Roch, and V Jacques. Avoiding power broadening in optically detected magnetic resonance of single nv defects for enhanced dc magnetic field sensitivity. *Physical Review B*, 84(19):195204, 2011.

[236] Zhenyu Wang, Jorge Casanova, and Martin B Plenio. Enhancing the robustness of dynamical decoupling sequences with correlated random phases. *Symmetry*, 12(5):730, 2020.

[237] Maximilian Schlosshauer. Decoherence, the measurement problem, and interpretations of quantum mechanics. *Reviews of Modern physics*, 76(4):1267, 2005.

[238] Maximilian A Schlosshauer. *Decoherence: and the quantum-to-classical transition*. Springer Science & Business Media, 2007.

[239] A Doll. Pulsed and continuous-wave magnetic resonance spectroscopy using a low-cost software-defined radio. *AIP Advances*, 9(11):115110, 2019.

[240] Ngoc Diep Lai, Dingwei Zheng, Fedor Jelezko, François Treussart, and Jean-François Roch. Influence of a static magnetic field on the photoluminescence of an ensemble of nitrogen-vacancy color centers in a diamond single-crystal. *Applied Physics Letters*, 95(13):133101, 2009.

[241] L Botsch, N Raatz, S Pezzagna, R Staacke, R John, B Abel, PD Esquinazi, J Meijer, and S Diziain. Vectorial calibration of superconducting magnets with a quantum magnetic sensor. *Review of Scientific Instruments*, 91(12):125003, 2020.

[242] Loïc Rondin, Jean-Philippe Tetienne, Thomas Hingant, Jean-François Roch, Patrick Maletinsky, and Vincent Jacques. Magnetometry with nitrogen-vacancy defects in diamond. *Reports on progress in physics*, 77(5):056503, 2014.

[243] Mayeul Chipaux, Alexandre Tallaire, Jocelyn Achard, Sébastien Pezzagna, Jan Meijer, Vincent Jacques, Jean-François Roch, and Thierry Debuisschert. Magnetic imaging with an ensemble of nitrogen-vacancy centers in diamond. *The European Physical Journal D*, 69(7):166, 2015.

[244] Somaie Salajeghe et al. *Image Encoding and Reconstruction for Portable Magnetic Resonance Imaging*. PhD thesis, University of Saskatchewan, 2016.

[245] Myeongwon Lee, Bumjin Jang, Jungbae Yoon, Mohan C Mathpal, Yuhan Lee, Chulki Kim, Salvador Pane, Bradley J Nelson, and Donghun Lee. Magnetic imaging of a single

ferromagnetic nanowire using diamond atomic sensors. *Nanotechnology*, 29(40):405502, 2018.

[246] Yang Zhang, Zhonghao Li, Yuanyao Feng, Hao Guo, Huanfei Wen, Jun Tang, and Jun Liu. High-sensitivity dc magnetic field detection with ensemble nv centers by pulsed quantum filtering technology. *Optics express*, 28(11):16191–16201, 2020.

[247] David J Szwer, Simon C Webster, Andrew M Steane, and David M Lucas. Keeping a single qubit alive by experimental dynamic decoupling. *Journal of Physics B: Atomic, Molecular and Optical Physics*, 44(2):025501, 2010.

[248] Götz S Uhrig. Exact results on dynamical decoupling by π pulses in quantum information processes. *New Journal of Physics*, 10(8):083024, 2008.

[249] Hannah Clevenson, Matthew E Trusheim, Carson Teale, Tim Schröder, Danielle Braje, and Dirk Englund. Broadband magnetometry and temperature sensing with a light-trapping diamond waveguide. *Nature Physics*, 11(5):393–397, 2015.

[250] Zongmin Ma, Shaowen Zhang, Yueping Fu, Hua Yuan, Yunbo Shi, Jian Gao, Li Qin, Jun Tang, Jun Liu, and Yanjun Li. Magnetometry for precision measurement using frequency-modulation microwave combined efficient photon-collection technique on an ensemble of nitrogen-vacancy centers in diamond. *Optics Express*, 26(1):382–390, 2018.

[251] Keigo Arai, Chinmay Belthangady, Huiliang Zhang, N Bar-Gill, SJ DeVience, Paola Cappellaro, Amir Yacoby, and Ronald Lee Walsworth. Fourier magnetic imaging with nanoscale resolution and compressed sensing speed-up using electronic spins in diamond. *Nature nanotechnology*, 10(10):859–864, 2015.

[252] Gerald Waldherr, Johannes Beck, Philipp Neumann, RS Said, M Nitsche, ML Markham, DJ Twitchen, J Twamley, Fedor Jelezko, and J Wrachtrup. High-dynamic-range magnetometry with a single nuclear spin in diamond. *Nature nanotechnology*, 7(2):105–108, 2012.

[253] Graciana Puentes, Gerald Waldherr, Philipp Neumann, Gopalakrishnan Balasubramanian, and Jörg Wrachtrup. Efficient route to high-bandwidth nanoscale magnetometry using single spins in diamond. *Scientific reports*, 4(1):1–6, 2014.

Appendix A

SPRINGER NATURE LICENSE
TERMS AND CONDITIONS

Aug 05, 2021

This Agreement between University of Saskatchewan -- Hammed Ejalonibu ("You") and Springer Nature ("Springer Nature") consists of your license details and the terms and conditions provided by Springer Nature and Copyright Clearance Center.

License Number	5122590488349
License date	Aug 05, 2021
Licensed Content Publisher	Springer Nature
Licensed Content Publication	Journal of Materials Science: Materials in Electronics
Licensed Content Title	Optimal parameter(s) for the synthesis of nitrogen-vacancy (NV) centres in polycrystalline diamonds at low pressure
Licensed Content Author	Hammed A. Ejalonibu et al
Licensed Content Date	Apr 25, 2019
Type of Use	Thesis/Dissertation
Requestor type	academic/university or research institute
Format	electronic
Portion	full article/chapter
Will you be	no

Appendix B

The effect of step-wise surface nitrogen doping in MPECVD grown polycrystalline diamonds

Author: Hammed Ejalonibu,Gordon Sarty,Michael Bradley

Publication: Materials Science and Engineering: B

Publisher: Elsevier

Date: August 2020